MAX-PLANCK-INSTITUT
FÜR METEOROLOGIE

Factors influencing subtropical stratocumulus: from a large-scale thermodynamic to a dynamical perspective

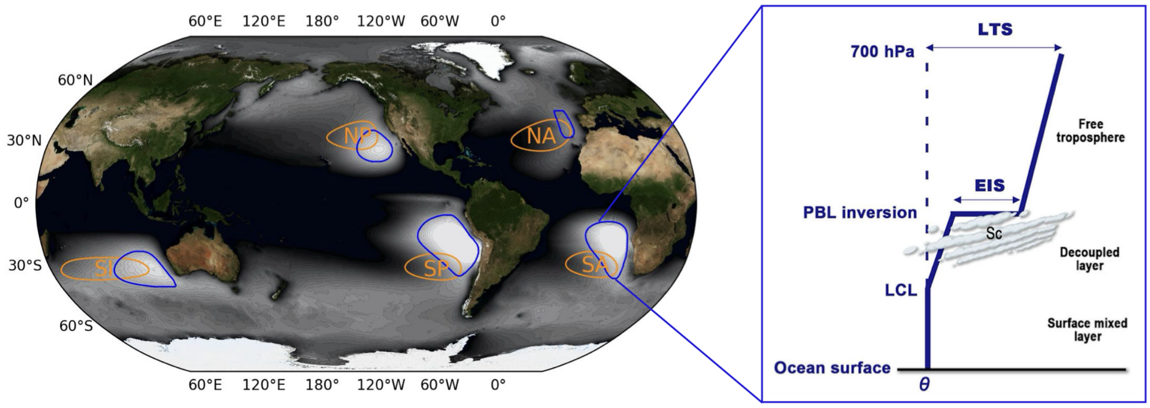

Hairu Ding

Hamburg 2026

Berichte zur Erdsystemforschung
Reports on Earth System Science

303
2026

Hinweis

Notice

Anschrift / Address

Max-Planck-Institut für Meteorologie
Bundesstrasse 53
20146 Hamburg
Deutschland

Tel./Phone: +49 (0)40 4 11 73 - 0
Fax: +49 (0)40 4 11 73 - 298

name.surname@mpimet.mpg.de
www.mpimet.mpg.de

Layout

Bettina Diallo and Norbert P. Noreiks
Communication

Copyright

Photos below: ©MPI-M
Photos on the back from left to right:
Christian Klepp, Jochem Marotzke,
Christian Klepp, Clotilde Dubois,
Christian Klepp, Katsumasa Tanaka

Factors influencing subtropical stratocumulus: from a large-scale thermodynamic to a dynamical perspective

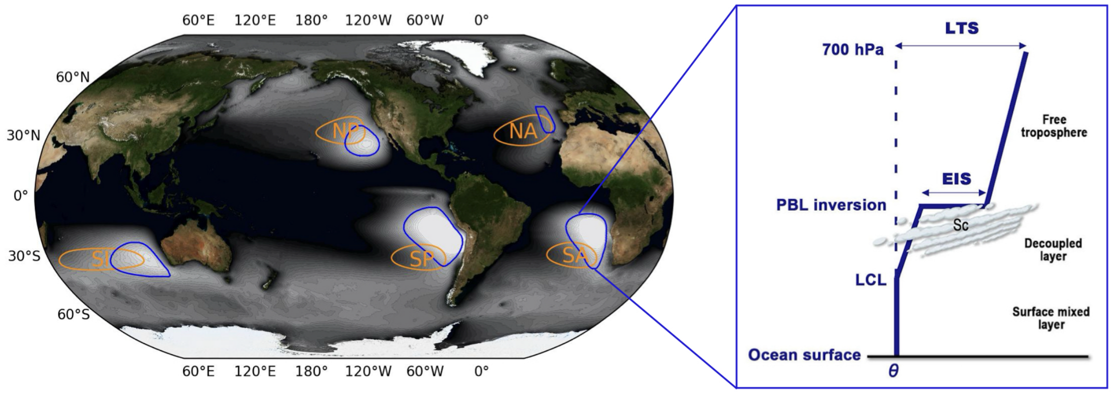

Hairu Ding

Hamburg 2026

Hairu Ding
aus Shandong, China

Max-Planck-Institut für Meteorologie
The International Max Planck Research School on Earth System Modelling
(IMPRS-ESM)
Bundesstrasse 53
20146 Hamburg

Tag der Disputation: 27. Mai 2026

Folgende Gutachter empfehlen die Annahme der Dissertation:
Prof. Dr. Bjorn Stevens
Prof. Dr. Nedjeljka Žagar

Vorsitzender des Promotionsausschusses:
Prof. Dr. Hermann Held

Dekan der MIN-Fakultät:
Prof. Dr.-Ing. Norbert Ritter

Berichte zur Erdsystemforschung / Max-Planck-Institut für Meteorologie 303
Reports on Earth System Science / Max Planck Institute for Meteorology 2026

ISSN 1614-1199 - doi: 10.17617/2.3713152

PREFACE

We live in a world full of beautiful coincidences, which makes it fun to just enjoy the magic (e.g., Fig. 1). Meanwhile, coincidences sometimes hamper people's understanding of the world.

This work starts with some facts: stratocumulus are located on the eastern edge of subtropical highs, where the lower-tropospheric stability happens to be large. These facts guide people's hypotheses on stratocumulus variability to a direct influence of local thermodynamics from the Hadley/Walker-like circulation. To date, contradictions within this framework have been increasingly realized. As there are few alternatives, this framework continues to be used with more additions and conditions. This study finds that the co-location of subtropical highs, lower-tropospheric stability, and stratocumulus comes from complex reasons, which cause them to maximize in adjacent areas and to show larger co-variability than their direct relationships. An extratropical dynamical framework is suggested to replace the local thermodynamics as the main large-scale mechanisms for stratocumulus variability.

In addition to the framework change, this work also examines the role of lower-tropospheric stability. Stability, viewed from the perspective of maintenance (or entrainment restriction), is insufficient to explain the full variability in stratocumulus. This work highlights the direct response of stratocumulus to circulation through stronger winds, which is pronounced across timescales. Stratocumulus variability shows a larger dependence on upstream conditions than on local ones. Using upstream conditions and local stability explains about half of the stratocumulus variability in the daily series. On the track of what processes control the other half, further work is still required.

Questioning the direct influence of lower-tropospheric stability, which used to be regarded as a "good proxy" for stratocumulus, seems discouraging. However, understanding its limitations is one way to proceed. I regard the process of revisiting previous approaches and reorganizing views as a spiral progression in a musical canon. With this overview, I hope you enjoy the reading.

(a) Taken in Budapest, 2023. (b) Taken in Hamburg, 2025.

Figure 1: Examples of the beauty in coincidence.

ABSTRACT

Semi-persistent subtropical stratocumulus cover approximately one-fifth of the low-latitude oceans. Their large coverage and semi-persistence contribute significantly to the Earth's energy budget by reflecting solar radiation. Because of this role, their variability raises interest in many studies. However, the large-scale mechanisms controlling their variability are still not well understood, causing uncertainties regarding future change. This study aims to understand the large-scale mechanisms for stratocumulus variability.

I examine two local thermodynamic effects of subtropical highs using reanalyses. One effect is adiabatic warming by atmospheric subsidence, and the other is cooling by ocean Ekman pumping. Both effects are hypothesized to increase lower-tropospheric stability and therefore inhibit entrainment drying at the cloud top, favoring more stratocumulus. The results show that local thermodynamics have little influence on variability in lower-tropospheric stability.

I then investigate the non-local effects by identifying large-scale circulation that covaries with stratocumulus. Two indices within stratocumulus areas are selected: estimated inversion strength (EIS, representing lower-tropospheric stability) and low-cloud cover (LCC). The results show that most of the EIS variability is controlled by extratropical eddies (represented by synoptic-scale Rossby ridges), while on long timescales (interseasonal and interannual), local sea surface cooling becomes more important. The role of remote monsoons is not observed for stratocumulus variability. Therefore, the large-scale mechanisms for stratocumulus variability are revised from the local thermodynamic view to the extratropical wave dynamical view.

Based on the view change, the importance of near-field orography is discussed, particularly in the phase-locked amplification effect on synoptic-scale Rossby ridges. These amplification effects create a zonally asymmetric distribution of EIS in the subtropics, which is one of the key reasons for the stratocumulus habitats.

Compared to EIS, which is controlled by local high and local sea surface cooling, LCC covaries with upstream high and upstream warming, which provide stronger winds in the stratocumulus area. These stronger winds influence LCC by enhancing boundary-layer mixing and offsetting the drying effects of Rossby ridges, without being mediated by EIS. The strong correlation between EIS and LCC on long timescales is confounded by the negative phase of a PDO-like (Pacific Decadal Oscillation) circulation pattern. These findings suggest that the correlation between EIS and LCC is larger than their direct causal relationships.

Overall, this study provides an explicit view of the relationships between large-scale circulation, lower-tropospheric stability, and stratocumulus, and it explains the physical processes behind these relationships.

ZUSAMMENFASSUNG (ÜBERSETZT MIT DEEPL.COM)

Halbpermanente subtropische Stratocumulus-Wolken bedecken etwa ein Fünftel der Ozeane in den niedrigen Breitengraden. Durch ihre große Ausdehnung und Halbpermanenz tragen sie durch die Reflexion der Sonnenstrahlung erheblich zum Energiebilanz der Erde bei. Aufgrund dieser Rolle ist ihre Variabilität Gegenstand zahlreicher Studien. Die großräumigen Mechanismen, die ihre Variabilität steuern, sind jedoch noch nicht gut verstanden, was zu Unsicherheiten hinsichtlich künftiger Veränderungen führt. Ziel dieser Studie ist es, die großräumigen Mechanismen der Stratocumulus-Variabilität zu verstehen.

Ich untersuche zwei lokale thermodynamische Effekte subtropischer Hochdruckgebiete anhand von Reanalysen. Der eine Effekt ist die adiabatische Erwärmung durch atmosphärische Absinkung, der andere die Abkühlung durch das Ekman-Pumpen des Ozeans. Für beide Effekte wird angenommen, dass sie die Stabilität der unteren Troposphäre erhöhen und somit die Entmischungstrocknung an der Wolkenobergrenze hemmen, was eine stärkere Stratocumulusbildung begünstigt. Die Ergebnisse zeigen, dass lokale thermodynamische Effekte nur einen geringen Einfluss auf die Variabilität der Stabilität in der unteren Troposphäre haben.

Anschließend untersuche ich die nichtlokalen Effekte, indem ich großräumige Zirkulationen identifiziere, die mit Stratocumulus-Wolken korrelieren. Es werden zwei Indizes innerhalb von Stratocumulus-Gebieten ausgewählt: die geschätzte Inversionsstärke (EIS, die die Stabilität in der unteren Troposphäre repräsentiert) und die niedrige Wolkendecke (LCC). Die Ergebnisse zeigen, dass der Großteil der EIS-Variabilität durch extratropische Wirbel (repräsentiert durch Rossby-Rücken im synoptischen Maßstab) gesteuert wird, während auf langen Zeitskalen (zwischen den Jahreszeiten und zwischen den Jahren) die lokale Abkühlung der Meeresoberfläche an Bedeutung gewinnt. Eine Rolle entfernter Monsune für die Stratocumulus-Variabilität wird nicht beobachtet. Daher werden die großräumigen Mechanismen für die Stratocumulus-Variabilität von einer lokalen thermodynamischen Sichtweise auf eine Sichtweise der extratropischen Wellendynamik umgestellt.

Auf der Grundlage dieser Sichtweise wird die Bedeutung der Nahfeld-Orografie diskutiert, insbesondere im Hinblick auf den phasenverriegelten Verstärkungseffekt auf Rossby-Rücken synoptischer Skala. Diese Verstärkungseffekte erzeugen eine zonal asymmetrische Verteilung des EIS in den Subtropen, was einer der Hauptgründe für die Stratocumulus-Habitate ist.

Im Vergleich zum EIS, das durch lokale Hochdruckgebiete und die lokale Abkühlung der Meeresoberfläche gesteuert wird, korreliert die LCC mit stromaufwärts gelegenen Hochdruckgebieten und der dortigen Erwärmung, die im Stratocumulus-Gebiet stärkere Winde verursachen. Diese stärkeren Winde beeinflussen die LCC, indem sie die Vermischung in der Grenzschicht verstärken und die austrocknenden Effekte von Rossby-Rücken ausgleichen, ohne dass dies durch das EIS vermittelt wird. Die starke Korrelation zwischen EIS und LCC auf langen Zeitskalen wird durch die negative Phase eines PDO-ähnlichen (Pacific Decadal Oscillation) Zirkulationsmusters verfälscht. Diese Ergebnisse deuten darauf hin, dass die Korrelation zwischen EIS und LCC größer ist als ihre direkten kausalen Zusammenhänge.

Insgesamt liefert diese Studie einen klaren Überblick über die Zusammenhänge zwischen großräumiger Zirkulation, Stabilität in der unteren Troposphäre und Stratocumulus und erklärt die physikalischen Prozesse, die diesen Zusammenhängen zugrunde liegen.

PUBLICATIONS

The following two publications are part of this dissertation and are included in the appendix:

Appendix A

Ding, H., Stevens, B., and Schmidt, H. (2025). Factors causing stratocumulus to deviate from subtropical high variability on seasonal to interannual timescales. Atmospheric Chemistry and Physics, 25(18), 10511-10521. `https://doi.org/10.5194/acp-25-10511-2025`

Appendix B

Ding, H., Stevens, B., Lunkeit, F., Žagar, N. (2026). Large-scale circulation and stratocumulus variability. *Submitted to Weather and Climate Dynamics*

ACKNOWLEDGMENTS

I appreciate this precious journey, during which I was able to focus on exploring questions and keep some distance from utilitarian criteria. I can imagine how unique it is, both compared with the past and the future. A lot of people to acknowledge during this journey.

I appreciate Bjorn Stevens. Thank him for bringing me to the subtropics. I appreciate his openness to getting results that go against hypotheses. I have learned many great things from him, from details to principles. One crucial principle is like Occam's razor: keep it simple. He always suggests adding evidence/hypotheses only when necessary, which makes me reflect a lot. I was encouraged to think about theories critically. I've learned from him that a valuable contribution is to help people understand more (or recognize what they understand less), no matter how simple it is. Therefore, they can answer the "why" and "how" questions themselves.

I appreciate Nedjeljka Žagar, who has helped a lot with research methods, my understanding, and presentation. I appreciate the thoughts and experiences shared by her. Her understanding of atmospheric dynamics and waves aids a lot in this study. I appreciate her carefulness in analyzing and phrasing. I also thank her for her detailed suggestions, which contribute significantly to the conclusion. I appreciate that she always encourages juniors throughout different phases of research.

I appreciate Hauke Schmidt, who has provided many precise suggestions, from detailed wording to the broader picture of results. Thank him for his help with rehearsals, drafting, testing ideas, addressing technical questions, and more. I cannot imagine how I would have attended my first conference, given my first talk, submitted my first paper, ect, without his support.

I appreciate people like Frank Lunkeit, Katharina Holube, Sergiy Vasylkevych, Marius Schulz, Moritz Günther, Peishan Chen, Clemens Schannwell, Sebastian Rast, Raphael Pistor, Jakub Nowak, Noel Gutierrez-Brizuela, Franziska Glassmeier, Lukas Kluft, Hideaki Kawai, Tiffany Shaw, Jiawei Bao, George Datseris, Hans Segura, Marco Giorgetta, Maeve Mayer, Volkmar Wirth, Mark Webb, Juntian Chen, who have ever brought inputs/help to this study. I appreciate Brian Mapes, who introduced the correlation networks and the logic of causality that inspired my later thinking.

I appreciate the questions from all of the above; the study develops in a way that I want to answer their questions.

I deeply appreciate Angela Gruber, whom I had to disturb many times. I am grateful for her help on countless occasions in negotiating and arranging appointments. I also appreciate Cornelia Kampmann, Antje Weitz, Michaela Born, Chen Wang, Florian Mundt, Hernan Campos, Chao Li, Hongdou Fan, Florian Ziemen, who have provided help beyond the research. I thank Sergiy again, who kindly asked whether I needed a mattress during the thesis-writing period. I give my special appreciation to Li Dong and Ross Bannister, who have shared a lot of experience in doing research, which helped me find my key interests before this journey.

Last but not least, I appreciate my friends and family. They are always there, being a solid anchor in my fluid life.

ACRONYMS

Sc	stratocumulus
LCC	low-cloud cover
NP	North Pacific
NA	North Atlantic
SI	South Indian Ocean
SP	South Pacific
SA	South Atlantic
LHF	surface latent heat flux
SLP	mean sea level pressure
SST	sea surface temperature
EIS	estimated inversion strength
LTS	lower-tropospheric stability
IG	inertia-gravity
NVA	negative vorticity advection
PDO	Pacific decadal oscillation

The difference between LTS and EIS is not emphasized. Both are employed to represent lower-tropospheric stability. LTS is used mainly for physical interpretation, and EIS for statistical analysis.

CONTENTS

Part I

Unifying Essay

1

INTRODUCTION

This chapter introduces the importance of stratocumulus (Section 1.1), the previously hypothesized large-scale mechanisms (Section 1.2), the contradictions and questions that remain in these hypotheses (Section 1.3), and the structure of the research and the thesis (Section 1.4).

1.1 Semi-persistent subtropical stratocumulus

A satellite view of low-cloud cover (LCC) in climatology is shown in Figure 1.1. Blue contours identify regions of semi-persistent low clouds, characterizing the typical habitats of stratocumulus (Sc). Sc are boundary-layer clouds with thin and layered structure (Wood, 2012). They are adjacent to the mass center of subtropical highs (orange contours). Vertically, Sc lay at the top of the well-mixed boundary-layer and capped by a stable free troposphere[1] (Lilly, 1968). The stable free troposphere can inhibit the cloud-top entrainment drying and benefit the maintenance of Sc (Stevens et al., 2001; Wood and Bretherton, 2004). Hence, Sc persist longer than other low clouds.

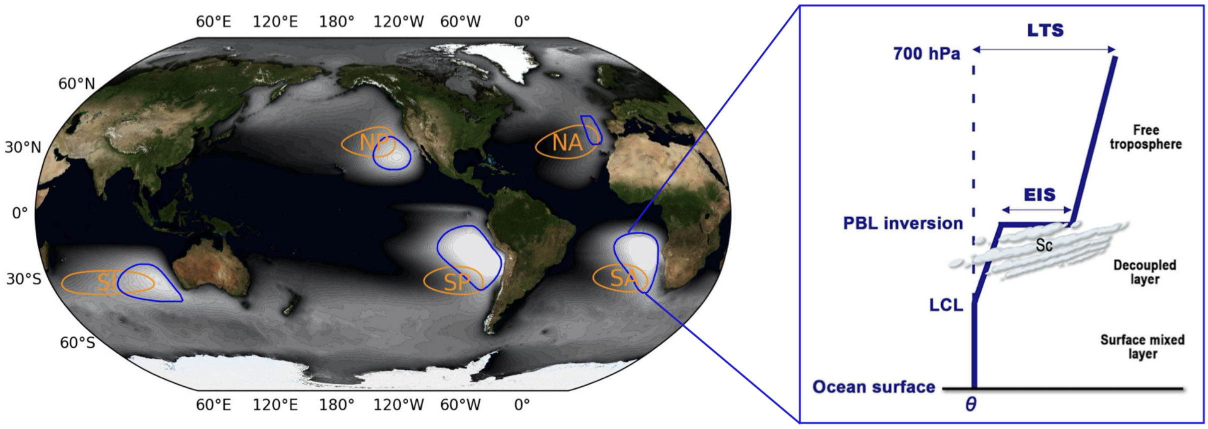

Figure 1.1: Map of 1987–2019 mean LCC and schematic potential temperature (θ) profile showing the vertical location of stratocumulus. Orange contours mark subtropical highs where mean sea level pressure (SLP) exceeds 1020 hPa. Abbreviation of regions: North Atlantic (NA), North Pacific (NP), South Indian Ocean (SI), South Pacific (SP), South Atlantic (SA). Blue contours mark areas where LCC exceeds 40% in NA and 50% in other regions. Abbreviation in the vertical profile: lower-tropospheric stability (LTS), estimated inversion strength (EIS), planetary boundary-layer (PBL), lifting condensation level (LCL). Topography and snow cover use the NASA Blue Marble base map for July.

---

[1] Also called the inversion layer in many studies, although it does not need to meet the inversion criteria.

Apart from the persistence, Sc are also recognized by their large coverage and high albedo. Subtropical Sc cover approximately one-fifth of the low-latitude oceans. Chen, Rossow, and Zhang (2000) compared the radiation effects of different clouds and found that Sc contribute the most in reflecting the solar radiation. Before these quantitative comparisons became available, the radiative effects of Sc had already been discussed since the last century. Studies investigated how a small to modest fraction change in Sc can be comparable with the doubling of CO_2 (Hartmann and Short, 1980; Randall et al., 1984; Randall and Suarez, 1984; Slingo, 1990). Owing to these studies, Sc are regarded as the Earth's refrigerators.

Regarding their influence on Earth's radiation budget, one may focus on the "persistent" feature of Sc and ignore the "semi." Many studies aim to determine the future trend of Sc, even though the mechanisms underlying their current variability are not well understood. However, this advanced goal is hampered by uncertainties in the representation of clouds in Earth system models, with Sc contributing the largest part of these uncertainties (Bony and Dufresne, 2005; Soden and Vecchi, 2011). It is worth noting that Sc exhibit a broad spectrum of variability, spanning from diurnal cycles to interannual timescales. That is why "semi" is used to describe the persistence that appears as a statistical result in climatology.

In this study, I try to understand the Sc variability that does not cancel out over periodic cycles (i.e., diurnal and annual cycles) across all timescales. This focus helps avoid confounding effects, such as those arising from solar isolation. Table 1.1 shows the variance of stratocumulus (represented by LCC) on different timescales, based on deseasonalized daily satellite observations. We see that Sc are not "inactive clouds", as often perceived. Instead, high-frequency variability contributes most of the variance beyond the diurnal and annual cycles.

Table 1.1: Variance of daily LCC / % series after deseasonalization (σ^2_{des}). Overline denotes the 33-year (1987–2019) mean of the original daily series. The four rightmost columns show the variance on each timescale derived from the fast Fourier transform: synoptic ($\leq$ 15 days), subseasonal (15–90 days), interseasonal (90–365 days), and interannual (> 365 days).

	σ^2_{des}	$\overline{\mathrm{LCC}}$	$\sigma^2_{\mathrm{synoptic}}$	$\sigma^2_{\mathrm{subseasonal}}$	$\sigma^2_{\mathrm{interseasonal}}$	$\sigma^2_{\mathrm{interannual}}$
North Pacific (NP)	331	57	136	137	34	24
North Atlantic (NA)	461	43	204	187	51	19
South Indian Ocean (SI)	252	56	130	86	21	16
South Pacific (SP)	120	63	46	48	14	12
South Atlantic (SA)	150	61	65	60	13	13

1.2 Large-scale mechanisms proposed in previous studies

The connection between large-scale circulation and Sc originates from questions about their preferred habitats. As Sc prefer the eastern edge of subtropical highs, they are hypothesized to be controlled by the large stability there.

In the classical view, the large stability in Sc areas is attributed to local thermodynamics, as the descending branch of the Hadley cell adiabatically warms the subtropical free troposphere (Hadley, 1735; Held and Hou, 1980; Lindzen and Hou, 1988). To explain the zonal asymmetry in Sc distribution, the subsidence associated with the Walker cell and land–sea circulation is invoked, along with the cooler surface resulting from ocean upwelling (Figure 1.2). To further explain the summer peak of Sc, the Rossby wave train induced by off-equatorial heating, such as monsoons, is also considered an additional source of subsidence (Rodwell and Hoskins, 1996; Rodwell and Hoskins, 2001). This local thermodynamic view is commonly believed for decades (e.g., Bretherton and Hartmann, 2009; Dussen, Roode, and Siebesma, 2016; Klein and Hartmann, 1993; Randall, 1980; Schubert, 1976).

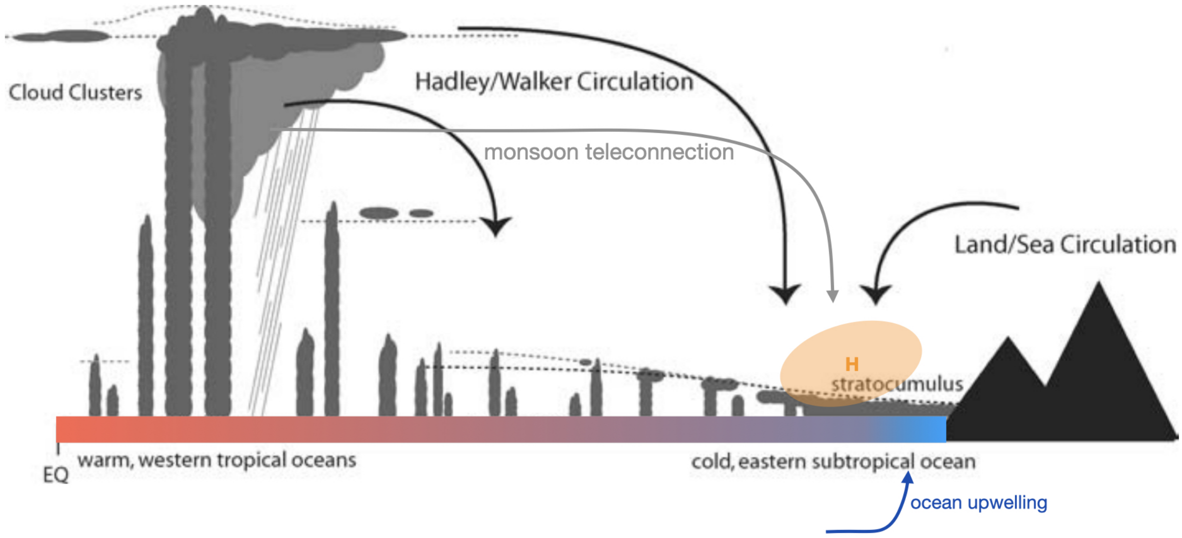

Figure 1.2: Schematic plot borrowed from Stevens (2005), with additions including monsoon teleconnection, the subtropical high, and ocean upwelling. The meridional and zonal dimensions are collapsed into a single dimension for simplicity.

Studies have been investigating the relationship between variations in stability and Sc. Klein and Hartmann (1993) proposed the concept of lower-tropospheric stability (LTS), defined as the potential temperature difference between 700 and 1000 hPa. They show that LTS and LCC in Sc areas are strongly correlated on the annual cycle and interannual timescales. Later in Wood and Bretherton (2006), the measurement of lower-tropospheric stability is improved by a factor called estimated inversion strength (EIS), which removes the temperature-dependent moist adiabatic lapse rate (see Figure 1.1). By this correction, EIS shows less regime dependence to represent LCC.

Studies also explored how to improve EIS by taking into account the specific humidity difference between 700 and 1000 hPa (Kawai, Koshiro, and Webb, 2017) and the boundary-layer height (Wang et al., 2023). The former one targets the trend of Sc in a changing climate, while the latter targets better representing the day-by-day variability of Sc. Both slightly increase the correlation between the modified indices and Sc compared with EIS for their respective targets, but not across all timescales. My study provides a physical explanation for why these factors show timescale-dependent improvements: the former happen to involve the different responses of LCC and EIS to large-scale circulation, while the latter reflects boundary-layer suppression by an upstream Rossby ridge.

Unlike the strong correlation with EIS on long timescales, Sc variability shows complexity on shorter timescales (i.e., synoptic and subseasonal). On short timescales, the strength and location of subtropical highs (Garreaud et al., 2001; George and Wood, 2010; Klein, Hartmann, and Norris, 1995; Toniazzo et al., 2011), subsidence (Blossey et al., 2013; Bretherton, Blossey, and Jones, 2013; Norris and Klein, 2000; Randall and Suarez, 1984), relative humidity, and boundary-layer cold advection (Klein, 1997) are often taken into account. Klein (1997) found that no single factor can fully represent the short-term variability of Sc. This already indicates some limitations of the local thermodynamic view, drawing attention to atmospheric motion. Nevertheless, studies tend to consider atmospheric motion on short timescales while still interpreting changes in the background flow from the local thermodynamic view.

Klein, Hartmann, and Norris (1995) first emphasized the importance of atmospheric motion on short timescales, although their hypothesis was limited to short Lagrangian trajectories (about one day). Since then, the mechanism on short timescales has been framed as follows: Sc require about one day to adjust their mass, and enhanced cloud mass one day earlier is still attributed to higher EIS, represented by stronger subtropical highs (e.g., Lewis and Bellon, 2025; Lewis, Bellon, and Dinh, 2023). However, this interpretation is not clearly supported by observations. Furthermore, as air mass adjustment typically takes days to weeks (Dong, Gregory, and Sutton, 2001), it is unclear why Sc preferentially covary with conditions one day earlier rather than with conditions further back in time. Thus, while including atmospheric motion represents an important step forward, combining local thermodynamics with regional Lagrangian trajectories is insufficient to explain the observed phenomena.

1.3 Puzzles

The above introduction already highlights some aspects that need to be explained, and there are more contradictions and questions within the previous large-scale framework.

The local thermodynamic view hypothesizes that EIS is controlled by subsidence and serves as a mediator through which large-scale circulation influences Sc. However, studies show that subsidence has opposite effects on Sc on short timescales. Clemesha et al. (2017) show that although subsidence can increase EIS, too much subsidence limits cloudiness. Myers and Norris (2013) further support that, at constant EIS, stronger subsidence reduces Sc. For Sc, subsidence and EIS have some independent effects (although they also interact): subsidence lowers the boundary-layer height and restricts cloud depth (Bretherton, Blossey, and Jones, 2013; Randall and Suarez, 1984), whereas EIS suppresses cloud-top entrainment through larger restoring buoyancy[2]. The observed contradictions indicate that subsidence and EIS can be decoupled on short timescales. This raises the question of what controls EIS variability on those timescales.

Once the opposite effects of subsidence and EIS are uncovered, the relationship between Sc and subtropical highs becomes uncertain, as a stronger subtropical high may represent stronger subsidence and higher EIS simultaneously. In addition, it is unclear why the co-variability between Sc and subtropical highs is emphasized only on short timescales, but not on longer timescales, which are supposed to better reflect the local thermodynamic view.

Not only for short timescales, the dominant role of EIS is also being questioned for longer timescales. Koshiro and Shiotani (2014) found that EIS correlates with LCC in the warm sea surface temperature (SST) regime, but not in the cold SST regime. The large-eddy simulations of Bretherton and Blossey (2014) show that changes in EIS are less important for Sc in response to a warmer climate. CMIP (Coupled Model Intercomparison Project) models also show that Sc can decrease even as EIS increases in warming experiments (Qu et al., 2014; Webb and Lock, 2013). Therefore, people lose the clue to future Sc changes along with the uncertainties in cloud simulations.

---

[2] EIS $\sim \Delta\theta_{700} - \theta_{1000}$; the squared buoyancy frequency for dry air $N^2 \equiv \frac{g}{\theta}\frac{d\theta}{dz}$

1.4 Research design

The first project is designed to examine the local thermodynamic view. Given that subsidence can be decoupled from EIS on short timescales, this project tests whether EIS is indeed controlled by local thermodynamics on long timescales. In this project, I use EIS as a proxy for Sc, following previous assumptions. The complexity on short timescales is not addressed in this project. Results explicitly show the limitation of the local thermodynamics (Appendix A, Chapter 3).

Motivated by the limitation of the local thermodynamics, the second project investigates the mechanisms that really drive EIS. It considers processes from synoptic to interannual timescales to identify robust relationships. Results show that extratropical Rossby waves dominate EIS variability (Appendix B, Chapter 3). In addition, this project explains the puzzles introduced above, and provides a new perspective on the relationship between EIS and Sc (Appendix B, Chapter 5).

Based on the findings of the second project, I developed a hypothesis about the near-field orographical effects on Sc. This hypothesis provides an additional explanation for why Sc favors the east coasts of subtropical oceans. It is further supported by simulation experiments (Chapter 4).

2

DATA AND APPROACH

2.1 Data

This study uses satellite observations for LCC and ERA5[1] (Hersbach et al., 2017b) reanalyses for the large-scale conditions.

Two satellite products are used due to some historical reasons: a. the second version of the ATSR-AATSR[2] (Poulsen et al., 2017) monthly product from January 2003 to December 2011 in the Cloud_cci[3] project; b. CLARA-A3[4] (Karlsson et al., 2022) daily product from January 1987 to December 2019 by EUMETSAT[5] and calculate the monthly mean. The choice of products does not influence our qualified results and conclusions.

The spatial resolution of ATSR-AATSR is $0.5° \times 0.5°$, and of CLARA-A3 is $0.25° \times 0.25°$. ERA5 has a horizontal resolution of $0.225° \times 0.225°$ with 37 vertical pressure levels. The regression analyses apply F128 Gaussian grids (512×256 points along latitude and longitude lines) with 26 vertical pressure levels below 125 hPa.

2.2 Wave-space regression between regional LCC/EIS and global circulation

Applying MODES software (Žagar et al., 2015) to study the coupling between Sc and large-scale circulation.

The MODES performs a multivariate representation of the global circulation in terms of three-dimensional orthogonal vertical and horizontal structure functions — normal modes (i.e., eigensolutions) of the linearized primitive equations. A single mode is defined by three indices: zonal wavenumber k, meridional mode index n, and vertical mode index m. For each n, there are three wave solutions: Rossby–Haurwitz wave (geostrophically balanced circulation on the sphere), eastward-propagating inertia–gravity wave (EIG), and westward-propagating inertia–gravity wave (WIG). Two special solutions, equatorially trapped Kelvin and mixed Rossby–gravity (MRG) waves, are included as $n = 0$ EIG and Rossby wave, respectively. The Rossby and MRG waves are collectively referred to as Rossby modes, and WIG and EIG modes, including Kelvin wave, are collectively referred to as IG modes in this study.

---

[1] the fifth generation European Centre for Medium-Range Weather Forecasts atmospheric reanalyses

[2] Along-Track Scanning Radiometer and Advanced Along-Track Scanning Radiometer

[3] European Space Agency Climate Change Initiative

[4] the third edition of the Satellite Application Facility on Climate Monitoring's cloud, albedo, and surface radiation dataset from advanced very-high-resolution radiometer data

[5] European Organisation for the Exploitation of Meteorological Satellites

The configuration applies 200 zonal wavenumber, 19 vertical modes, and 70 meridional modes for each wave type (making a total of 210 meridional modes).

At each time step with data, MODES provides dimensionless expansion coefficients $\chi_n^k(m)$ in each mode, which can represent the full atmospheric circulation collectively. Applied step-by-step to daily/monthly ERA5 data, I obtain the time series of $\chi_n^k(m,t)$. Then the lagged regressions between $\chi_n^k(m,t)$ and EIS/LCC in the Sc area (denoting $\mathcal{I}$ for the index) are computed as:

$$\mathcal{R}_n^k(m,\tau) = \frac{1}{N-1} \frac{\sum_{t=1}^{N} [(\chi_n^k(m,t+\tau) - \overline{\chi_n^k(m)})(\mathcal{I}(t) - \overline{\mathcal{I}})]}{\mathrm{var}(\mathcal{I})}, \tag{2.1}$$

where τ is the lag, N is the length of records, var denotes temporal variance, and the overbar denotes temporal mean. $\mathcal{R}_n^k(m,\tau)$ is computed separately for each Sc area and on each timescale. t and τ are in days for the synoptic, subseasonal, and interseasonal series, and in months for the interannual series. The resulting $\mathcal{R}_n^k(m,\tau)$ (complex variable) is a normalized covariance between circulation and $\mathcal{I}$. It is projected back to the physical space of wind and geopotential height anomalies associated with the variability of $\mathcal{I}$.

The squared amplitude of the regression field, $gD_m|\mathcal{R}_n^k(m,\tau)|^2$, can be integrated along any dimension (k, n, or m) to show the wavenumber distribution of the covariance as a function of the remaining dimensions. For example, $\sum_m \sum_n gD_m|\mathcal{R}_n^k(m,\tau)|^2$ provides the zonal wavenumber distribution of the covariance between the global circulation and $\mathcal{I}$. The multiplication factor gD_m consists of the gravity g and equivalent depth D_m associated with vertical mode m, and it provides variance with the dimension of energy. gD_m can be split into Rossby and IG modes to identify both scales and wave dynamics associated with $\mathcal{I}$.

Note that for each series of $\mathcal{I}$, $\mathcal{R}_n^k(m,\tau)$ is normalized by a different variance (var($\mathcal{I}$)). Therefore, amplitudes across areas, timescales, or indices are incomparable. Thus, I mainly use this regression method to analyze the wave pattern and combine it with the composite analysis of original ERA5 data to interpret the processes in terms of amplitudes.

2.3 Simulation experiments

Applying ICON[6] (Hohenegger et al., 2023) for atmospheric simulations. I use the same model version as the Cycle 5 in the nextGEMS[7] project (Segura et al., 2025). This model produces a realistic representation of LCC in Sc areas compared with satellite observations and reanalysis data (Fons et al., 2024).

The Control simulation is conducted following the AMIP[8] specifications (Gates, 1992; Gates et al., 1999). It uses the atmospheric model forced by monthly historical SST and sea ice conditions, together with annually historical greenhouse gas concentrations since 1979. Aerosol concentrations are fixed at their 1979 values. The simulation covers three years (1979-01-01 to 1981-12-31) with a 60 s time step and R2B8 resolution (about 10 km). Model outputs are saved as daily means on the model grid below 20 km altitude and are interpolated to regular grids (0.225° × 0.225°) and pressure levels (22 levels below 125 hPa) for analysis. The first month of outputs is discarded for model spin-up.

---

[6] the ICOsahedral Non-hydrostatic global storm-resolving model

[7] Next Generation of Earth Modeling Systems

[8] Atmospheric Model Intercomparison Project

The "noTopo" experiment adopts the same configuration as the Control simulation, except that the land elevation, the elevation-caused roughness length, and the subgrid topography are removed. Surface depressions are retained as in the control simulation. This experiment aims to study the orographical effects on synoptic timescales.

2.4 Timescale decomposition

For ERA5 and CLARA-A3:

Firstly, deseasonalize daily time series from 33 years of data (1987–2019) by subtracting daily climatology. The deseasonalized series are then decomposed into synoptic (< 15 days), subseasonal (15–90 days), and interseasonal (90–365 days) components. The synoptic component is derived by removing a 15-day running mean. The subseasonal component is obtained using a band-pass filter defined as the difference between 90-day and 15-day running means. The interseasonal component is similarly obtained as the difference between 365-day and 90-day running means. The interannual (> 1 year) component is obtained by a 12-month running mean of the monthly time series. Deseasonalization is not applied on the interannual timescales, as the 12-month running mean effectively removes the annual cycle.

For ICON:

With the three-year simulation, the annual cycle can be efficiently removed by subtracting a 15-day running mean. No additional deseasonalization is needed.

3

LARGE-SCALE MECHANISMS FOR LOWER-TROPOSPHERIC STABILITY

This study use EIS as a quantitative measure of lower-tropospheric stability:

$$\mathrm{EIS} = \mathrm{LTS} - \Gamma_{\mathrm{m}} \left(Z_{700} - \mathrm{LCL}\right), \tag{3.1}$$

where $\mathrm{LTS} = \theta_{700} - \theta_{1000}$, Γ_{m} denotes the moist lapse rate at the average temperature between 700 and 1000 hPa, Z denotes geopotential height, and LCL is the lifting condensation level, which is fixed to be 500 m following the approximations suggested by Lawrence (2005) and Wood and Bretherton (2006).

3.1 Examining the local thermodynamic view

In the classical hypothesis (Figure 1.2), atmospheric subsidence and ocean surface cooling contribute most to lower-tropospheric stability.

Following this hypothesis, a stronger subtropical high, which is generally associated with stronger atmospheric subsidence, would warm θ_{700}. Assuming a steady state ($\frac{\partial \theta}{\partial t} = 0$), the total adiabatic temperature tendency (Q) must be balanced by the diabatic heating (Q_{diab}). In the subtropical region, the transient eddy terms were assumed to be negligible in this thermodynamic balance according to Rodwell and Hoskins (2001). Therefore, the adiabatic term can be computed from the monthly data as:

$$Q = -Q_{\mathrm{diab}} = -\boldsymbol{v} \cdot \nabla \theta - \omega \frac{\partial \theta}{\partial p}, \tag{3.2}$$

where $\boldsymbol{v} \cdot \nabla \theta$ denotes horizontal advection, with $\boldsymbol{v}$, the winds; $\omega \frac{\partial \theta}{\partial p}$ describes vertical advection, with ω representing vertical (pressure) velocity, and p denoting the pressure.

However, results show that although subsidence warming dominates the total adiabatic temperature tendency, this tendency is insufficient to explain the temperature change in the free troposphere (panels a and b in Figure 3.1). In addition, subsidence rates in the Sc area (ω_{700c}) do not follow the strength of the subtropical high ($\mathrm{SLP_H}$; see panel d). Panel c further supports that variations in subsidence are inhomogeneous from the high-pressure system to the Sc area.

Figure 3.1 presents these findings on interannual timescales, in line with my focus on non-periodic variability (introduced in Section 1.1). The relationship was also examined on the annual cycle, and the conclusions were found to be consistent (see details in Appendix A).

Given that subsidence does not control free-tropospheric temperature, the question becomes whether subtropical highs can influence EIS through the surface processes. For this question, hypothesizing that changes in the strength, location, or structure of subtropical highs that steepen the geopotential gradient in the Sc area can play a role. As a larger geopotential

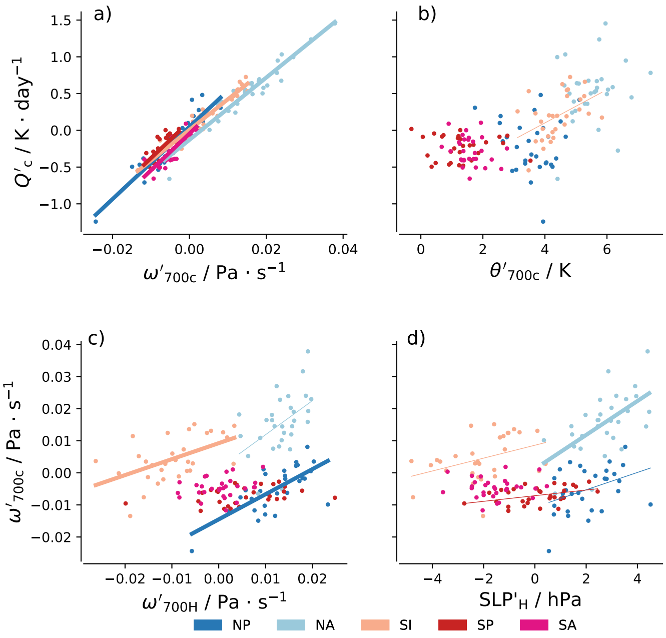

Figure 3.1: Interannual correlation plots between **a)** ω_{700} versus Q, **b)** θ_{700} versus Q, **c)** ω_{700} in the subtropical high area versus that in the Sc area, and **d)** SLP in the subtropical high area versus ω_{700} in the Sc area. Subscripts c and H denote the Sc area and the subtropical high area, respectively. The prime denotes anomaly from the annual mean in the corresponding regions. Each color represents a region. Regression lines are presented for p-values $\leq$ 0.05, and thickened when $r^2 \geq 0.25$. Data: monthly ERA5 from 1985–2014 during summer, July for the Northern Hemisphere and January for the Southern Hemisphere.

gradient can strengthen winds through geostrophic balance, the key is to examine whether these stronger winds influence θ_{1000}. Two pathways are proposed through which stronger winds may influence θ_{1000} via cooling the ocean surface.

The first pathway is through wind-driven Ekman pumping (Anderson and Gill, 1975), which can enhance ocean upwelling. The resulting upwelling velocity is computed as:

$$w_\mathrm{E} = \frac{1}{\rho_0 f} \left(\nabla \times \boldsymbol{\tau} \right) \cdot \boldsymbol{k}, \tag{3.3}$$

where $\rho_0 = 1030\,\mathrm{kg\,m^{-3}}$ is the density of ocean water, f is the Coriolis parameter, and

$$\boldsymbol{\tau} = \boldsymbol{v_{10}} \cdot \rho_\mathrm{a} C_\mathrm{D} \|V\| \tag{3.4}$$

is the wind-stress, with $\rho_\mathrm{a} = 1.225\,\mathrm{kg\,m^{-3}}$ the density of near-surface air, C_D the drag coefficient, $\boldsymbol{v_{10}}$ the 10 m wind vector, and $\|V\|$ the wind speed. [1]

The second pathway is that stronger winds can increase evaporation and enhance surface latent heat flux (LHF). To test the influence on EIS, only the temperature effect is considered in this pathway.

Results show that both Ekman pumping and LHF play a limited role in modulating θ_{1000}, as neither shows a significant correlation (Figure 3.2). These results indicate that EIS is influenced little by stronger winds, which provides the basis for revealing the key distinction between Sc and EIS later in Chapter 5.

---

[1] Since wind speeds are moderate in the subtropics, the drag coefficient C_D is assumed to be constant at 0.0012.

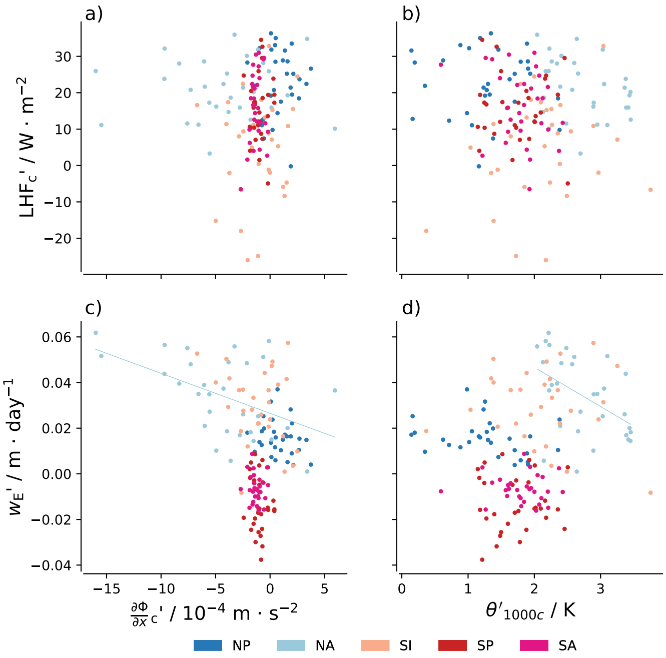

Figure 3.2: Interannual correlation plots between **a)** 700 hPa zonal geopotential gradient ($\frac{\partial\Phi}{\partial x}$) versus surface latent heat flux (LHF), **b)** 1000 hPa potential temperature (θ_{1000}) versus LHF, **c)** $\frac{\partial\Phi}{\partial x}$ versus Ekman pumping velocity in the ocean (w_E; only take the positive value area near the coast), and **d)** θ_{1000} versus w_E. The other settings are similar to Figure 3.1.

Overall, the local thermodynamic view is too rough to explain EIS variability, even on long timescales where quasi-equilibrium assumptions are expected to hold.

3.2 The extratropical dynamical view

To begin investigating the mechanisms that indeed control EIS, Figure 3.3 indicates when the atmosphere or SST plays the dominant role. It shows that EIS is driven by atmospheric processes on synoptic and subseasonal timescales, while the interseasonal one acts as a transition period. On interannual timescales, EIS becomes SST-driven.

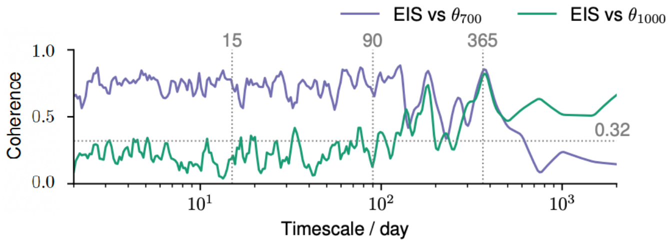

Figure 3.3: Coherence of EIS versus $\theta_{700}/\theta_{1000}$ across timescales. Values exceeding 0.32 are significant at the 90% level. This plot uses the original daily data from 1987–2019 before deseasonalization.

Focusing on the atmosphere-driven timescales first. Figure 3.4 show the perturbation patterns that are associated with EIS variability. Filled contours represent the geopotential height (Z) perturbation in geostrophically balanced Rossby modes, whereas contour lines represent the vertical velocity (ω) in inertia-gravity (IG) modes. In the MODES decomposition (Section B.2.4), IG modes include a mixture of ageostrophic circulation, internal IG and gravity waves, and so on, collectively representing the main part of vertical motions (Žagar et al., 2023).

Therefore, the patterns on synoptic timescales (panels a–b of Figure 3.4; detailed time decomposition method is in Section 2.4) reflect the perturbations of synoptic-scale Rossby waves ($k = 4$–7). The subseasonal and interseasonal timescales also show an important role of synoptic-scale Rossby waves, although at higher latitudes, we see signals of planetary-scale waves (panels c–f). These results indicate that the synoptic-scale Rossby waves, which may interact with the planetary-scale waves, control EIS variability when the atmospheric processes dominate. This deseasonalized conclusion does not differ between winter and summer, although the summertime synoptic-scale Rossby waves are weaker (see the supplementary information in Appendix B).

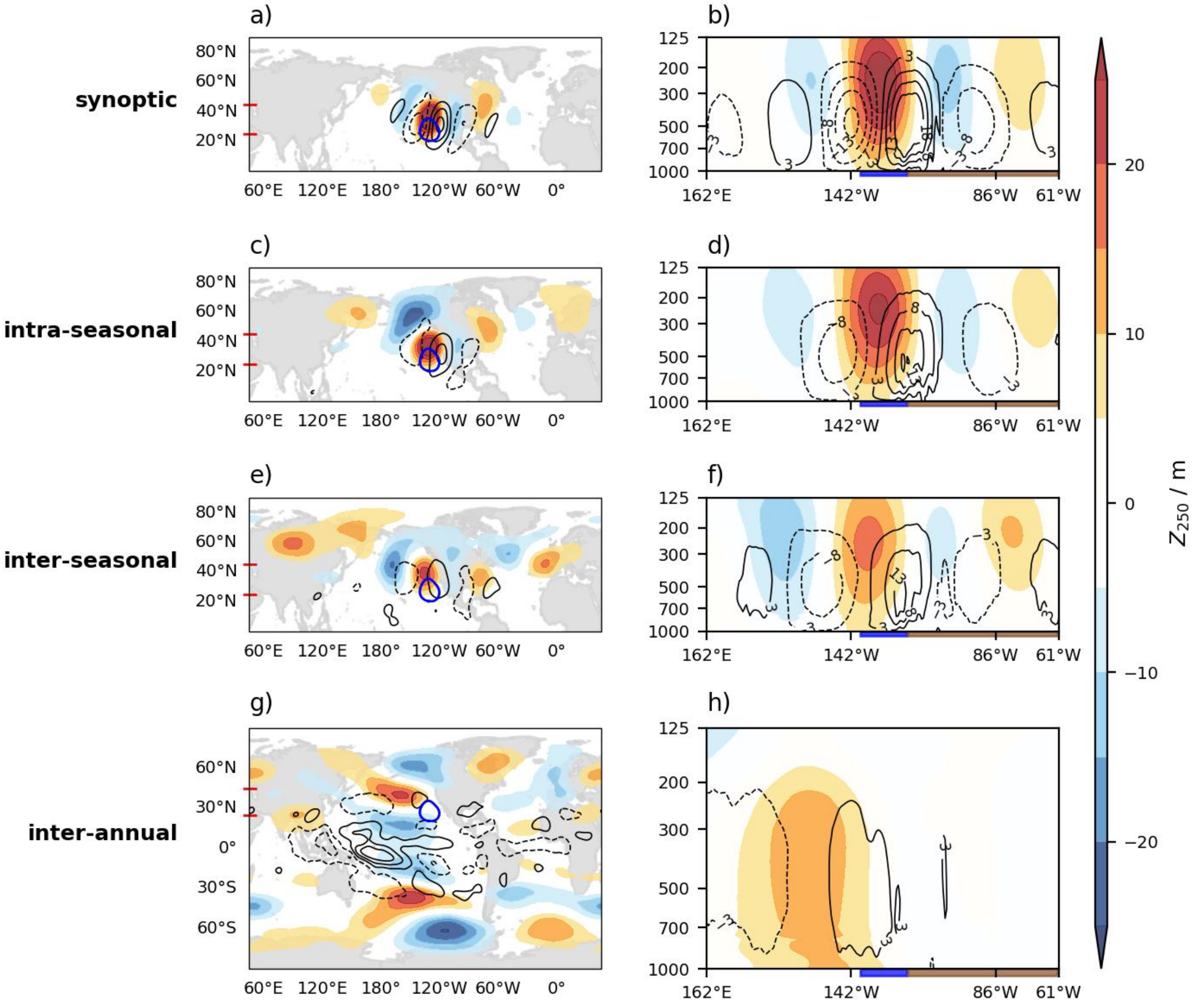

Figure 3.4: Geopotential height (Z) perturbation in Rossby modes (filled contours) and vertical velocity (ω) in IG modes (contour lines) associated with EIS at the peak day (lag=0). Maps show Z and ω at 250 hPa. The blue contour circles out the Sc area. Each row represents one timescale. The right column shows the cross-section averaged between latitudes marked by red ticks on the map. The thick blue and brown underlines of the cross-sections represent Sc areas and continents, respectively. The plots show perturbations after deseasonalization.

In the subtropics, the synoptic-scale Rossby waves are almost equivalent barotropic[2]. IG modes depict the vertical motion associated with these synoptic-scale Rossby waves, and no additional diabatic forcing is observed. To specify, the vertical motions are in quadrature with the geopotential heights, suggesting that ω here is not an initial perturbation but a response to vorticity advection in Rossby waves. This relation fits the expectation of the quasi-geostrophic theory.

The quasi-geostrophic ω equation including diabatic effects can be written as:

$$\underbrace{\left(\nabla^2 + \frac{f_0^2}{\sigma}\frac{\partial^2}{\partial p^2}\right)\omega}_{(1)} = \underbrace{\frac{f_0}{\sigma}\frac{\partial}{\partial p}\left[\boldsymbol{v_g}\cdot\nabla(\zeta+f)\right]}_{(2)} + \underbrace{\frac{R}{\sigma p}\nabla^2\left(\boldsymbol{v_g}\cdot\nabla T\right)}_{(3)} - \underbrace{\frac{R}{\sigma p}\nabla^2\left(\frac{T}{\theta}Q_{\mathrm{diab}}\right)}_{(4)}. \tag{3.5}$$

Here, σ denotes static stability, and f_0 denotes the reference Coriolis parameter on an f-plane. Term (1) is ω multiplied by an elliptic operator, which introduces a sign reversal between the forcing terms and the diagnosed ω for synoptic-scale perturbations. Term (2) represents vorticity advection changing with pressure levels. Term (3) represents the localized temperature advection (e.g., cold fronts), which is neglected in the Sc area. Term (4) represents the localized diabatic forcing, which is dominated by cloud-top radiative cooling in the Sc area.

On the east side of the Rossby ridge, negative vorticity advection (NVA) decreases with pressure (i.e., NVA is stronger aloft than below), resulting in a negative contribution from term (2). Through the elliptic inversion of the ω equation, this negative forcing corresponds to subsidence ($-\omega < 0$) east of the Rossby ridge. Conversely, term (2) becomes positive on the west side of the ridge, favoring ascent ($-\omega > 0$).

In addition, term (4) provides a negative forcing over the Sc region, consistent with the localized cloud-top radiative cooling shown in Figure A.4 (note that $Q = -Q_{\mathrm{diab}}$). As a result, subsidence is enhanced on the east of the Rossby ridge ($-\omega$ becomes more negative), while ascent is weakened on the west ($-\omega$ becomes less positive there). Hence, there is a east–west asymmetry of the ω associated with the Rossby ridge. This asymmetry can be seen in the contour lines shown in panels (b), (d), and (f) of Figure 3.4.

Under the Rossby wave perturbation, temperatures in the whole column adjust to be associated with geopotential height perturbations, to maintain hydrostatic balance:

$$T = -\frac{pg}{R}\frac{\partial Z}{\partial p}, \tag{3.6}$$

where R denotes the specific gas constant for dry air.

These high-frequency adjustments occur on the order of seconds to minutes, which is not captured by ω in the daily/monthly data. It explains why ω is a bad representative for this stability-changing process. Therefore, I refer to this mechanism controlling the vertical structure of temperatures as a column response to the high-pressure perturbations in the atmosphere. In the purely atmospheric-driving cases, EIS is controlled by this column response.

On interannual timescales (panels g–h in Figure 3.4), the low-frequency Rossby waves are coupled with a negative-phase Pacific decadal oscillation (PDO)-like SST pattern: cold SST anomalies along the eastern boundary, accompanied by warm SST anomalies in the central and western ocean basin. These cold SST anomalies in the east occur beneath the Sc area.

---

[2] Equivalent barotropic: barotropic in sign along vertical coordinates, while the amplitude varies with height.

As suggested by Figure 3.3, in typical cases, the strengthening of these cold SST anomalies controls the interannual variability of EIS. This control role is not in contradiction with higher pressure in the atmosphere, considering the coupling of atmosphere and oceans on interannual timescales. In other words, when both the atmosphere and SST vary in a PDO-like structure in internal variability, higher pressure aloft and cooler temperatures below occur simultaneously in the Sc area and enhance EIS.

3.3 Discussion

In Section 3.2, the large-scale mechanisms for EIS are updated from the local thermodynamics to the Rossby wave dynamics. The differences across timescales can be regarded as different wavelength and oscillation systems. Therefore, we can expect that free-tropospheric temperature changes (represented by θ'_{700}) correlate well with atmospheric Rossby ridge perturbations (represented by Z'_{250}), which is tested true looking back (see panel a in Figure 3.5).

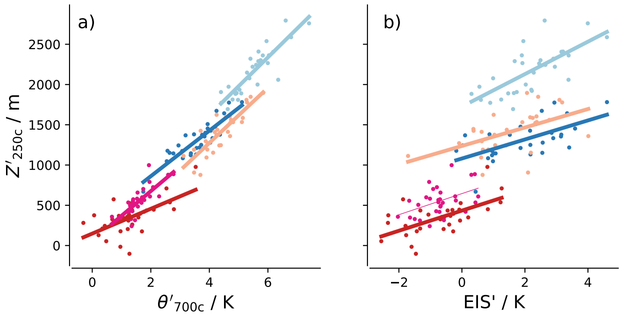

Figure 3.5: Interannual correlation plots between **a)** θ_{700} versus Z_{250}, **b)** EIS versus Z_{250}. The prime denotes anomaly from the annual mean in the corresponding regions. The other settings are similar to Figure 3.1.

Panel b in Figure 3.5 supports the coherent oscillations between low-frequency atmospheric systems and oceans. Therefore, without external forcing, the atmospheric Rossby ridges can be expected to correlate well with EIS also on long timescales.

This coherent oscillation case does not serve for the situations with external forcings, such as the annual cycle (solar forcing) and the fast response in the global warming scenario (greenhouse gases forcing). For those situations, the relative changes and competing effects between geopotential heights and SST in the Sc area need to be considered.

Moreover, in Chapter 1, we recognized the competing roles of subsidence and EIS. With the insights from this chapter, the relationship between subsidence and EIS can now be better understood. Large-scale subsidence is not the cause of enhanced EIS; instead, it acts as a secondary circulation compensating for extratropical Rossby waves. Hence, one can consider the relative influences of subsidence and EIS separately, without being overly concerned about their causal relationship in the Sc area. Spatially, as subsidence and EIS perturbations are not in phase, subsidence restricts cloud depth to the east of a case with increasing EIS, leading to a zonally asymmetric Sc enhancement.

4

OROGRAPHIC EFFECTS ON STRATOCUMULUS

Chapter 3 shows that, in the atmosphere-driven situation (synoptic and subseasonal timescales), synoptic-scale Rossby ridges control EIS. In this chapter, I will explain how the near-field orography influences these synoptic-scale Rossby ridges and, in turn, affects Sc (as sketched in Figure 4.1). The black arrows denote processes discussed in previous studies. Although there are still unclear parts regarding jet modification and the waveguide theory, delving into them is beyond the scope of this study. I only introduce the concept of those theories to show the broad picture of orographic effects. The blue arrows in the scheme denote the effects supported by my results.

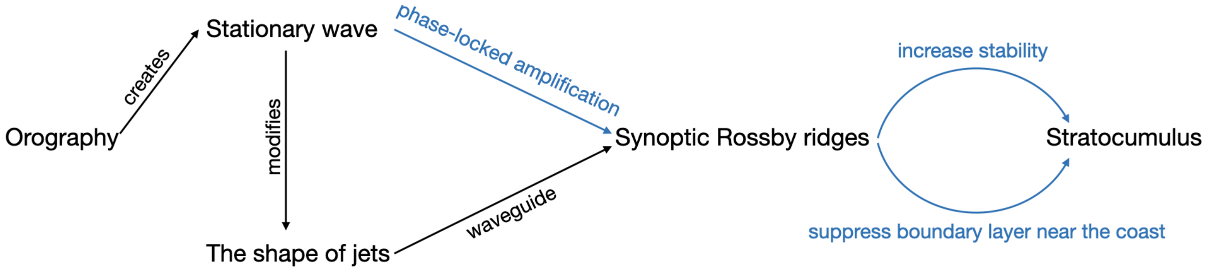

Figure 4.1: Schematic plot for orographic effects. Black arrows denote processes discussed in previous studies, and blue arrows denote processes supported by my results.

4.1 Influences on waveguides

The pioneer work of Charney and Eliassen (1949) demonstrates that orography can force stationary waves, leading to a worldwide adjustment of the zonal flow. To specify, large-scale orography induces a stationary ridge upstream, resulting in a wavenumber 3 planetary wave in the climatology of the Northern Hemisphere. In addition, although tropical heating does not directly determine subtropical stability (shown in Section 3.1), it can influence the strength and the meridional location of subtropical jets (Lee and Kim, 2003; Liu et al., 2021). The orographically forced stationary waves, together with the zonal distribution of tropical heating, are regarded as the key reasons for the shape of subtropical jets shown in panel a of Figure 4.2 (Lee and Kim, 2003; Riehl, 1961).

Lee and Kim (2003) further discussed how the strength and meridional location of the subtropical jet influence the synoptic-scale eddy generation region, which can be interpreted here as the polar front jet location. They show that as the subtropical jet strengthens and goes poleward, the synoptic-scale eddy generation region abruptly shifts from latitudes about 30° poleward of the subtropical jet to latitudes close to the jet itself (panel b of Figure 4.2).

Panel c of Figure 4.2 shows the subtropical and polar front jets in the ERA5 climatology. It aligns with the theories described above. In particular, points 1, 3, and 5 fit the expected wavenumber 3 structure of the subtropical jet (panel a), and the relative locations of the two types of jets between 1–2 and 3–4 are consistent with the conceptual results shown in panel b.

Furthermore, orography can induce a localized equatorward deflection of jets (Brayshaw, Hoskins, and Blackburn, 2009; Ringler and Cook, 1997; Rodwell and Hoskins, 1996). Such deflection is observed at points 6 (Mongolian Plateau) and 7 (Rocky Mountains) in panel c. This deflection effect provides an additional explanation for the merging of the two types of jets and their southwest–northeast tilts (see detailed discussion in Brayshaw, Hoskins, and Blackburn, 2009).

The above discussion shows the importance of orography in shaping jets.

As Sc regions are located in relatively weak subtropical jet regions, and according to the theory of Lee and Kim (2003), eddies are typically generated about 30° poleward of the subtropical jets. This theoretical expectation is supported by my regression results shown in panels d and e of Figure 4.2. Panels d and e show the synoptic-scale Rossby wave trains associated with EIS variability in Sc areas. These wave trains originate poleward of the subtropical jets and tend to travel equatorward on the sphere, until they are stopped by jets (Hoskins and Ambrizzi, 1993; Hoskins and Karoly, 1981). If the polar front jets are sufficiently strong, they can guide the Rossby wave trains for some distance (Wirth, 2020). In the regression results, Rossby wave trains do not cross the subtropical jets to the equatorward side. In the Southern Hemisphere (e.g., panel e), they follow the polar front jet for a longer distance and depart where the polar front jet is weaker (e.g., point 8 in panel c).

Therefore, climatological jets, which are shaped by orography, can provide an explanation for the propagation of synoptic-scale Rossby waves according to waveguide theory. The different features of jets result in regional differences in Sc. For example, SP and SA are typically located on the equatorward side of subtropical jets and therefore experience weaker perturbations from synoptic-scale Rossby waves. Consequently, these two regions have smaller Sc variability, as shown in Table 1.1. (See Appendix B for more regression results.)

4.2 Phase-locked amplification effect

The stationary waves induced by orography can produce a phase-locked amplification effect on selected wavenumbers. Using idealized simulations, Jiménez-Esteve, Kornhuber, and Domeisen (2022) show that large mountains preferentially amplify upstream Rossby waves with zonal wavenumbers 5 and 6, locally strengthening their ridges. A similar effect is found in ERA5 and ICON experiments analyzed in this study.

Figure 4.3 shows the synoptic evolution of composite high-LCC cases (above the 90th percentile) in ICON experiments. Compared to the noTopo run, the simulation including orography (i.e., Rocky Mountains for NP) shows significant local amplification of the Rossby ridge over the Sc area. This amplification persists for more than two days, allowing the positive Z' anomaly to remain longer.

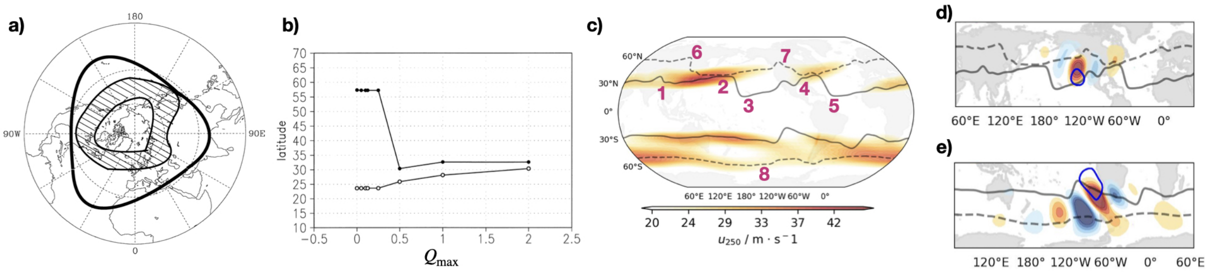

Figure 4.2: **a)** Northern Hemisphere view of the mean location of the subtropical jet (thick solid line) and area of principal activity of the polar front jet (shaded). **b)** Meridional locations of the subtropical jet (open circles) and the polar front jet (filled circles) in different tropical heating ($Q_{\max}$) experiments. Panels a–b) are borrowed from Lee and Kim (2003). **c)** 1987–2019 annual mean of 250 hPa zonal winds (u_{250}), subtropical jets (solid lines) and polar front jets (dashed lines). **d–e)** Geopotential height perturbation in Rossby modes associated with EIS on synoptic timescales at the peak day (lag=0). d) is the regression results for NP and e) is that of SP. Subtropical jets are identified by the maximum vertical shear between the u_{250} and u_{850} within 10°–40° latitude, while polar front jets are identified by the maximum u_{850} within 37°–65° latitude. A Gaussian filter with $\sigma = 5$ is applied for visualization.

As already discussed in Chapter 3, this positive Z' anomaly directly enhances stability in the whole column and increases EIS. Hence, the near-field orography leads to an asymmetry between synoptic-scale Rossby ridges and troughs. In climatology, this asymmetry manifests as larger EIS in Sc areas relative to their zonal mean state.

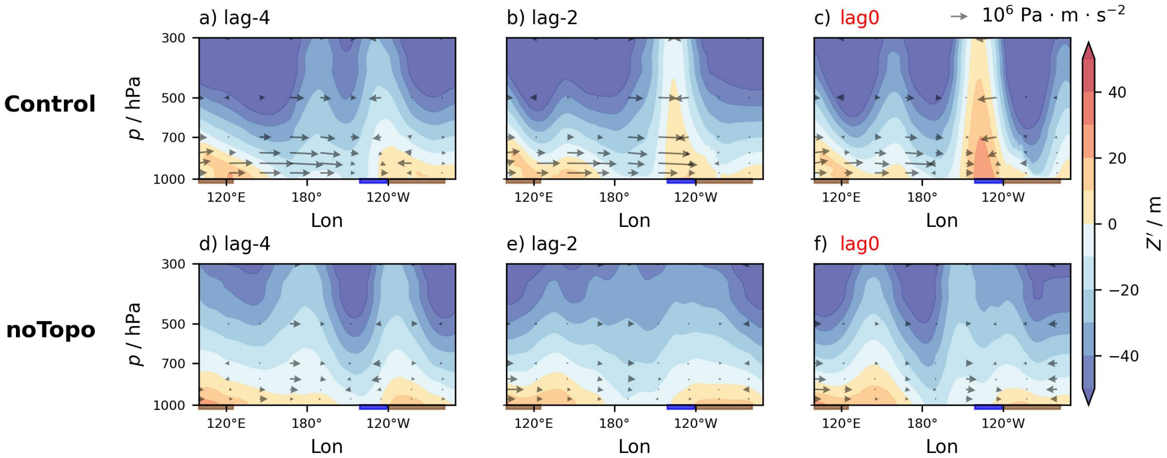

Figure 4.3: Zonal cross sections (21°–50°N) of geopotential height anomalies (Z') relative to the mean state for composite high-LCC cases in NP. Arrows denote the wave activity flux, with the vertical component multiplied by 10^5 for visualization. "Lag-4" denotes four days prior to the peak day. The upper row shows results from the control run, and the lower row shows those from the noTopo run. The thick blue and brown underlines of the cross-sections represent Sc areas and continents, respectively.

The amplified and long-lasting synoptic-scale Rossby ridges also modulate the boundary-layer height, contributing to the zonally asymmetric distribution of Sc. As shown in Figure 4.4, the coastal boundary-layer height decreases progressively during the synoptic evolution. This asymmetric boundary-layer height response is consistent with the subsidence area associated with a Rossby ridge perturbation. As discussed in Chapter 3, subsidence occurs along the eastern edge of positive Z', above the coast. The resulting suppression of the boundary-layer near the coast produces a zonal seesaw-like pattern in Sc distribution.

Previous studies identified this seesaw-like pattern and attributed it to the land/sea circulation (as introduced in Figure 1.2). Here, this view is updated by highlighting the phase-locked amplification effect on synoptic-scale Rossby ridges in a quasi-geostrophic atmosphere (on timescales beyond the diurnal cycle), as the noTopo run retains the land/sea contrast but lacks orographic elevations. This effect is observed not only in the synoptic evolutions but also in the three-year mean (see Figure C.2 in Appendix C).

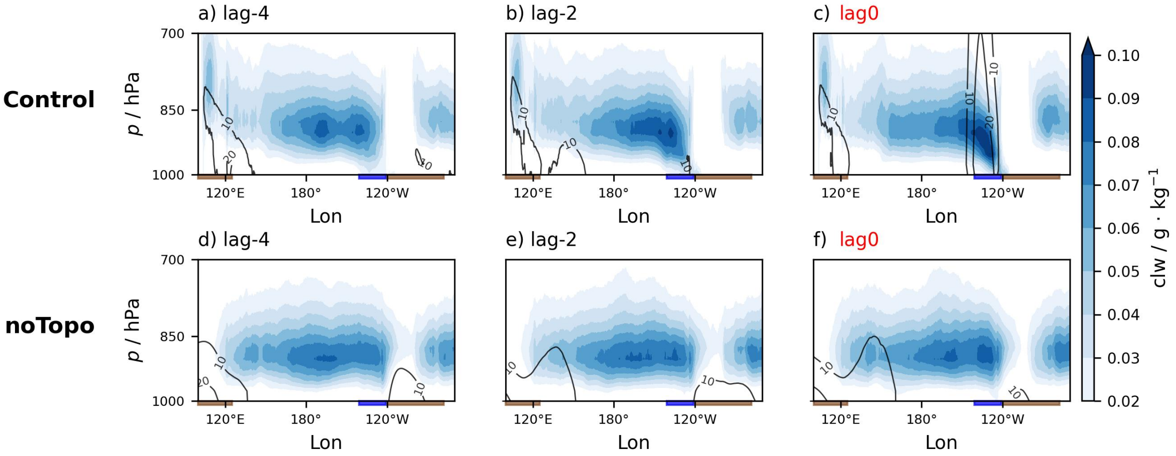

Figure 4.4: Zonal cross sections (21°–50°N) of cloud liquid water (clw) for composite high-LCC cases in NP. Contours lines denote Z', with only the 10 m and 20 m contours shown. All other settings are similar to Figure 4.3.

The amplified and phase-locked Rossby ridges leave a signature in the mean state, resulting in larger EIS in Sc areas. Figure 4.5 shows that removing the orography reduces Sc cover, particularly in regions with significant orography and previously larger Sc cover (i.e., NP with the Rocky Mountains, SP with the Andes, and SA with the South African Plateau).

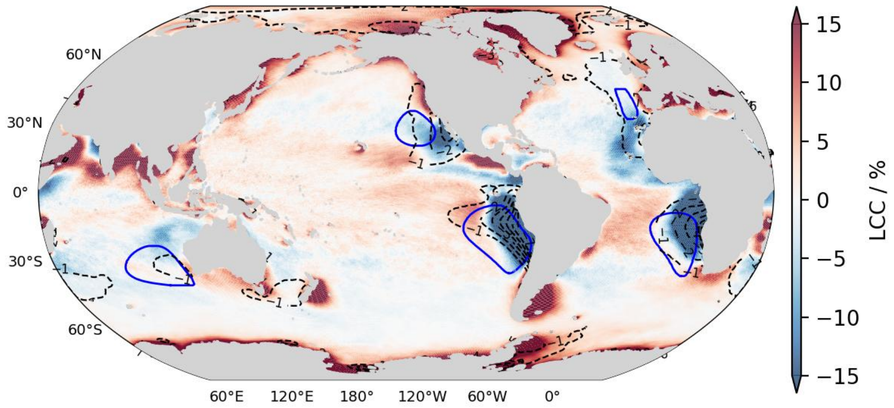

Figure 4.5: Three-year mean differences in LCC (colors) and EIS (contour lines) between the noTopo and control runs (noTopo minus control). Only contours below -1 are shown.

4.3 Discussion

Although local thermodynamics is too rough to explain EIS variability, it can contribute to the modification of waveguides as well. Liu et al. (2021) show that stronger tropical convection leads to a poleward shift and strengthening of the subtropical jets, which in turn affects the location of eddy generation and the propagation of synoptic-scale Rossby waves, as introduced in Section 4.1.

In addition, perturbations in tropical convection can redistribute absolute vorticity and induce a Rossby wave source in the subtropics (Sardeshmukh and Hoskins, 1988). The induced Rossby wave source associated with extratropical -PDO-like circulation influences the interannual variability of EIS (see Figure 3.4g in Section 3.2).

Therefore, tropical perturbations are suggested to have nonlinear effects on EIS and Sc variability.

5

DIFFERENT RESPONSES OF EIS AND SC TO LARGE-SCALE CIRCULATION

Having established the large-scale dynamical framework for EIS and Sc (without emphasizing their differences in previous chapters), it then becomes interesting to dive into the relationship between EIS and Sc. In this chapter, I will explain the different responses of EIS and Sc (represented by LCC) to large-scale circulation perturbations, which explains their weaker correlation, particularly on synoptic timescales.

Figure 5.1 shows that although both EIS and LCC are influenced by extratropical Rossby wave activity, they have different preferences regarding the location of Rossby ridges. EIS (red) is controlled by Rossby ridges located directly above it (referred to as local), whereas LCC (blue) is preferentially associated with Rossby ridges shifted about 10° upstream. These upstream Rossby ridges do not necessarily belong to the same processes as the local ridges.

In other words, the upstream preference of LCC is not due to a lagged response, which differs from previous assumptions. Previous studies assume that LCC prefers upstream high-pressure systems because of the large stability there, with cloud mass requiring about one day to adjust. However, this assumption is not supported: the lagged correlation between upstream EIS and local LCC is not higher than the simultaneous correlation between local EIS and LCC when carefully examined.

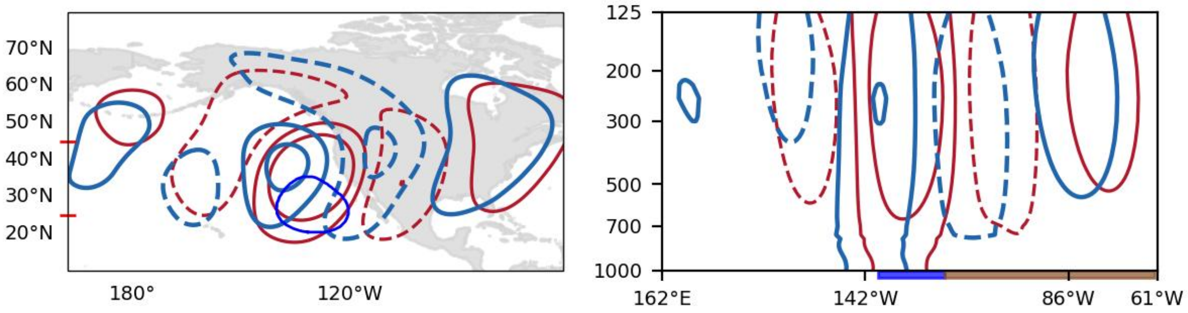

Figure 5.1: 250 hPa geopotential height perturbation in Rossby modes associated with EIS (red) and LCC (blue) at the peak day (lag=0). The right column shows the cross-section averaged between latitudes marked by red ticks on the map. The thick blue and brown underlines of the cross-sections represent Sc areas and continents, respectively. The plots show perturbations on synoptic timescales.

Table 5.1 further shows that, based on deseasonalized time series, high-EIS and high-LCC cases exhibit different seasonal distributions. High-EIS cases preferentially occur in winter, when extratropical eddies are more active. In contrast, high-LCC cases show a weaker seasonal preference. This contrast suggests that EIS and LCC depend on different physical conditions, even though the large-scale circulation patterns and dynamical framework are similar.

Table 5.1: Seasonal occurrence (%) of high-EIS and high-LCC cases identified from deseasonalized time series on synoptic timescales. Values indicate the occurrence in hemispheric winter (DJF in the Northern Hemisphere and JJA in the Southern Hemisphere) and summer (JJA in the Northern Hemisphere and DJF in the Southern Hemisphere), relative to the total number of cases.

	high-EIS		high-LCC	
	Winter	Summer	Winter	Summer
NP	34	11	32	12
NA	28	17	25	20
SI	33	13	28	18
SP	36	17	26	24
SA	40	9	27	20

5.1 Stronger winds

One of the key differences is that LCC prefer stronger near-surface winds, which enhances the boundary-layer cold advection[1] ($-T_{\mathrm{adv}}$) and evaporation (quantified by -LHF). While EIS is not controlled by stronger winds (tested in Section 3.1). Based on geostrophic balance, an upstream high can generate stronger winds in the Sc area by increasing the pressure gradient.

Figure 5.2 compares the synoptic evolution of T_{adv} and LHF in high-EIS (red) and high-LCC (blue) cases. It shows both stronger (about 40%) cold advection and larger (about 80%) latent heat flux favor more LCC. Cold advection can enhance boundary-layer turbulent mixing and increase Sc (Klein, Hartmann, and Norris, 1995; Scott et al., 2020; Wood and Bretherton, 2004). Evaporation provides a greater moisture supply. Here, I do not emphasize their relative contributions in increasing LCC, but note that both processes benefit from stronger winds. In the right panel, we see how the increased moisture supply offsets the drying effect of the Rossby ridge and helps maintain a moist boundary layer. Although Bretherton and Wyant (1997) suggest that larger LHF can lead to boundary-layer decoupling, this effect may be of secondary importance for LCC increasing, acting to limit further increases.

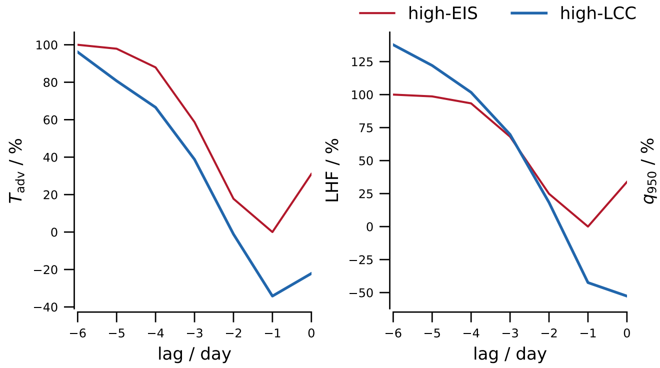

Figure 5.2: Synoptic evolution of T_{adv} (left), LHF (middle), and 950 hPa specific humidity (q_{950}, right) in NP composite high-EIS and high-LCC cases, based on deseasonalized time series. Values are averaged over the Sc region and normalized by the high-EIS range. Ranges for high-EIS cases: T_{adv} -2.1 to -1.5 $\mathrm{K} \cdot \mathrm{day}^{-1}$, LHF -125 to -111 $\mathrm{W} \cdot \mathrm{m}^{-2}$, and q_{950} 7.9 to 8.2 $\mathrm{g} \cdot \mathrm{kg}^{-1}$.

---

[1] Boundary-layer temperature advection is computed by: $T_{\mathrm{adv}} = -\boldsymbol{v}_{\mathbf{1000}} \cdot \nabla T_{1000}$, where $\boldsymbol{v}_{\mathbf{1000}}$ denotes the 1000 hPa horizontal wind vector, T_{1000} denotes 1000 hPa temperature.

5.2 Local SST cooling

In the previous view, EIS and LCC exhibit a lagged relationship, and their differences on synoptic timescales could be smoothed out when averaged over multiple days (Klein, 1997). As discussed above, they are not in a simple lagged relationship but have different responses to synoptic perturbations. I further test whether this difference can be smoothed out on long timescales.

Figure 5.3 suggests that the differences persist on long timescales. Comparing both the interseasonal and interannual patterns (panels b–e), LCC prefers upstream SST warming and associated upstream high, while EIS is more closely linked to local SST cooling and local high.

This discrepancy can be masked when the annual cycle is included. The winter-to-summer circulation change exhibits a negative phase of PDO-like pattern (-PDO-like), with upstream warming and relatively less temperature anomalies in the Sc area. This SST pattern, together with a zonally warmed free troposphere in summer, enhances EIS. Meanwhile, the upstream warming and associated upstream high also favor more LCC. As a result, both EIS and LCC increase through different mechanisms, leading to their stronger correlation on the annual cycle.

A similar confounding effect operates on interannual timescales. PDO-like oscillations influence both EIS and LCC. Such coupling between -PDO-like patterns and LCC is also supported by the simulations in Bellomo et al. (2014).

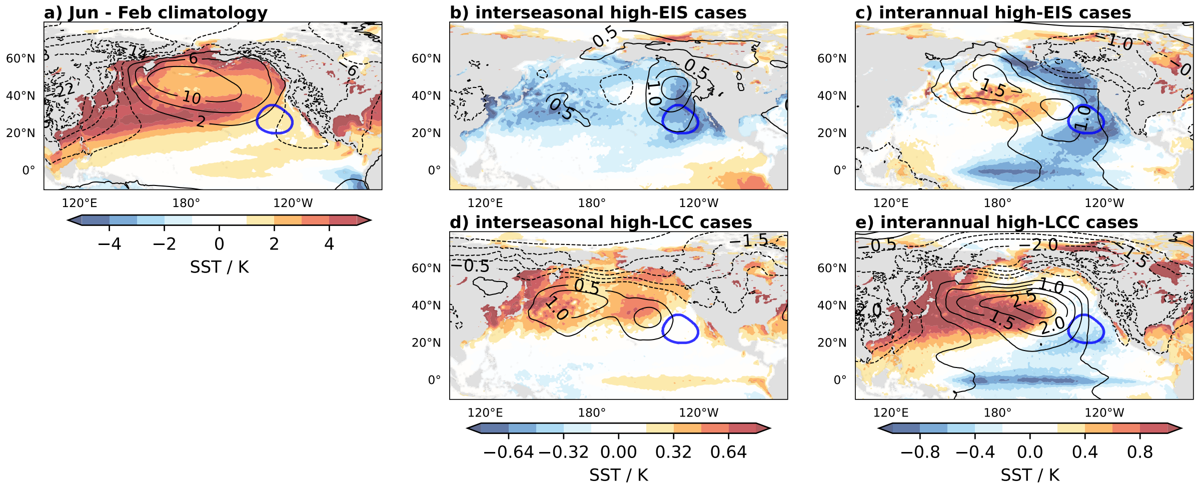

Figure 5.3: Maps of SST (filled contours) and SLP (contour lines) based on ERA5: a) difference between June and February in the climatology; b) anomalies from the climatological mean in the interseasonal high-EIS cases identified from deseasonalized time series; c) anomalies from the climatological mean in the interannual high-EIS cases; d–e) are similar to b–c) but for the high-LCC cases.

5.3 Discussion

Above results show that LCC is more associated with stronger winds (upstream high and upstream SST warming), while EIS is more associated with local high and local SST cooling (Chapter 3 and this chapter). Combined with Chapter 4, both local EIS and stronger winds serve to increase LCC. A confounding effect from -PDO-like SST patterns increases the co-variability between EIS and LCC on long timescales. It indicates an over-interpretation of the causality between EIS and LCC on long timescales and explains why previous studies found a questionable role of EIS in simulation experiments (Bretherton and Blossey, 2014; Qu et al., 2014; Webb and Lock, 2013).

When projected onto synoptic timescales, the preference of LCC for stronger winds manifests as a stronger correlation with conditions about one day earlier. This “one-day lead" is consistent with the wavelength of synoptic-scale Rossby waves, which require an upstream shift of about 10° to enhance the pressure gradient. On long timescales (i.e., interannual), when the dominant Rossby wavelength becomes longer, the correlation between LCC and upstream conditions can extend over greater distances and correspond to longer “time lags". However, on such longer timescales, lags of a few days are typically ignored. In this sense, the “one-day lead" does not reflect a mysterious adjustment timescale, but rather the spatial scale of the controlling Rossby waves.

The improvements to EIS proposed by Kawai, Koshiro, and Webb (2017) and Wang et al. (2023) can now be better understood. Their additional diagnostics implicitly reflect the influence of upstream highs from different perspectives. Specifically, Kawai, Koshiro, and Webb (2017) include moisture, which has the potential to reflect changes in LHF associated with stronger winds, although the humidity difference between 700 and 1000 hPa is not an ideal proxy for stronger winds. Wang et al. (2023) include boundary-layer height together with EIS, accounting for both effects of local EIS and the subsidence induced by upstream synoptic-scale Rossby ridges. Hence, their approach improves the correlation with LCC on synoptic timescales. However, both approaches, as well as the new findings in this study, still explain only about half of LCC variability using daily series. I would suggest that future studies pay more attention to the moisture pathway in response to stronger winds within the boundary layer.

Moreover, a key conclusion of this chapter is that EIS alone is insufficient to predict Sc. This is further supported by the CO_2 forcing experiments[2]: when SST does not change in a coherent -PDO-like pattern, the responses of EIS and Sc are decoupled. Figure 5.4 presents the ten-year mean responses in EIS (panels c and d) and Sc (represented by vertically integrated cloud liquid water and net surface solar radiation; panels e and f) to the SST pattern change. We see that Sc are more sensitive to the pattern change, as they are associated with upstream high, while EIS is more affected by local pressure.

---

[2] These experiments use the fully coupled MPI-ESM (Max Planck Institute for Meteorology’s Earth System Model) and are conducted by Moritz Günther. In those experiments, the CO_2 concentrations are fixed with locations and do not advect with air flow.

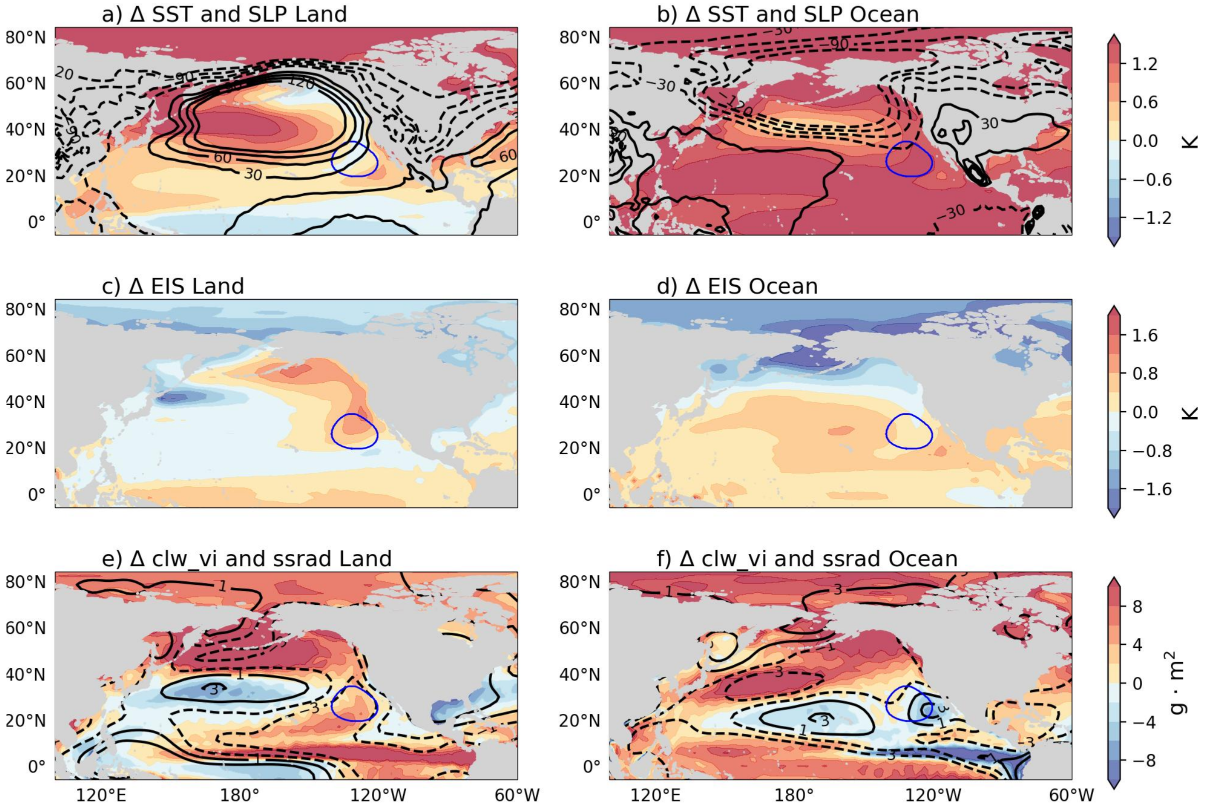

Figure 5.4: Differences in the abrupt 4 × CO_2 forcing experiments relative to the control run. The left column shows results for CO_2 forcing applied only over land, and the right column shows results for forcing applied only over oceans. a–b) Responses in SST (filled contours) and SLP (contour lines); c–d) responses in EIS; e–f) responses in vertically integrated cloud liquid water (clw_vi, filled contours) and net surface solar radiation (ssrad, contours). Blue contour marks the Sc area.

6

CONCLUSIONS

This dissertation establishes the relationship between large-scale circulation and subtropical stratocumulus (Sc). This is based on the investigation of reanalyses and satellite observations using various statistical methods and MODES to decompose different wave species. The findings are further supported by simulation experiments, providing a progressively revised and coherent view of the large-scale dynamics of Sc. The main contributions are summarized as follows.

1) The large-scale framework for subtropical lower-tropospheric stability is revised

It examines the previous large-scale view (local thermodynamics) of Sc and shows its limited role. Tropical heating cannot be regarded as a direct forcing of subtropical lower-tropospheric stability (EIS). Instead, it can be viewed as an indirect factor that modifies waveguides. EIS is controlled by extratropical Rossby waves, whose ridges increase stability in the whole column and enhance EIS in the meantime. The subsidence anomalies observed in the data mainly reflect the ageostrophic part of these Rossby waves and are not the key reason for EIS enhancement in Sc areas.

On synoptic and subseasonal timescales, EIS is dominated by atmospheric processes, such that synoptic-scale Rossby waves (extratropical eddies) are the key driver of EIS enhancement. On interseasonal timescales, both atmospheric processes and local SST are important, while local SST becomes dominant on interannual timescales. The increased importance of local SST does not induce competing effects with atmospheric Rossby waves (in the absence of external forcing), as the atmosphere and ocean covary in a Pacific Decadal Oscillation-like (PDO-like) structure on long timescales. Hence, without external forcing (e.g., solar forcing in the diurnal and annual cycles, or greenhouse gas forcing in more complex situations), EIS can be simply expected to covary with upper-tropospheric geopotential height.

2) The near-field orographic effect explains the zonally asymmetric distribution of Sc

The coastal orography (e.g., Rocky Mountains, Andes Mountains, South African Plateau) induces a phase-locked amplification effect on synoptic-scale Rossby ridges over the Sc area. This effect leads to a temporal asymmetry between synoptic-scale Rossby ridges and troughs. As EIS is mainly enhanced by these Rossby ridges, it is larger near the coastal orography (i.e., Sc areas) compared to its zonal mean. Hence, a large part of the high EIS, and therefore more Sc in the east flank of subtropical oceans, can be regarded as the footprint of the phase-locked and amplified Rossby ridges there. By removing orography in an AMIP experiment, we see more than a 15% decrease in Sc near large orography. (Note that this decrease does not account for the SST response in the experiment without orography.)

The phase-locked amplification effect also revises the previous view of the uneven boundary-layer height from the coast to the west open ocean. This unevenness is mainly due to subsidence on the east side of the amplified synoptic-scale Rossby ridges, rather than to additional subsidence forcing from land–sea circulation.

3) Different responses of Sc and EIS to large-scale circulation are identified

Unlike the previously assumed lagged response, LCC and EIS have different preferences for physical conditions. LCC prefers stronger winds (associated with upstream high and upstream warming), which can lead to enhanced boundary-layer turbulent mixing and greater surface evaporation. In comparison, EIS prefers local high and local SST cooling, which can increase local stability. These differences persist across timescales, suggesting that relying solely on EIS cannot explain all LCC increases.

Further statistical analyses (at the end of Appendix B) show that EIS variability can be mostly explained by local geopotential height and SST perturbations, while LCC is more complicated due to the responses of smaller-scale processes.

4) Explanations for puzzles raised in the introduction

The effects of subsidence and EIS are not contradictory, as their causal link is weak and both are associated with high-pressure systems (Rossby ridges) at different locations, together contributing to an uneven increase in the Sc area. Detailed discussions can be found in Chapter 3.

The location shift and strengthening of “subtropical highs" were found to be associated with Sc variability on short timescales, but discussions on long timescales are lacking. From my explicit test (Section 3.1), they are not associated on long timescales. This is because the detected system in previous studies actually reflects synoptic-scale Rossby ridges located upstream of Sc. When previous studies discussed this association, they focused on specific or composite high-LCC cases, where the association can be seen, but the source of the perturbation is not identified. If subtropical highs are defined in the traditional view (a consequence of zonal flow in the descending branch of the Hadley Cell interacting with orography), the synoptic-scale Rossby ridges overlap a part of subtropical highs, but they arise from different mechanisms and vary at different frequencies. Detailed discussion for the relationship between upstream synoptic-scale Rossby ridges and Sc can be found in Chapter 5.

The differences between EIS and LCC were discussed in point 3, explaining why EIS can show different changes from LCC in forcing experiments. More details regarding their difference can be found in Chapter 5.

Furthermore, why Sc is associated with conditions one day earlier rather than further back in time, and why improvements to EIS by including moisture and boundary-layer height are effective, can also be found in Chapter 5.

Overall remark: how should atmospheric motion be properly regarded for Sc variability?

In the introduction, I introduced that combining local thermodynamics with short Lagrangian trajectories is an important step forward in including atmospheric motion, but it still exhibits contradictions with observations and cannot explain the correlation between Sc and conditions one day earlier. Here, with the revised framework, large-scale conditions are suggested to be regarded fully dynamically, involving eddy perturbations and westerlies, rather than assuming steady-state forcing on longer timescales. Awareness of large-scale atmospheric motion and its local effects better explains the variability in EIS and the correlation between Sc and their upstream conditions when considering the wavelength.

7

OUTLOOK

Based on this study, subtropical stratocumulus variability can be interpreted within a framework similar to that of mid-latitude dynamics, while noting that low-frequency tropical processes can also influence the geopotential height there beyond dynamics (represented by vorticity).

Two future works are worth improving the understanding. One is to test if, without orography, the direct influence of tropical convections will become more pronounced on stratocumulus. This topic is initially investigated in ERA5 by comparing the stratocumulus area with an open-ocean area, but it is hard to separate the influence from jets in that comparison. Hence, investigating this in a slab ocean simulation of more than ten years could provide a good test. The outcome of that study can show whether mid-latitude dynamics only apply to the stratocumulus area due to orographic influence or whether it is a general framework throughout the subtropics.

Another work is to investigate the potential decoupling between stratocumulus and lower-tropospheric stability. In particular, it aims to understand whether changes in the adjacent SST pattern in future scenario experiments cause them to respond differently. The outcome of that study may explain part of the uncertainties among models regarding stratocumulus changes in future scenarios.

Part II

Appendices

A

FACTORS CAUSING STRATOCUMULUS TO DEVIATE FROM SUBTROPICAL HIGH VARIABILITY ON SEASONAL TO INTERANNUAL TIMESCALES

This work is published as: Ding, H., Stevens, B., and Schmidt, H. (2025). Factors causing stratocumulus to deviate from subtropical high variability on seasonal to interannual timescales. Atmospheric Chemistry and Physics, 25(18), 10511-10521. https://doi.org/10.5194/acp-25-10511-2025

Factors causing stratocumulus to deviate from subtropical high variability on seasonal to interannual timescales

Abstract

Stratocumulus (Sc) covers the eastern flanks of maritime subtropical high-pressure systems, and changes in their coverage can exert a radiative effect on the global energy budget comparable to that of a doubling of CO_2. Previous studies have identified the temperature difference between 700 hPa and the surface as the primary driver of Sc variability. However, the mechanistic linkages between subtropical highs and this critical temperature difference, which defines lower tropospheric stability, remain unresolved. While subsidence modulates temperatures at 700 hPa and wind-driven cooling affects surface temperatures, the observed decoupling between subtropical highs and Sc fraction on seasonal to interannual timescales lacks a mechanical explanation. This study uses reanalysis data to test two hypothesized pathways linking subtropical highs to the lower tropospheric stability. Results demonstrate that neither pathway dominates, as correlations between Sc-area temperatures and subtropical high dynamics exhibit strong regional and temporal dependencies. Additionally, Sc-area conditions do not systematically align with subtropical high variability, highlighting the need for further investigation into the dynamical processes governing temperatures in the lower troposphere.

A.1 Introduction

Stratocumulus (Sc), which covers around 20% of the low-latitude oceans, plays an important role in the global energy budget by reflecting solar radiation (Hahn and Warren, 2007; Warren et al., 1986, 1988; Wood, 2012). Previous studies have verified that changes in their fraction of only 3–5% can lead to effects commensurate with those from a doubling of atmospheric CO_2 concentrations (Hartmann and Short, 1980; Randall and Suarez, 1984; Slingo, 1990), a fact that has motivated a considerable amount of research, including this study, to understand what controls Sc variations and changes.

To understand the variation of Sc, one approach has been to identify and study cloud controlling factors (Stevens and Brenguier, 2009). Previous researchers have made progressive efforts to define such factors statistically. For instance, already a century ago it was appreciated that Sc are sensitive to the temperature and humidity difference between the surface and air above the clouds (Blake, 1928). It is now understood that the sensitivity to the temperature difference arises because this difference measures the stability of the Sc-top interface, whereby greater stability suppresses the entrainment velocity, which limits the entrainment drying that inhibits cloud formation. Likewise for a given entrainment rate, a drier free atmosphere implies more entrainment drying. Klein and Hartmann (1993) made these relationships quantitative by demonstrating a strong and linear relationship between lower-tropospheric stability (LTS), which they defined as the difference between 700 hPa and 1000 hPa, and variations in Sc amount across regions and seasons. Later, Wood and Bretherton (2006) introduced the estimated inversion strength (EIS) to account for differences in lapse rates that influence the relationship between θ at 700 hPa and its more pertinent value, which lies just above cloud top. They found that EIS explains the variation of low clouds across a wider range of temperature regimes, and hence latitudes, to provide good predictions across tropical, subtropical, and mid-latitude regions. Kawai, Koshiro, and Webb (2017) combined EIS with the humidity difference into a unified index which they called estimated cloud top entrainment index (ECTEI). They tested ECTEI using ship observations and found it correlates with the total low stratiform clouds (including Sc, stratus, and sky-obscuring fog) better than EIS. Apart from the role of temperature and humidity differences, a physical understanding of Sc identifies a variety of other physical factors, including, large-scale atmospheric subsidence (Randall and Suarez, 1984; Weaver and Pearson Jr, 1990), downwelling longwave radiation above clouds (Stevens and Brenguier, 2009), and sea surface temperature (SST) (Klein, Hartmann, and Norris, 1995).

Based on those factors, and from the spatial coincidence of Sc on the eastern-flanks of the semi-permanent subtropical high-pressure regions, an expectation arises that variations in these high-pressure regions will influence Sc. We identify two hypothesized pathways by which the variation of subtropical highs may affect neighboring regions of Sc. The first hypothesized mechanism would be that variations in the subsidence influence the free-tropospheric temperature above Sc, and hence Sc themselves, through enhanced adiabatic warming. If this hypothesis holds, it suggests that variability in Sc may be linked to remote monsoon regions. The pioneering work of Rodwell and Hoskins (1996) has shown a teleconnection between monsoons and subtropical subsidence described as a "monsoon-desert mechanism". Latent heat release from monsoonal convection generates a westward-propagating Rossby wave that enhances subtropical subsidence, subsequently influencing the free-tropospheric temperature. The second hypothesized mechanism is that variations in the steepness of the high, as measured by the zonal geopotential gradients from its mass center to the east coast, change surface temperatures through their effect on near-surface winds and the winds' consequent effects on surface currents, ocean upwelling, and surface cooling via wind-driven evaporation. Some evidence for such relationships exists, based on studies that have found Sc to co-vary with the subtropical highs on synoptic (George and Wood, 2010; Klein, 1997; Klein, Hartmann, and Norris, 1995; Toniazzo et al., 2011) and diurnal timescales (Ciesielski, Schubert, and Johnson, 2001; Duynkerke and Teixeira, 2001; Garreaud and Muñoz, 2004). However, these relationships are not particularly strong. Moreover, there is scant evidence for such relationships on seasonal and interannual timescales, in which LTS dominants Sc variation (Klein and Hartmann, 1993; Richter and Mechoso, 2004, 2006; Wood and Bretherton, 2006). A few studies that have addressed this question have found the subtropical highs to be less important than the LTS itself (McCoy et al., 2017; Qu et al., 2015; Zhou et al., 2015). The extent to which this holds up to a more systematic analysis, and if so whether it is due to confounding influences, or simply by the fact that the strength of highs is a poor predictor of the constituent terms of cloud controlling factors, as identified through a statistical analysis, is the focus of the present study. To test the first hypothesized mechanism, we analyze whether subsidence, characterized by ω_{700}, warms the free troposphere adiabatically. Similarly, $\frac{\partial \Phi}{\partial x}$ represents the steepness of the high in the second hypothesized mechanism, whose changes may influence wind stress, ocean upwelling, and surface temperature. Both factors are selected to describe the features of subtropical highs because they are physically connected to mechanisms proposed to influence EIS. Another commonly used factor for subtropical highs—sea level pressure (SLP)—is tested not to be a good representor for both ω_{700} and $\frac{\partial \Phi}{\partial x}$ to investigate the mechanical relationship between subtropical highs and EIS.

Specifically we test the two hypothesized pathways by which the subtropical high-pressure systems may influence cloud amount in the main Sc areas. This requires defining the main Sc areas and the high-pressure areas based on the data, as described in §A.2, and identifying whether the quantities hypothesized to be regulated by variations in the subtropical high are indeed the dominant cloud controlling factors. We first establish a metric for Sc amount (§A.2.2) and use this to investigate the contributions of the free-tropospheric and the surface pathways to the variation of Sc in §A.3.1. Then, the free-tropospheric pathway is tested in §A.3.2 and the surface pathway in §A.3.3. The investigation of free-tropospheric pathway follows the logic of how subsidence impacts adiabatic processes (Figs. A.4, A.5) and hence the potential temperature at 700 hPa (Fig. A.6). In addition, the surface pathway is tested through the impact of geopotential gradient on ocean upwelling and latent heat flux (Fig. A.7), and thus changes the potential temperature at 1000 hPa (Fig. A.8). Finally, the correlation between variables in the Sc and subtropical high areas is tested in §A.3.4. The conclusions drawn from our analyses are presented in §A.4.

A.2 Data and Methods

A.2.1 *Data*

This paper uses ERA5 (the fifth generation ECMWF atmospheric reanalysis, E5, Hersbach et al. 2017) data for cloud controlling factors and atmospheric conditions. Its data is provided on a $0.25^\circ \times 0.25^\circ$ grid, with three-dimensional fields on 37 pressure levels. The monthly mean of SLP, surface latent heat flux, wind components, vertical velocity, temperature, and geopotential heights are analyzed.

Low cloud fraction is analyzed based on the satellite data. This paper uses the second version of the ATSR-AATSR (Along-Track Scanning Radiometer and Advanced Along-Track Scanning Radiometer) data set in the Cloud_cci (European Space Agency Climate Change Initiative) project (Poulsen et al., 2017). The data are provided on a $0.5^\circ \times 0.5^\circ$ grid. In this paper, Sc amount is denoted by the symbol κ and defined to be equal to the low cloud fraction (cfc_low) in the identified Sc areas (see Section 2.A.2.2.1). ATSR-AATSR features a two-view radiometer with 7 channels and is one of a number of cloud climatologies that we chose because it is associated with essential climate variables (details are available at `https://space.oscar.wmo.int/instruments/view/aatsr`).

For the ATSR-AATSR data, monthly means for the period from January 2003 to December 2011 are analyzed and compared to ERA5 data over the same period. For the analyses of mechanisms that impact the cloud controlling factors, the 30-year ERA5 record, from January 1985 to December 2014, is analyzed. To fix terminology, our use of the term “seasonal cycle" denotes the monthly climatology, while the term “interannual" denotes the variations in specific monthly values across the record—July for the Northern Hemisphere and January for the Southern Hemisphere. These months are chosen because subtropical highs are at their peak intensity, and Sc reaches its maximum during the summertime, when the monsoon-desert mechanism intensifies subsidence in their vicinity. We have also examined the interannual variability during the winter season, and the results are consistent with those observed during the summertime period. The “climatological mean" refers to the average over all months for the thirty-year record. Hence, for the thirty-year ERA data, at each spatial location, the seasonal cycle has 12 data points, the interannual record has 30-point records, and the climatological mean has one data point.

A.2.2 *Definitions*

A variety of quantities arise in our analysis and are defined as described as follows. In addition to defining the areas over which the analysis is performed, and the various cloud controlling factors being considered, two additional quantities are defined as possible pathways by which the variation of the subtropical highs might influence cloud-controlling factors and hence cloudiness, κ.

A.2.2.1 *Marine subtropical highs and stratocumulus areas*

Marine subtropical highs are defined by the union of closed 1020 hPa contours of the climatological-mean SLP and marine areas. These are referred to subtropical high areas (H-areas) and denoted by color in Figure A.1. Five major regions can be identified across the globe, and these are named, respectively, North Pacific (NP), North Atlantic (NA), South Pacific (SP), South Atlantic (SA), and South Indian Ocean (SI).

Similarly, Sc areas (c-areas) are defined when the mean low cloud fraction of 9 years is greater than 0.5 (or 0.4 for NA) and falls within 45°N–45°S. c-areas are shown as thick black contours in Fig. A.1. Figure A.1 shows the c-areas are typically located eastward of H-areas.

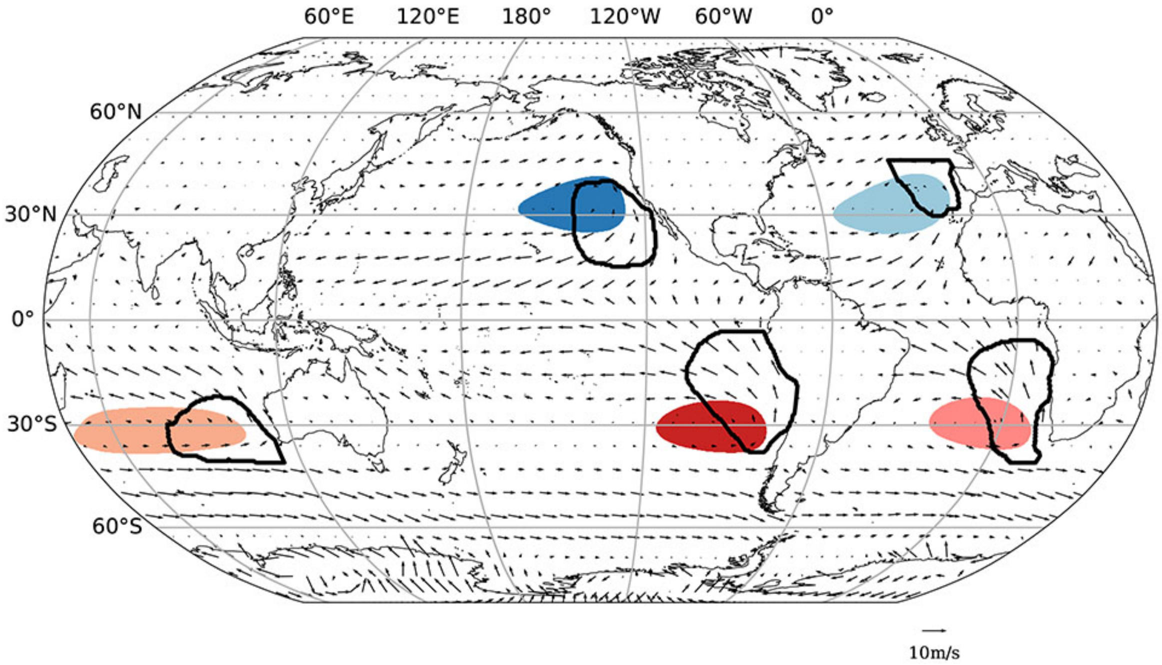

Figure A.1: The defined H-areas (shaded) and c-areas (thick black lines). The quivers denote 10 m wind field. Each color represents one region, and it is consistent in the later analyses. The map uses the Robinson projection.

This paper uses some similar words to address different concepts. “Regions" specifies the difference among NP, NA, SI, SP, and SA. “Areas" specifies the difference between H- and c-areas. Subscripts "H" and "c" represent the area over which the variables are averaged.

A.2.2.2 *Cloud controlling factors*

Previous studies suggested four factors to represent lower tropospheric conditions: the hydro-lapse ($\mathscr{H}$), LTS, EIS, ECTEI (Kawai, Koshiro, and Webb, 2017; Klein and Hartmann, 1993; Wood and Bretherton, 2006), as defined below:

$\mathscr{H}$: The hydro-lapse is defined as

$$\mathscr{H} = \beta \frac{l_\mathrm{v}}{c_p}(q_{700} - q_{1000}) \tag{A.1}$$

where β = 0.23, l_v is the latent heat of vaporization, c_p is the specific heat of air at constant pressure, and q is the specific humidity. Here, and throughout, a numeric subscript denotes the pressure level in units of hPa.

LTS: The lower-tropospheric stability is defined as:

$$\mathrm{LTS} = \theta_{700} - \theta_{1000} \tag{A.2}$$

where θ is the potential temperature.

EIS: The estimated inversion strength is defined as:

$$\mathrm{EIS} = \mathrm{LTS} - \mathit{\Gamma}_{850}\,(Z_{700} - \mathrm{LCL}) \tag{A.3}$$

where $\mathit{\Gamma}$ denotes the moist lapse rate, and $\mathit{\Gamma}_{850}$ is calculated by the average temperature of 700 and 1000 hPa. Z denotes the geopotential height. LCL is the lifting condensation level. To estimate the LCL we assume a constant surface relative humidity of 80%, consistent with Wood and Bretherton (2006). Based on the approximations $\mathrm{RH} \approx 100 - 5(T - T_\mathrm{d})$ and $\mathrm{LCL} \approx 125(T - T_\mathrm{d})$ with RH in %, LCL in m, and T and T_d in K, from Lawrence (2005), the difference between surface temperature and dew point is approximately 4 K, and the corresponding LCL is about 500 m.

ECTEI: The estimated cloud top entrainment index is defined as:

$$\mathrm{ECTEI} = \mathrm{EIS} + \mathscr{H} \tag{A.4}$$

Some recent studies re-evaluated LTS and EIS and found that they have little difference in their ability to describe cloud amounts and that this difference varies with data sources (Cutler, Brunke, and Zeng, 2022; Park and Shin, 2019). For this reason we re-examine the correlation between each suggested factor and κ to select the one that is the best predictor. Figure A.2 shows that EIS best explains variations in κ across all monthly means. Analyses of the same correlations on both the seasonal ($r = 0.93$) and the interannual ($r = 0.79$) timescales are consistent with the results based on all monthly means. Hence, EIS is selected for the following investigation. The performance of $\mathscr{H}$ is the worst. Even though $\mathscr{H}$ and κ are correlated at least in SP and SA, also in these regions the correlations weaker than those between κ and the other factors. This agrees with Klein and Hartmann (1993), which claims that moisture dominates the change of stratus in the Arctic but not for subtropical Sc. For this reason (which through a supplementary analysis we also confirm, but don't include here) the effects of subtropical highs on Sc through the influence of their variations on the the free tropospheric humidity are not explored further.

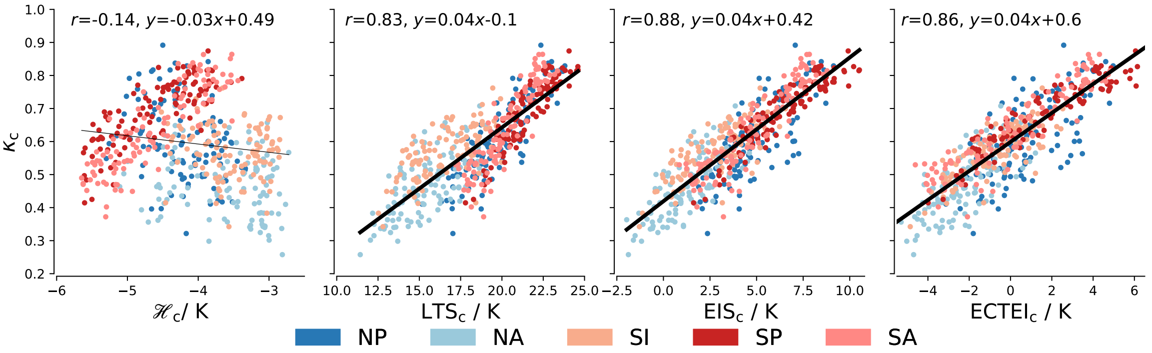

Figure A.2: Scatter plots of different cloud controlling factors and low cloud fraction (κ) from 2003 to 2011. Each scatter point represents a monthly mean, and the plots include 9 years of data, covering all 12 months per year. From left to right, the cloud controlling factors are $\mathscr{H}$, LTS, EIS, ECTEI, analyzed over the cloud (c) areas, as denoted by subscript. All subplots share the same y-axis, which represents κ, with each plot displaying data points colored by different regions. Regression lines are presented for p-values $\leq$ 0.05, and thickened when $r^2 \geq 0.25$.

A.2.2.3 *Adiabatic warming of lower-free troposphere*

For a stronger high-pressure we expect greater subsidence and more adiabatic warming, which in the mean would need to be balanced by increased radiative cooling or advection.

To explore the link between the lower-tropospheric potential temperature and the high-pressure regions we look to the thermodynamic energy equation. There, assuming stationarity, adiabatic warming (Q) must be balanced by diabatic warming/cooling (Q_{Diab}), such that:

$$Q = -Q_{\mathrm{Diab}} = -(\boldsymbol{v} \cdot \nabla\theta + \omega\frac{\partial\theta}{\partial p}) \tag{A.5}$$

Here $\boldsymbol{v} \cdot \nabla\theta$ denotes horizontal advection, with $\boldsymbol{v}$, the horizontal wind vector, and $\omega\frac{\partial\theta}{\partial p}$ describes vertical advection, with ω representing vertical (pressure) velocity, and p denoting the pressure. Q_{Diab} can be associated with the convergence of radiant energy, or through turbulent mixing associated with covariances arising from the use of mean quantities to form the budget terms.

A.2.2.4 *Wind driven surface cooling*

According to our second hypothesis, a high pressure system with a larger zonal geopotential gradient ($\frac{\partial\Phi}{\partial x}$) would be accompanied by a cooler surface. This could be due to a variety of mechanisms. First, it leads to more equatorward winds due to the geostrophic balance:

$$v = \frac{1}{f}\frac{\partial\Phi}{\partial x} \tag{A.6}$$

where Φ is the geopotential, x represents distance in the zonal direction, f is the Coriolis parameter, and we analyze $\frac{\partial\Phi}{\partial x}$ at 700 hPa.

The consequently increased surface wind-stress leads to more ocean upwelling and hence surface cooling. This upwelling is measured by the Ekman pumping velocity, w_{E}:

$$w_{\mathrm{E}} = \frac{1}{\rho_0 f}(\nabla \times \boldsymbol{\tau}) \cdot \boldsymbol{k}. \tag{A.7}$$

Here $\rho_0 = 1030\,\mathrm{kg\,m^{-3}}$ is the density of ocean water, and

$$\boldsymbol{\tau} = \boldsymbol{v_{10}} \cdot \rho_a C_D \|V\| \tag{A.8}$$

is the surface wind-stress, with $\rho_a = 1.225\,\mathrm{kg\,m^{-3}}$ the density of near-surface air, C_D the drag coefficient, $\boldsymbol{v_{10}}$ the near-surface (10 m) horizontal wind, and $\|V\|$ the near-surface wind speed. Since wind speeds are moderate in subtropical high and Sc regions, the drag coefficient C_D is assumed to be constant at 0.0012, following Large and Pond (1981). A positive value of w_E means upwelling motion, and a negative means downwelling motion. Different from other variables, the w_E is analyzed in a continuous area of positive w_E near the coast.

In addition, increased surface winds can also cool the surface through enhanced evaporation, which is measured by the latent heat flux (LHF).

A.3 Analysis

In this section we first explore what factors explain variations in EIS, which we now use as a proxy for cloudiness κ. We then explain to what extent these factors can be related to variations of the subtropical high-pressure regions.

A.3.1 *Dependence of EIS on θ_{700} and θ_{1000}*

EIS differs from LTS as it includes the temperature-dependent lapse rate Γ, but it is dominated by the variations of LTS (i.e., the difference between θ_{700} and θ_{1000}) because any change in lapse rates depends on the change of the temperature below 700 hPa. Table A.1 shows how these quantities vary across different regions and for different timescales and how much they contribute to variability in EIS.

In the higher latitude regions of the NP, NA and SI, variations of θ_{700} are mostly larger than variations in θ_{1000} in both the seasonal and interannual data and explain a large part of the variability in EIS in those regions, particularly on seasonal timescales. In these regions θ_{700} and θ_{1000} strongly co-vary across the seasonal cycle, but θ_{700} varies more. This means that EIS increases even as θ_{1000} increases, which explains the otherwise counterintuitive positive correlation between θ_{1000} and EIS in the higher-latitude regions on seasonal timescales. For the more equatorward regions of the SP and SA, variability of EIS is dominated by θ_{1000}, of which the variability is much larger than that of θ_{700} on seasonal timescales. This result is consistent with Klein and Hartmann (1993), who found that lower tropospheric stability covaries with θ_{700} in NP, NA, and SI, and with SST in other regions. Moreover, variations in θ_{1000} are important for all regions on interannual timescales (as evidenced by the correlations between θ_{1000} and EIS in Table A.1), and are particularly important for the main Sc areas of the NP, SA, as well as for the SI, where the standard deviations of θ_{1000} and θ_{700} are nearly equal.

This analysis demonstrates that variations in EIS are complex and regionally dependent. It also hints at why previous studies have not reported a strong relationship between the subtropical highs and cloudiness, as might be expected if, for instance, cloudiness was primarily controlled by either variations in the temperatures at the surface, possibly driven by surface winds and ocean upwelling, or aloft, possibly driven by atmospheric subsidence. Using $\omega_{700\mathrm{H}}$ as a factor of highs does not clearly indicate whether the variability of θ_{700} is larger or smaller

c-area	Seasonal Cycle						interannual Variability					
	$\theta_{1000\mathrm{c}}$		$\theta_{700\mathrm{c}}$		$\omega_{700\mathrm{H}}$		$\theta_{1000\mathrm{c}}$		$\theta_{700\mathrm{c}}$		$\omega_{700\mathrm{H}}$	
	r	σ/K	r	σ/K	r	$\sigma/\mathrm{hPa\,d^{-1}}$	r	σ/K	r	σ/K	r	$\sigma/\mathrm{hPa\,d^{-1}}$
NP	0.16	1.5	**0.64**	**2.6**	0.74	10.3	**-0.83**	0.6	0.76	**0.7**	-0.08	5.4
NA	0.26	2.4	**0.49**	**3.5**	0.88	5.3	-0.53	0.5	**0.75**	**0.8**	-0.23	3.2
SI	0.52	1.8	**0.79**	**3.3**	-0.82	8.1	**-0.84**	0.7	0.72	0.7	0.00	5.4
SP	**-0.97**	**2.0**	-0.73	1.0	0.04	4.4	-0.48	0.4	**0.85**	**0.9**	0.00	6.9
SA	**-0.94**	**2.0**	-0.52	1.1	0.59	3.7	**-0.66**	0.4	0.64	**0.5**	0.26	4.9

Table A.1: Correlation (r) with EIS and standard deviation (σ), respectively, for the quantities $\theta_{1000\mathrm{c}}$, $\theta_{700\mathrm{c}}$, and $\omega_{700\mathrm{H}}$ over the seasonal cycle and the interannual variability. The level with the higher correlation is denoted by bold font.

than that of θ_{1000}. For the seasonal cycle, the three regions with the largest variability of the high (measured by the standard variation of $\omega_{700\mathrm{H}}$ in Table A.1) are also the regions where θ_{700} varies more than θ_{1000}. However, this relationship does not necessarily indicate a causal link between subsidence rate in the high and θ_{700}, because it does not hold on interannual timescales. Moreover, the correlation between $\omega_{700\mathrm{H}}$ and EIS nearly vanishes, further suggesting that variations in atmospheric subsidence over H-areas are not the cause of changes in EIS.

To explore whether such relationships might exist, but are hidden by co-variability in other factors, we regress EIS against Q_c, the adiabatic warming in the cloud region, as well as two fields that could be indicative of the influence of the subtropical high on surface mechanisms, one being the $\mathrm{LHF_c}$, which we expect to co-vary with the surface wind speed, $\|V\|$, the other being ocean upwelling, w_E. Figure A.3 shows that some weak relationships emerge, as expected. Greater adiabatic warming, stronger winds (as measured by surface-latent heat fluxes) and more ocean upwelling all are positively correlated with increases in EIS. Because the relationships are generally stronger over the seasonal cycle as compared to the interannual record, it raises the question as to whether they are causal.

A.3.2 *Control by atmospheric subsidence*

Before exploring to what extent variations in the high-pressure regions can explain variations in θ_{700} we first examine the more basic question as to whether the adiabatic warming, which in stationarity balances the diabatic cooling Q, co-varies with ω_{700} in the Sc areas. Fig. A.4 demonstrates that there is a clear relationship between Q_c at 700 hPa and $\omega_{700\mathrm{c}}$ in the climatological mean (Fig. A.4). A strong and consistent relationship also emerges across the seasonal cycle and on interannual timescales (Fig. A.5). Hence $\omega_{700\mathrm{H}}$ is a good proxy for the adiabatic warming in the cloud areas.

Knowledge of the adiabatic warming is, however, not sufficient to determine θ_{700}. This is shown in Fig. A.6, which shows no consistent relationship between Q_c and $\theta_{700\mathrm{c}}$ across the seasonal cycle for the different regions, and no relationship between Q_c and $\theta_{700\mathrm{c}}$ whatsoever on interannual timescales. This indicates that $\omega_{700\mathrm{c}}$ is not the dominant factor for changes in θ_{700}, and falsifies the hypothesis that variations in $\theta_{700\mathrm{c}}$ can be explained by a monsoon-desert mechanism, at least one mediated by the adiabatic warming.

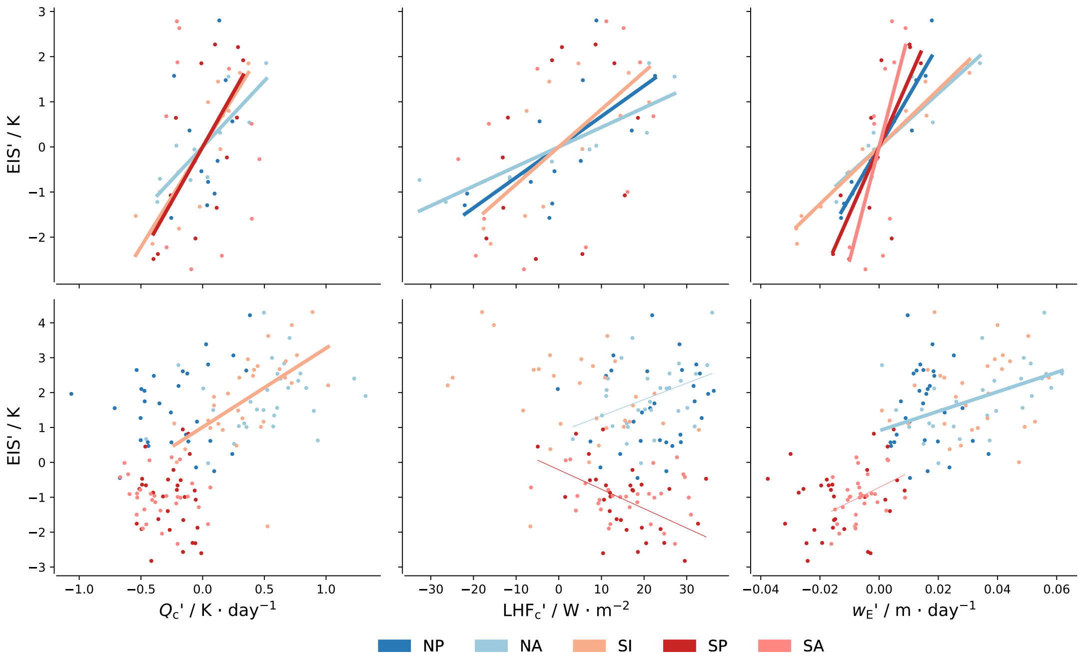

Figure A.3: Scatter plots of Q and EIS (left), LHF and EIS (middle), and w_{E} and EIS (right). The primes indicate deviations from the mean of the respective regions on the corresponding timescales. Each color represents a region. The top branch is for the seasonal cycle, and the bottom branch is for the interannual time series. Regression lines are presented for p-values ≤ 0.05, and thickened when $r^2 \geq 0.25$.

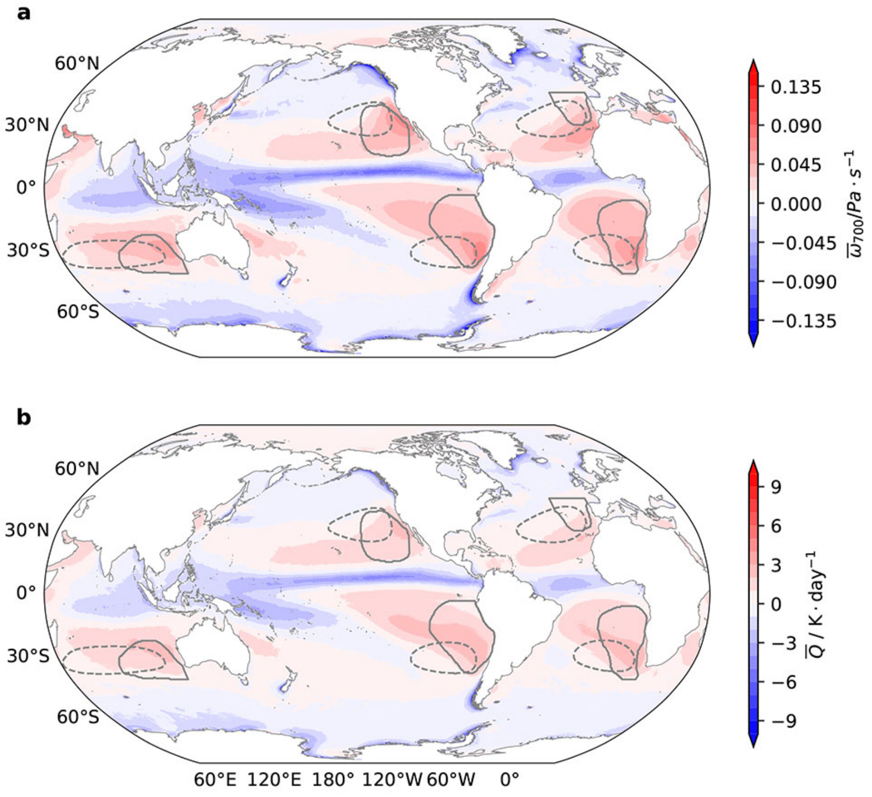

Figure A.4: Map of 1985–2014 climatological mean ω_{700} (top) and Q (bottom). Subtropical high areas are shown by dashed lines and cloud-regions are outlined by solid lines.

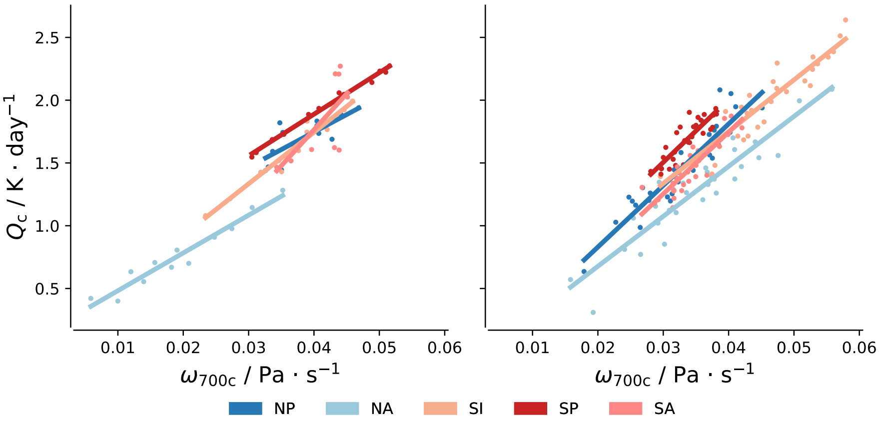

Figure A.5: Scatter plots of ω_{700} and Q. Subscript c denotes the mean value of the variable in the c-area. Each color represents a region. The left subplot is for the seasonal cycle, and the right subplot is for the interannual time series. Regression lines are presented for p-values ≤ 0.05, and thickened when $r^2 \geq 0.25$.

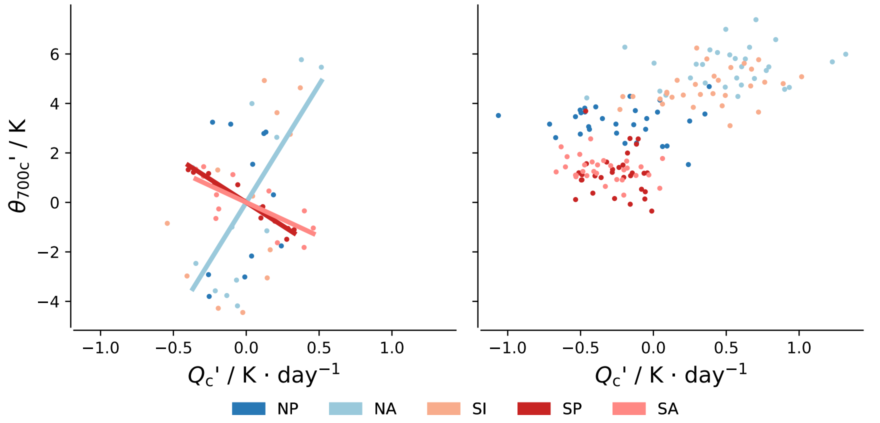

Figure A.6: Scatter plots of Q and θ_{700}. The primes indicate deviations from the mean of the respective regions on the corresponding timescales. Subscript c denotes the mean value of the variable in the c-area. Each color represents a region. The left subplot is for the seasonal cycle, and the right subplot is for the interannual time series. Regression lines are presented for p-values ≤ 0.05, and thickened when $r^2 \geq 0.25$.

A.3.3 *Control by wind-driven cooling*

In addition to subsidence rates, the steepness of subtropical highs is also proposed to influence EIS. As subtropical highs are typically located on the western flanks of Sc, the steepness of highs may affect the zonal geopotential gradient in c-areas, and thereby impact near-surface winds there. According to Sverdrup balance, the equatorward near-surface wind, which in geostrophic balance is determined by the zonal geopotential gradient ($\frac{\partial \Phi}{\partial x}$), is associated with a wind-stress gradient that results in ocean Ekman pumping (Anderson and Gill, 1975). In addition, the changed near-surface wind can also affect cold advection of waters from high-latitudes, and impact surface evaporative cooling as measured by the surface latent heat flux (LHF).

Figure A.7 shows patterns for mean $\frac{\partial \Phi}{\partial x}$, Ekman pumping velocity (w_{E}), and LHF. Unlike Q and ω_{700}, pattern correlations are difficult to discern. Ocean upwelling areas are restricted to the coastal regions where the wind-stress curl is large, and the maximum LHF is located on the west and equatorward side of the maximum $\frac{\partial \Phi}{\partial x}$ where temperatures are warmer and strong trade-winds prevail. A more quantitative evaluation of the relationship between $\frac{\partial \Phi}{\partial x}$ and either w_{E} or LHF (not shown), does not show strong and consistent relationships across regions or timescales. This leads us to conclude that variations in near-surface geopotential gradients are not the primary driver of changes in θ_{1000} (Fig. A.8) and hence variations in EIS.

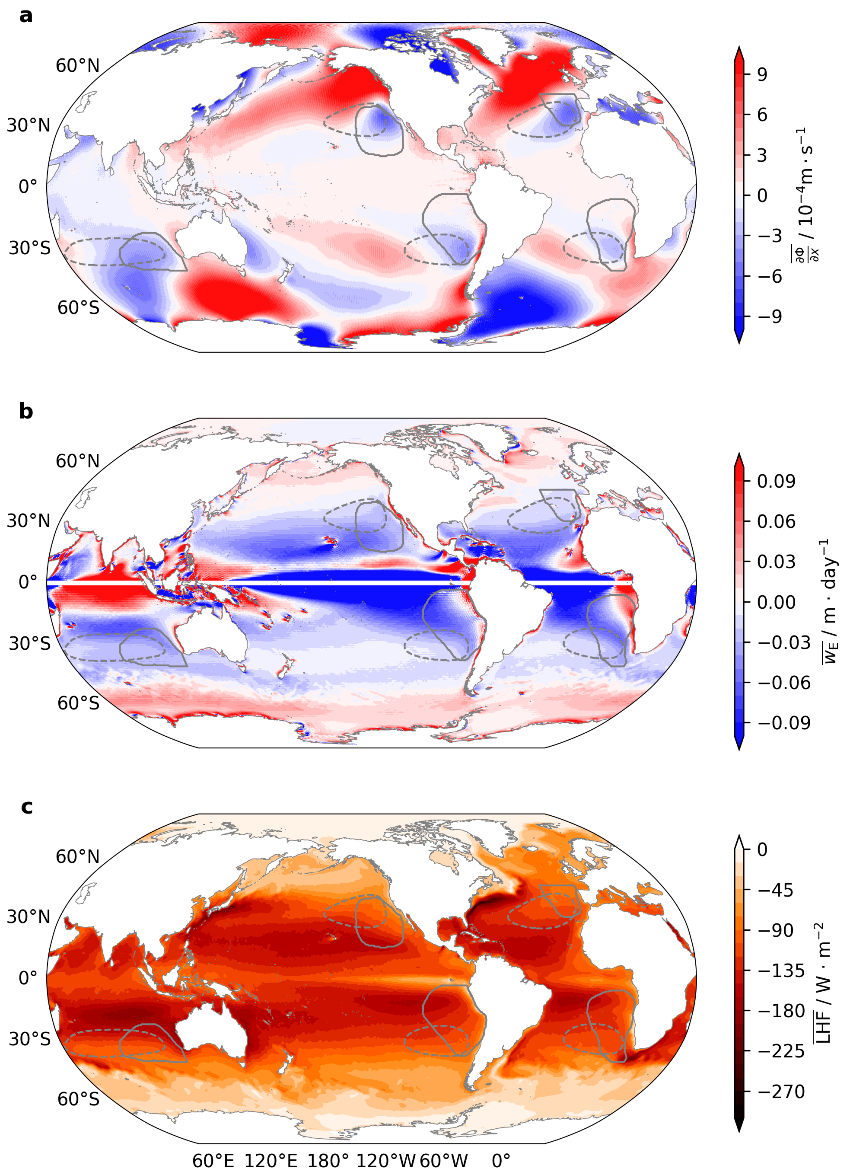

Figure A.7: Map of 1985–2014 climatological mean a. $\frac{\partial \Phi}{\partial x}$, b. w_{E} (masked within 1°N–1°S), c. LHF.

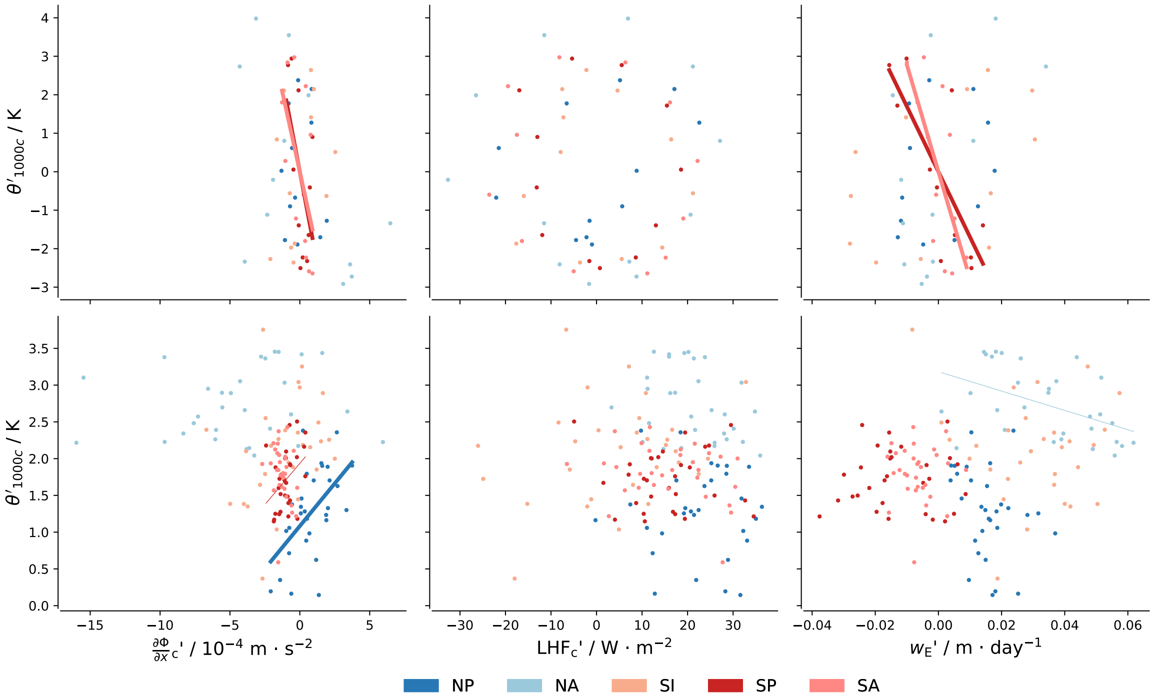

Figure A.8: Scatter plots of $\frac{\partial \Phi}{\partial x}$ and θ_{1000} (left), LHF and θ_{1000} (middle), and w_E and θ_{1000} (right). Subscript c denotes the mean value of the variable in the c-area, while w_E is averaged over the continuous ocean upwelling area near the coast. The primes indicate deviations from the mean of the respective regions on the corresponding timescales. Each color represents a region. The top branch is for the seasonal cycle, and the bottom branch is for the interannual time series. Regression lines are presented for p-values $\leq$ 0.05, and thickened when $r^2 \geq 0.25$.

A.3.4 *The disconnection between changes in H- and c- areas*

Until this point we have considered proxies within c-areas for the variation of H-areas that generally lie westward of c-areas. Figure A.9 shows that subsidence in c-areas is not necessarily a good proxy for subsidence in H-areas, and therefore not for the strength of the subtropical high represented by $\mathrm{SLP_H}$, as no rule for the relationships between H- and c- areas emerges. Correlations, when they exist can differ in sign across regions and for the same region across timescales. Even though the regression coefficients between the two areas show some similarity in NA across timescales, the correlations in the interannual time series are weak. Figure A.10 also shows that geopotential gradient in c-areas does not consistently correlate with SLP in H-areas. Therefore, the properties of c-areas that may affect EIS do not simply follow the strength of subtropical highs, which further reduces the probability of predicting Sc by the variation of subtropical highs.

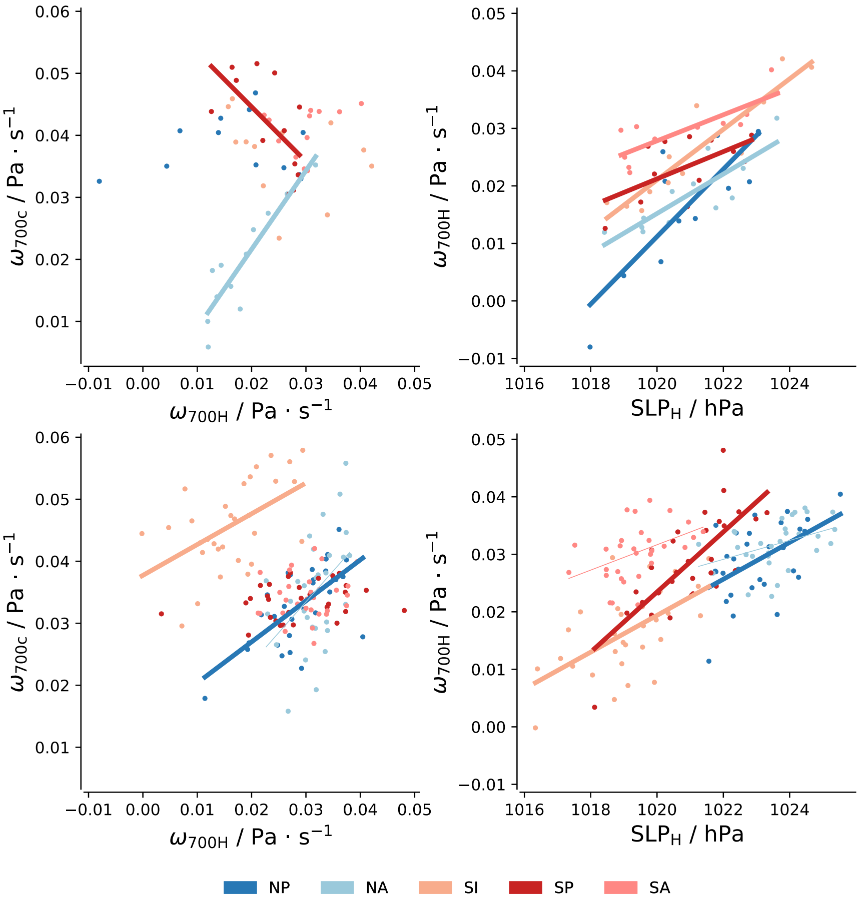

Figure A.9: Scatter plots of ω_{700} between H- and c- areas (left), and ω_{700} and SLP in H-areas (right). Each color represents a region. The top branch is for the seasonal cycle, and the bottom branch is for the interannual time series. Regression lines are presented for p-values $\leq$ 0.05, and thickened when $r^2 \geq 0.25$.

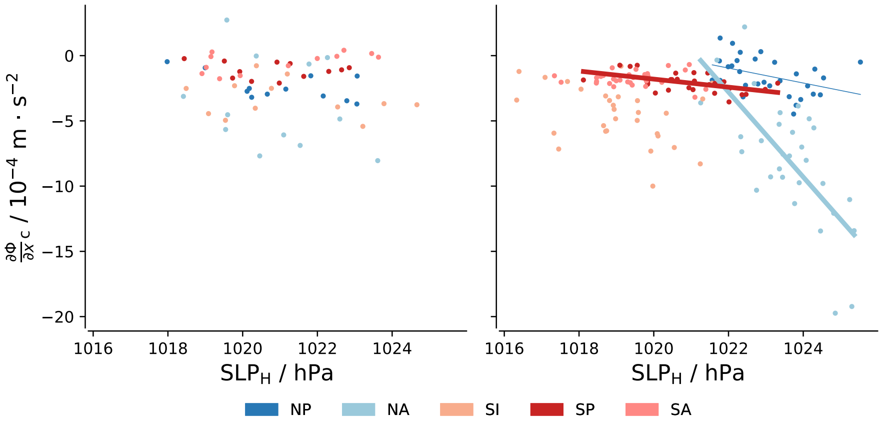

Figure A.10: Scatter plots of $\frac{\partial\Phi}{\partial x}$ in c-areas and SLP in H-areas on the seasonal (left) and interannual (right) timescales. Each color represents a region. Regression lines are presented for p-values $\leq$ 0.05, and thickened when $r^2 \geq 0.25$.

A.4 Conclusions

This paper tests two hypothesized mechanisms by which subtropical highs may affect Sc. Both hypotheses are rejected. Figure A.11 illustrates the relationships within the proposed mechanisms that are tested in this paper.

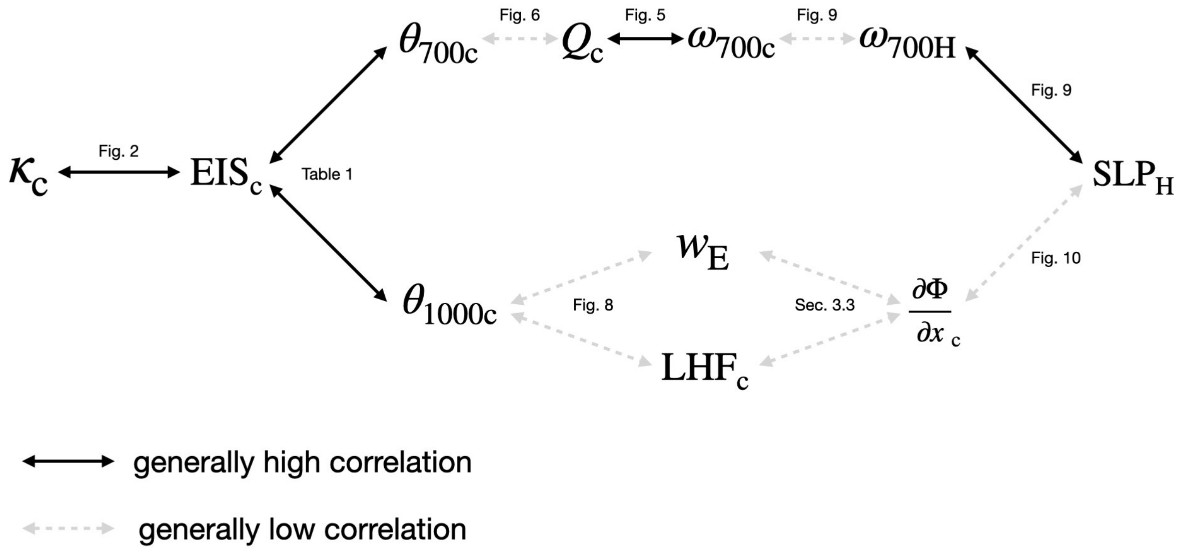

Figure A.11: Schematic representation of temporal correlations analyzed in this paper. Variables include: κ (cloud fraction), EIS (estimated inversion strength), θ (potential temperature), Q (adiabatic warming), ω (subsidence rate), SLP (sea level pressure), w_E (Ekman pumping velocity in the associated coastal ocean upwelling areas), LHF (latent heat flux), and $\frac{\partial\Phi}{\partial x}$ (700 hPa geopotential gradient). Subscript "H" represents the high-pressure areas and "c" represent the Sc areas. Arrows indicate a general relationship; please refer to the text for details.

First we define the marine high-pressure areas and the Sc areas by a surface isobar in the case of the former and a satellite derived cloud fraction in the latter. This identifies five regions, in each of which the high-pressure area intersects the Sc area, with the latter generally locates on the eastward flanks of the former. Next we demonstrate that Sc is well predicted by both the lower-tropospheric stability (LTS) and the Estimated Inversion Strength (EIS). A more recent proposal for a cloud controlling factor, the Estimated Cloud Top Entrainment Index, is more complex as it includes humidity variations and does not perform better than the EIS, as its additional skill arises from predictions outside of the main cloud areas we consider. Furthermore, in the areas we consider, and for any particular region, most of the variability in EIS can be explained by LTS alone.

Given these findings we hypothesize that EIS (or LTS) can be increased through an increase in adiabatic warming, Q, which maintains a higher potential temperature at 700 hPa. An enhanced subsidence in subtropical highs can lead to this increase in adiabatic warming. However, the variation of Q is not the dominant factor influencing changes in temperature above Sc (θ_{700}), as the correlation of θ_{700} and adiabatic warming can even be negative in some regions. This agrees with (Caldwell and Bretherton, 2009), which shows that the effects of the thermodynamic process are not warming the free troposphere directly; instead, it works more on enhancing the subsidence itself, which all things considered would maintain a shallower cloud layer.

We further hypothesize that the steepness of the subtropical highs could modulate Sc amounts through their effect on the surface momentum balance, and hence surface temperature, to which θ_{1000} is strongly related. A high with larger geopotential gradient in the Sc area is posited to increase surface wind speeds, enhancing ocean upwelling (w_E) along eastern coasts, accompanied by greater surface evaporation and cooling. If this mechanism were a dominant factor in controlling θ_{1000}, we would expect strong relationships between θ_{1000} and both w_E and latent heat flux (LHF), as well as a correlation between geopotential gradient and w_E, and even with LHF. However, there is little evidence supporting these relationships.

Environmental changes associated with variations in the subtropical high-pressure regions correlate better with LTS (and EIS) than they do with the components of the LTS and EIS the variations are thought to influence. On both seasonal and interannual timescales regionally unified positive correlations between Q and EIS, as well as between ocean upwelling velocity and EIS can be identified. We interpret this as indicative of variations in high-pressure regions not being the primary cause of variations in the Q, w_E or LHF, but rather indicative of hidden mechanisms that cause these quantities to co-vary with LTS. This finding is further supported by the lack of robust relationships between the variations in Q, w_E or LHF, in the high-pressure region and the same quantity in the partially overlapping cloud regions.

Our results do not support the hypotheses that an understanding of how the subtropical highs change with climate will be informative for how Sc amount will change in regions where such clouds prevail. It is well appreciated that the temperature control of the convecting areas on the moist adiabatic lapse rate throughout the tropics can influence the near tropical LTS (Betts, 1986; Manabe, Smagorinsky, and Strickler, 1965; Stone and Carlson, 1979). However, there is also a growing appreciation of the departures from the weak-temperature gradients that this mechanism relies on, which will continue to motivate efforts to identify dynamic factors influencing the LTS across the near tropics (Bao and Stevens, 2021; Singh and O'Gorman, 2013; Sobel and Bretherton, 2000; Sobel, Nilsson, and Polvani, 2001).

Data availability

The ERA5 reanalysis (Hersbach et al., 2017a) is available at `https://www.ecmwf.int/en/forecasts/datasets/reanalysis-datasets/era5`. The ATSR-AATSR dataset (Poulsen et al., 2017) is available at `http://catalogue.ceda.ac.uk/uuid/1ea3b2e391e4441daa57100a02b98691`.

Author contributions

HD did the data process and analyses, and wrote the original draft of this paper and edited it later. BS proposed the idea, restructured the paper, and wrote the analyses. HS reviewed and edited this paper, contributed to discussions, and helped guide the analyses.

Competing interests

The authors declare that no competing interests are present.

Acknowledgements

The German Climate Computation Centre (DKRZ) provided the reanalysis data and supercomputer used in this study. The authors appreciate their support for the data pool and server.

The authors also appreciate Hans Segura, Tiffany Shaw, Nedjeljka Žagar, Ian Dragaud, and Marco Giorgetta, who shared their thoughts that influenced this paper.

B

LARGE-SCALE CIRCULATION AND STRATOCUMULUS VARIABILITY

This work has been submitted to Weather and Climate Dynamics. Authors: Ding, H., Stevens, B., Lunkeit, F., Žagar, N.

Large-scale circulation and stratocumulus variability

Abstract
This study aims to understand the relationship between large-scale circulation and stratocumulus variability. We use reanalysis and satellite data to identify circulation patterns that couple with estimated inversion strength (EIS) and low-cloud cover (LCC) in stratocumulus areas. The results update the current understanding in two aspects: the limited direct influence of the tropical thermodynamic framework on stratocumulus, and the different responses of EIS and LCC to large-scale circulation.

Extratropical dynamics control EIS variability. From synoptic to interseasonal timescales (after deseasonalization), synoptic-scale Rossby ridges located directly over stratocumulus enhance stability throughout the tropospheric column and thereby increase EIS. On interannual timescales, planetary-scale Rossby waves coupled with a negative PDO-like (Pacific Decadal Oscillation-like) sea surface temperature pattern increase EIS. In contrast, LCC responds to circulation patterns similar to those associated with EIS, but with a systematic upstream (west and poleward) shift. This shift suggests a direct response of LCC to circulation through enhanced pressure gradients, which increase cold advection and offset the drying effect of Rossby ridges via stronger winds. The upstream Rossby ridges associated with increased LCC often overlap with the subtropical highs, which has led to the previous emphasis on thermodynamic processes that strengthen subtropical highs by enhancing the descending branch of the Hadley cell.

B.1 Introduction

Subtropical stratocumulus (Sc) play an important role in reflecting Earth's incoming solar radiation (e.g., Hartmann et al., 1992; Stephens, 2005; Wood, 2012). Understanding the mechanisms that control its variability is therefore essential for understanding the global energy budget. Sc, lying within the well-mixed boundary layer, are hypothesized to be controlled by lower-tropospheric stability (quantified by estimated inversion strength in this study, EIS). Stronger lower-tropospheric stability can suppress entrainment drying and favor more Sc (Stevens et al., 2001). Previous studies supported that hypothesis by a strong correlation between lower-tropospheric stability and Sc (quantified by low-cloud cover, LCC) on the annual cycle and interannual timescales (Klein and Hartmann, 1993; Wood and Bretherton, 2006). However, later studies with contradict results renew the discussion over the causality underlying this strong correlation. Myers and Norris (2013) found that EIS dominates the climatological variability in Sc, whereas Bretherton and Blossey (2014) suggested that EIS is less important for Sc changes in a warming climate. On shorter (synoptic and subseasonal) timescales, the correlation between lower-tropospheric stability and Sc also becomes weak. Klein (1997) found that no single factor can well represent the short-term variability in Sc. Klein, Hartmann, and Norris (1995), who observed a covariance between Sc and conditions from the preceding day near the subtropical highs, suggested that short-term variability in Sc corresponds to the strength of the subtropical highs.

Regarding the large-scale mechanism, early works proposed a tropical thermodynamic framework that linked Sc variability to the subsidence branch of the Hadley cell (e.g., Klein and Hartmann, 1993; Schubert et al., 1995; Siebesma et al., 2004). This however doesn't explain the regional maximum of subtropical highs over the eastern ocean basins. The regional maximum is instead thought to result from interactions between the zonal-mean flow and orography in winter, and from thermally induced extra subsidence in summer (known as monsoon–desert mechanism; Rodwell and Hoskins, 1996; Rodwell and Hoskins, 2001). The monsoon–desert mechanism states how off-equator convection warms the upper troposphere and induces a Rossby wave train toward the subtropical Sc area. They also discussed how that convection influences regions to the east through Kelvin waves and extends this mechanism to the whole globe. Later studies examining the influence of the monsoon–desert mechanism implicitly showed the uncertainty in regional responses (Chen et al., 2022; Chen, Hoerling, and Dole, 2001; Cherchi et al., 2014; Gaetani et al., 2011; Zhang et al., 2022; Zilli and Hart, 2021). In addition, Garfinkel et al. (2021) suggested that the method of Rodwell and Hoskins (1996), which fixes diabatic forcing to mimic monsoons, underestimates the nonlinearity of summer stationary waves. Nigam and Chan (2009) proposed that the influence of monsoons on subtropical highs is a secondary effect compared to the absence of winter storm tracks. As the effects of monsoons on subtropical highs remain debated, their influence on Sc is even more unclear.

Above discussion highlights the uncertain role of EIS and the tropical thermodynamic framework in influencing Sc variability. Furthermore, there are several questions remain. For instance, why does the correlation between EIS and LCC exhibit a dependence on timescale (1st paragraph)? If the timescale of cloud-mass adjustments is on the order of a week (Dong, Gregory, and Sutton, 2001), why does Sc respond to conditions one day earlier (Klein, Hartmann, and Norris, 1995), rather than to conditions further upstream? If the one-day-lagged covariance indicates an effect of subtropical highs on Sc variability, why is this covariance observed only on short timescales, but not on long timescales (Ding, Stevens, and Schmidt, 2025)?

This study aims to identify the large-scale mechanisms underlying Sc variability and to explain the above questions. The coupling between the LCC or EIS index time series and circulation variability is quantified through regression in global three-dimensional wave space. The spherical framework and the distinction between mid-latitude Rossby, inertia-gravity waves and equatorial waves provide a scale-dependent perspective on the dynamics underlying Sc variability. This study shows an important role of the extratropical Rossby wave dynamics, which can directly influence Sc. Details of data and wave-space analysis method are provided in §B.4. In the temporal domain, we decompose variability in synoptic, subseasonal, interseasonal and interannual timescales. The regression analysis is complemented by composite analysis; composites of high-EIS and high-LCC cases illustrate the different responses of EIS and LCC to similar large-scale circulation patterns (§B.5).

B.2 Data and Methods

B.2.1 *Data*

This study uses satellite observations for low-cloud cover (LCC) and ERA5 (the fifth generation European Centre for Medium-Range Weather Forecasts atmospheric reanalyses; Hersbach et al., 2017b) for other quantities. Daily mean data in the period 1987-01-01–2019-12-31 is used to investigate synoptic, subseasonal, and interseasonal variations; monthly mean data in the same period is used for analyzing interannual variations.

Satellite observations of cloud cover are taken from CLARA-A3 (the third edition of the Satellite Application Facility on Climate Monitoring's cloud, albedo, and surface radiation dataset from advanced very-high-resolution radiometer data) product by EUMETSAT (European Organization for the Exploitation of Meteorological Satellites; Karlsson et al., 2022). CLARA-A3 data is provided on a 0.25° × 0.25° spatial resolution and has long records (42 years), which benefits climate studies. It provides separate fractions for low-, mid-, and high-clouds, and we take the low-clouds fraction to quantify LCC.

ERA5 are obtained from DKRZ (Deutsche Klimarechenzentrum) data pool. It is in 0.225° × 0.225° horizontal resolution and 37 pressure levels. The regression analysis applies F128 Gaussian grids (512×256 points along latitude and longitude lines). Basic variables such as winds, geopotential height, sea surface temperature (SST), atmospheric temperature, sea level pressure (SLP), and surface latent heat flux (LHF) are directly read from ERA5. The other factors, such as relative vorticity, divergence, and potential temperature, are diagnosed by the MetPy Python package (version 1.7.0).

B.2.2 *Estimated inversion strength*

EIS is diagnosed following Wood and Bretherton (2006):

$$\mathrm{EIS} = \mathrm{LTS} - \Gamma_\mathrm{m}\,(Z_{700} - \mathrm{LCL}) \tag{B.1}$$

where $\mathrm{LTS} = \theta_{700} - \theta_{1000}$ is the potential temperature difference between 700 and 1000 hPa, Γ_m denotes the moist lapse rate at the average temperature of 700 and 1000 hPa. Z denotes the geopotential height at 700 hPa. LCL is the lifting condensation level, which is fixed to be 500 m in the calculation. This height is assumed based on a 80% surface relative humidity (RH), which is also what Wood and Bretherton (2006) does, and then it is calculated by $\mathrm{LCL} \approx 125(T - T_\mathrm{d})$ where $(T - T_\mathrm{d}) \approx (100\% - \mathrm{RH})/5$ following the approximation suggested by Lawrence (2005).

In this study, we use EIS to describe lower-tropospheric stability. Some studies also simply use LTS to describe that. The differences between LTS and EIS in their association with LCC are smaller than the data source difference (Cutler, Brunke, and Zeng, 2022; Park and Shin, 2019), which indicates that the difference between EIS and LTS are not important for the more tropical/subtropical regimes. Hence, we do not emphasize the distinction between the two indices.

B.2.3 *Timescale decomposition*

For variability within a year, we remove the annual cycle by subtracting daily climatology. The deseasonalized series are then decomposed into synoptic (< 15 days), subseasonal (15–90 days), and interseasonal (90–365 days) components. The synoptic component is derived by removing a 15-day running mean from the deseasonalized series. The subseasonal component is obtained using a band-pass filter defined as the difference between 90-day and 15-day running means. The interseasonal component is similarly obtained as the difference between the 365-day and 90-day running means. For interannual variability (> 1 year), we take a 12-month running mean of the monthly time series. Deseasonalization is not applied on the interannual series, as the 12-month running mean effectively removes the annual cycle.

B.2.4 *Wave-space regression between regional LCC/EIS and global circulation*

We study coupling between Sc and large-scale circulation by decomposing ERA5 data using the MODES software (Žagar et al., 2015). MODES performs a multivariate representation of the global circulation in terms of three-dimensional orthogonal vertical and horizontal structure functions — normal modes (i.e. eigensolutions) of the linearized primitive equations. A single mode is defined by three indices: zonal wavenumber k, meridional mode index n and vertical mode index m. For every n, there are three wave solutions: Rossby waves describing geostrophically-balanced circulation on the sphere, and eastward-propagating and westward-propagating inertia-gravity (IG) waves solutions (EIG and WIG, respectively). Two special solutions, equatorially-trapped Kelvin and mixed Rossby–gravity (MRG) waves are included as the lowest or $n = 0$ EIG and Rossby wave, respectively. The modal solutions for the zonal mean state ($k = 0$) follow Kasahara (1976). Our setup applies 200 zonal wavenumber, 19 vertical modes and 70 meridional modes for every wave types making a total of 210 meridional modes.

Vorticity-dominated MRG waves (Neduhal et al., 2024) and Rossby waves are collectively referred to as Rossby modes, and WIG and EIG modes including Kelvin wave are collectively referred to as IG modes. The tropical trapped MRG and Kelvin modes are included in the analysis because Sc areas are located in the subtropics and we also consider interannual timescales. Geostrophically balanced Rossby waves on the sphere have a small divergence associated with the β term, proportional to $v_g \beta / f$, where v_g is the meridional geostrophic wind. The isallobaric motions, i.e. most of ageostrophic dynamics related to the baroclinic Rossby wave dynamics, projects on the IG modes. This means that mid-latitude IG modes are a mixture of ageostrophic circulation, internal IG and gravity waves due to various sources and some coherent structure across scales that are not waves (see discussion in Žagar et al., 2023).

At each time step with data, modal decomposition produces a dimensionless expansion coefficient $\chi_n^k(m)$. Applied step-by-step to daily/monthly ERA5 data, MODES provides time series $\chi_n^k(m,t)$ that can be correlated with time series of EIS or LCC indices, denoted $\mathcal{I}$. The lagged regressions between $\mathcal{I}$ and $\chi_n^k(m,t)$, $\mathcal{R}_n^k(m,\tau)$, is computed as:

$$\mathcal{R}_n^k(m,\tau) = \frac{1}{N-1} \frac{\sum_{t=1}^{N} [(\chi_n^k(m,t+\tau) - \overline{\chi_n^k(m)})(\mathcal{I}(t) - \overline{\mathcal{I}})]}{\mathrm{var}(\mathcal{I})}, \tag{B.2}$$

where τ denotes the lag, N denotes the length of records, and var denotes temporal variance. The overbar in this equation denotes temporal mean.

We compute $\mathcal{R}_n^k(m,\tau)$ separately for $\mathcal{I}$ for each Sc area and for each of the time series isolating different timescales as described above. We also do the same regression for an open-ocean area in the subtropics in order to compare the near-field orographic effects. Indices t and τ are in days for the synoptic, subseasonal, and interseasonal series, and in months for the interannual series. The resulting complex variable $\mathcal{R}_n^k(m,\tau)$, a normalized covariance between circulation and Sc area index, can be projected back to physical space of 3D global wind and geopotential anomalies associated with variability represented by the index $\mathcal{I}$. Such filtering already identified circulation modes associated with the Madden-Julian Oscillation (MJO; Žagar and Franzke, 2015) and equatorial wave circulation coupled with a deep convection over the subtropical western North Pacific (Chen et al., 2025).

By limiting physical-space transformation of the complex vector $\mathcal{R}$ to elements associated with only Rossby or IG modes, we filter geopotential height (Z) and wind (u, v) perturbations associated with Rossby and IG waves, respectively. The IG-mode field filtered in this way is used to compute the vertical pressure velocity (ω) from the continuity equation, starting from the top level in the data (125 hPa).

The squared amplitude of the regression field, $gD_m|\mathcal{R}_n^k(m,\tau)|^2$, can be integrated along any dimension (k, n, or m) to provide the normalized covariance as a function of the remaining dimensions; for example, $\sum_m \sum_n gD_m|\mathcal{R}_n^k(m,\tau)|^2$ provides the zonal wavenumber distribution of the covariance between the global circulation and the $\mathcal{I}$. The multiplication factor gD_m consists of the gravity g and the equivalent depth D_m associated with vertical mode m, and it returns dimension of energy per unit mas (J/kg) to the covariance (removed in the process of projection). The covariance spectrum can further be split between Rossby and IG modes to identify both scales and wave dynamics associated with the $\mathcal{I}$. Here we note that each Sc area is normalized by a different variance meaning that their variance spectra, as well as u, v and Z anomalies for different $\mathcal{I}$ and timescales are not comparable in terms of amplitudes.

B.2.5 *Jet Identification*

The identification of polar front jets and subtropical jets follows the method of Liu et al. (2021) and uses 1987–2019 climatology. Polar front jets are detected by the maximum in zonal winds at 850 hPa, within 37°–65° N/S. Subtropical jets are detected by the maximum shear between 250 and 850 hPa within 10°–40° N/S. This method helps to separate polar front and subtropical jets based on the baroclinic structure of subtropical jets. Afterwards, we apply Gaussian smoothing with $\sigma = 5$ for visualization.

B.2.6 *Wave activity flux*

To diagnose energy propagation independent from wave phase, we compute the three-dimensional wave activity flux $\mathbf{F} = (F_\lambda, F_\varphi, F_p)$ following Takaya and Nakamura (2001), expressed in terms of wind components in pressure coordinates:

$$\begin{aligned} F_\lambda &= \frac{p\cos\varphi}{2\|\bar{V}\|}[\bar{u}(u'^2 - v'^2) + 2\bar{v}u'v'] \\ F_\varphi &= \frac{p\cos\varphi}{2\|\bar{V}\|}[2\bar{u}u'v' + \bar{v}(v'^2 - u'^2)] \\ F_p &= -\frac{p\cos\varphi}{\|\bar{V}\|}\frac{f^2}{N^2}(\bar{u}u'\omega' + \bar{v}v'\omega') \end{aligned} \tag{B.3}$$

where u, v, ω denote the zonal, meridional, and vertical velocity, respectively; p is pressure, φ is latitude, λ is longitude, and θ is potential temperature. The overbar denotes zonal mean, and the prime denotes deviation from zonal mean. $\|\bar{V}\| = \sqrt{\bar{u}^2 + \bar{v}^2}$ denotes zonal-mean wind speed, $f = 2\Omega \sin\varphi$ is the Coriolis parameter, and $N = \sqrt{(g/\bar{\theta})(\partial\bar{\theta}/\partial z)}$ is the Brunt–Väisälä frequency. Here g, Ω, a are the gravity, Earth's rotation rate, and Earth's radius, respectively. Negative F_p indicates upward wave energy propagation.

To avoid infinite values in the planetary boundary-layer, negative or near-zero values of N^2 were set to a very small value ($10^{-6}\,\mathrm{s}^{-2}$). This preserves the direction of vertical flux while stabilizing the numerical computation.

The fluxes $(F_\lambda, F_\varphi, F_p)$ were computed using daily data at each grid point, and they were saved as three-dimensional (p, φ, λ) arrays for subsequent composite analyses.

B.2.7 *Near surface temperature advection*

The near surface temperature advection (T_{adv}) is diagnosed by:

$$T_{\text{adv}} = -\boldsymbol{v_{1000}} \cdot \nabla T_{1000} = -\left(\frac{u_{1000}}{a\cos\varphi}\frac{\partial T_{1000}}{\partial\lambda} + \frac{v_{1000}}{a}\frac{\partial T_{1000}}{\partial\varphi}\right) \tag{B.4}$$

using central finite difference. Here $\boldsymbol{v_{1000}}$ denotes the 1000 hPa horizontal wind vector, T_{1000} denotes 1000 hPa temperature.

B.2.8 *Coherence*

We use the SciPy Python package (version 1.14.1) to compute the coherence between two daily time series from 1987–2019. This package is based on Welch's method, in which the time series is divided into overlapping segments and the Fourier transform is applied to each segment independently. Given a total record length of 12053 days, we choose a window size of 3000 days. This window size provides sufficient frequency resolution for interannual signal shorter than 7 years. With this window size and a 50% overlap, the significance thresholds of coherence are approximately 0.4 and 0.32 at the 95% and 90% levels, respectively. For visualization, we remap the coherence onto a logarithmically spaced frequency axis using linear interpolation. A 3-point running mean is then applied to the logarithmically spaced coherence to smooth the plots.

B.3 Overview of LCC and EIS

The climatology of low-cloud cover (LCC) and estimated inversion strength (EIS) show similar distribution patterns (Figure B.1 a–b). Five Sc areas (blue contours) are identified based on the climatological LCC exceeding 40% in the North Atlantic (NA) and 50% in other regions, including North Pacific (NP), South Indian Ocean (SI), South Pacific (SP), and South Atlantic (SA).

Beyond the spatial pattern, panel c of Figure B.1 shows the coherence between LCC and EIS across timescales. Their coherence is strong on interseasonal (90–365 days) and interannual ($>$ 365 days) timescales, with a peak at the annual cycle (around 365 days). The coherence on synoptic ($<$ 15 days) and subseasonal (15–90 days) timescales is weaker and slowly increasing going from day-by-day to seasonal timescales.

The coherence between EIS and potential temperatures (θ) in panel d, provides insight into its controlling processes. It suggests that EIS is dominated by free-tropospheric processes on synoptic and subseasonal timescales, while the influence of θ_{1000} becomes important on longer timescales.

Based on c and d, we decompose the original daily series of EIS and LCC into four components: synoptic, subseasonal, interseasonal, and interannual (see method in §B.2.3). Even

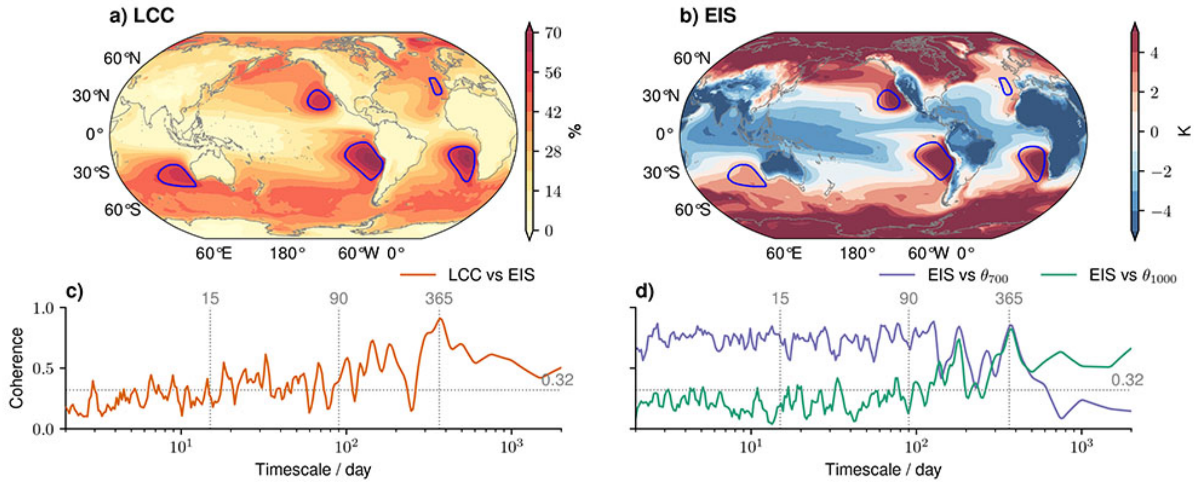

Figure B.1: LCC (a) and EIS (b). Blue contours mark Sc areas (climatological LCC exceeding 40% in the North Atlantic (NA) and 50% in other regions). c) coherence of LCC versus EIS across timescales. d) coherence of EIS versus θ_{700} and θ_{1000} across timescales. c–d) use the mean time series over the five Sc areas. It represents the common features across Sc areas (Figure S1 in the Supplement). Coherence exceeding 0.32 are significant at the 90% level. The computation and smoothing method for coherence is introduced in §B.2.8.

though there is no clear boundary between synoptic and subseasonal coherence, the 2-week timescale is typical for weather prediction as an initial-value problem and is associated with traveling, synoptic-scale baroclinic Rossby waves, whereas variability on subseasonal timescales is coupled to quasi-stationary, planetary-scale waves. The variance for each series of LCC after that decomposition is shown in Table B.1. Synoptic and subseasonal variability accounts for the major part of LCC variability. To note, as we use running mean to perform timescale decomposition, the values are approximate variances for each timescale. We also quantified variances on each timescale through the Fourier series decomposition (Table S1). It also shows that synoptic and subseasonal variability account for the majority of LCC variability, while the subseasonal variances are more comparable to that of synoptic timescales.

Table B.1: Variance of LCC (unit: %) for each time series. The subscription ‘orig’ denotes the original daily series; ‘deseas’ denotes the series removing daily climatology; ‘synoptic’, ‘subseasonal’, ’interseasonal’, and ‘interannual’ denote the respective series introduced in §B.2.3.

	σ^2_{orig}	σ^2_{deseas}	$\sigma^2_{\text{synoptic}}$	$\sigma^2_{\text{subseasonal}}$	$\sigma^2_{\text{interseasonal}}$	$\sigma^2_{\text{interannual}}$
NP	492	331	192	76	18	15
NA	501	461	272	106	27	11
SI	279	252	165	50	14	8
SP	221	120	66	25	10	7
SA	247	150	91	30	9	7

B.4 Circulation controlling EIS and LCC on different timescales

This section shows the identified circulations controlling EIS and LCC for each Sc area (see the method in §B.2.4).

Figure B.2 shows the zonal wavenumbers spectra of the normalized circulation covariance associated with LCC. Synoptic-scale ($k = 4$–8) waves play the dominant role on synoptic timescales in all seasons and regions. These synoptic-scale waves remain important on longer timescales (subseasonal and interseasonal) and still pronounce as a secondary peak on interannual timescales, while planetary-scale ($k = 1$–3) waves become increasingly important toward longer timescales.

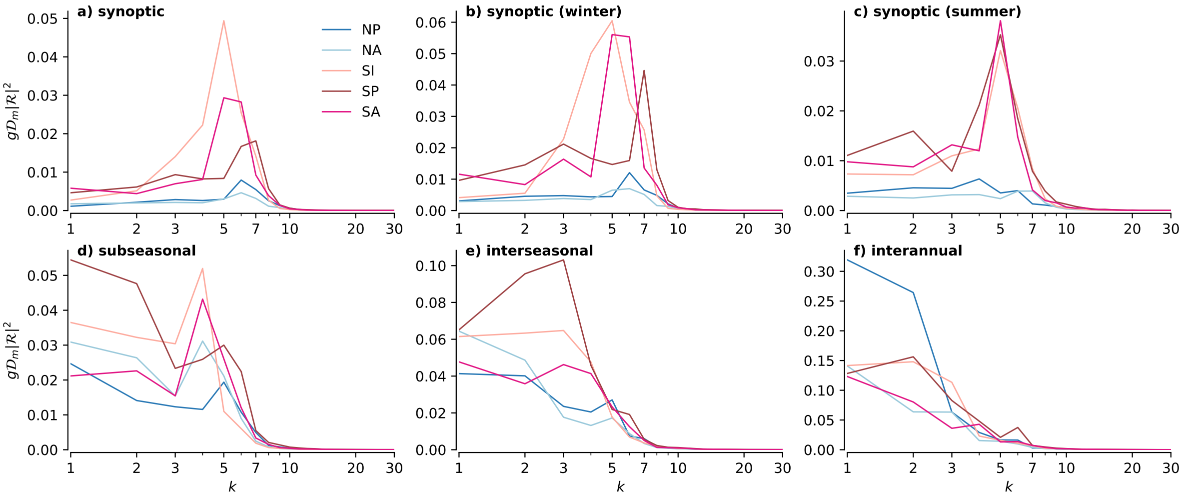

Figure B.2: Zonal wavenumber (k) distribution of the covariance between global circulation and LCC for Rossby modes, with each region represented by a different color. See §B.2.4 for details of the method. (Version for EIS in Figure S2.)

B.4.1 *Synoptic timescales*

Figure B.3 shows synoptic-timescale Rossby-mode geopotential height perturbations. Each row represents one region. We see that the circulation controlling synoptic EIS and LCC variability is an extratropical Rossby wave, with spatial scales reflecting Fig. B.2a. An important difference between EIS and LCC is that the LCC-related Rossby wave (contour lines) is somewhat shifted upstream relative to that associated with EIS (filled contours). This location shift indicates that peak LCC variability preferentially occurs in the upstream Rossby wave ridge position, rather than collocated with it. We will return to the reason for this upstream preference in §B.5.2.

A synoptic-scale Rossby wave from upstream (west and poleward) originates several days ahead and propagates energy downstream. The zonal scale of this wave is equivalent to $k = 5$ wave (Figure B.2a). The signal is localized, as the $k = 5$ Rossby waves are rarely circumglobal. On day 0, a Rossby ridge around Sc areas influences EIS and LCC. This ridge is associated with anticyclonic-wind perturbation (not shown). The vertical cross-sections indicate that this Rossby wave is almost barotropic but has a maximal amplitude in the upper troposphere. Later in §B.5.1, we discuss how this Rossby ridge increases EIS.

Behaviors of the synoptic-scale Rossby wave are influenced by both jets and orography. The subtropical jets (solid thick line) and the polar front jets (dashed thick line) act as waveguides for the synoptic-scale Rossby wave (Polster and Wirth, 2023). Rossby waves on the sphere tend to propagate equatorward unless stopped by jets (Hoskins and Ambrizzi, 1993; Hoskins and Karoly, 1981; Wirth, 2020). Due to the waveguide, synoptic-scale Rossby waves cannot fully reach the Sc areas that are closed to the equator (i.e., SP and SA). Therefore, SP and SA show smaller synoptic variability (Table B.1), as they are less perturbed.

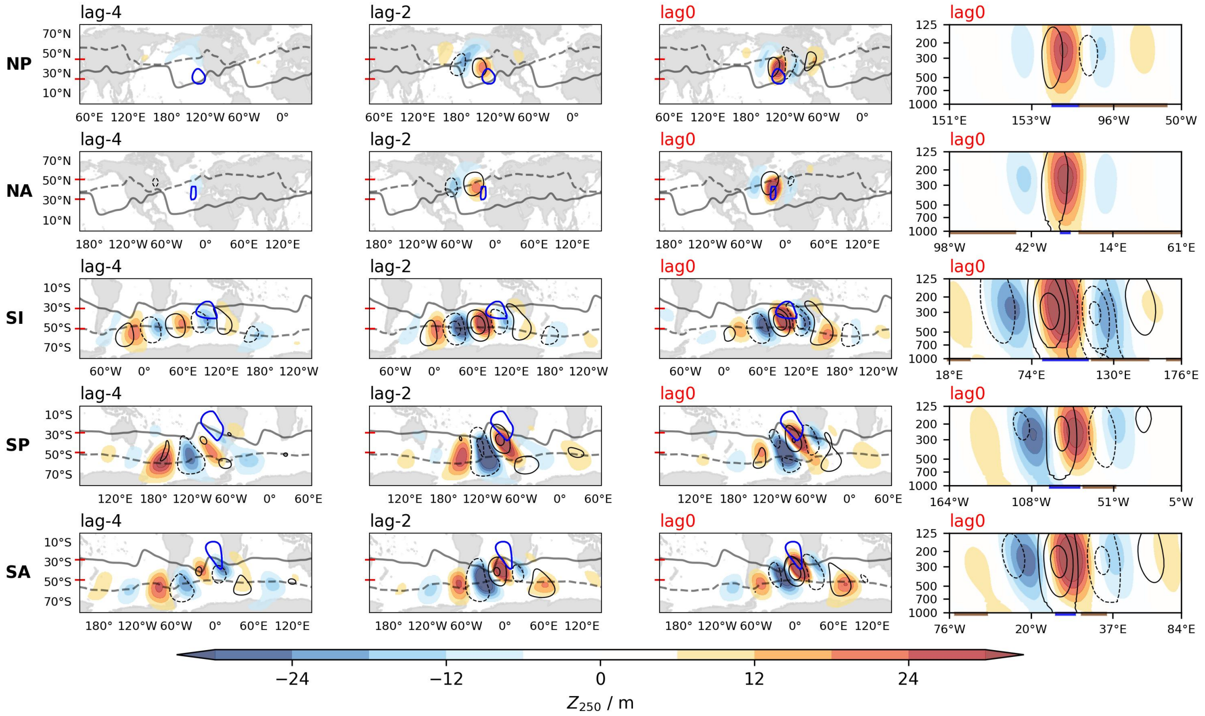

Figure B.3: Geopotential height (Z) perturbation in Rossby modes associated with EIS (filled contours) and LCC (contour lines) on synoptic timescales. Maps show Z at 250 hPa. The thick gray solid line marks subtropical jets, and the thick dash line marks polar front jets. The blue contour marks the Sc area. Each row represents one region. 'lag-4' denotes circulation leads EIS/LCC by 4 days. The right column shows the cross-section averaged between latitudes marked by the red ticks on the map. The thick blue and brown underlines of the cross-section represent Sc areas and continents, respectively. (Winter and summer versions in Figures S7–8.)

Vertical velocity perturbations are due to IG modes (Žagar et al., 2023). The vertical velocity patterns in Fig. B.4 are roughly in quadrature with the Rossby modes geopotential height (Figure B.3). The quadrature relationship between Rossby wave geopotential and vertical velocity is consistent with quasi-geostrophic theory; air subsides in the negative vorticity advection region rather than at the center of highs. Neduhal et al. (2024) showed that the quadrature relationship holds for any linear wave solutions. We don't observe other source of vertical velocity perturbations that could originate from tropical convections such as monsoons. This result suggests that the direct effect of monsoon on Sc is negligible compared to that of extratropical Rossby waves, in agreement with the similar arguments by Nigam and Chan (2009) for anticyclones in the subtropics.

The quadrature relationship between Rossby and IG modes remains on all timescales (Figures B.3–B.6). Due to this quadrature relationship, the subsidence perturbations caused by Rossby ridges locate on the east edge of Sc. The compensate ascending motions locate on the west edge (cross-sections in Figure B.4, compare the dipole of color with the blue underline). This setup makes subsidence averaged over the Sc area a poor predictor for EIS variability, which explains EIS appears to be independent from subsidence in the same area (Ding, Stevens, and Schmidt, 2025; Myers and Norris, 2013).

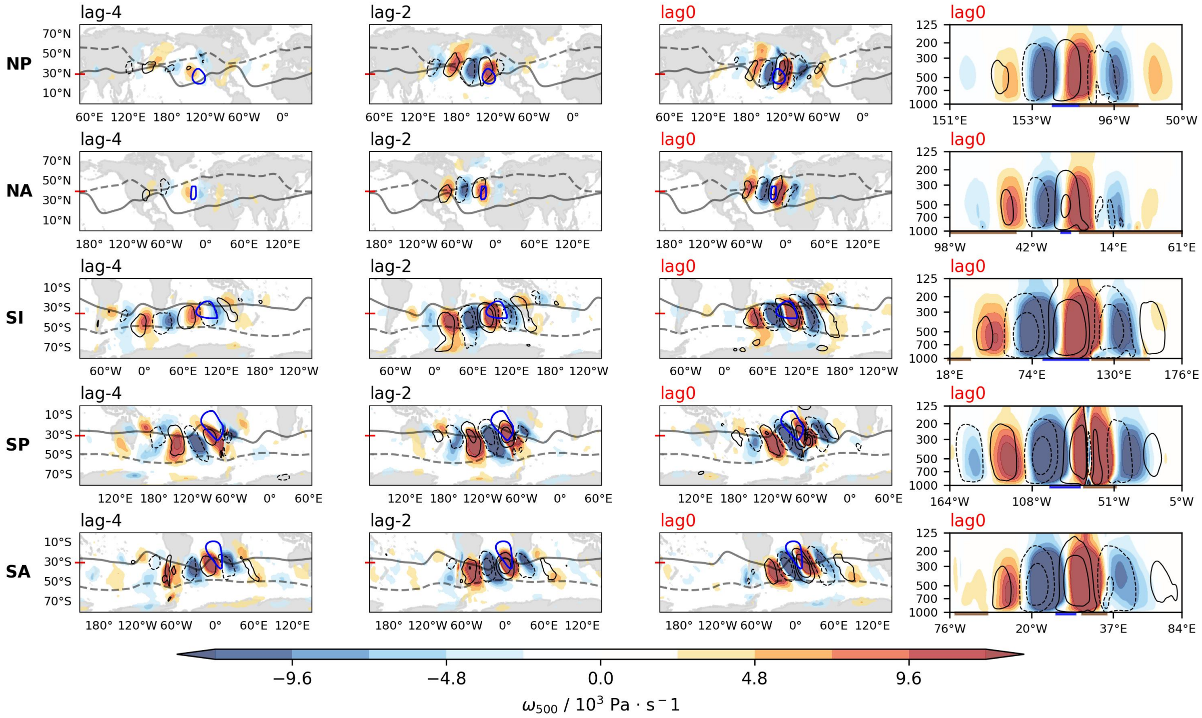

Figure B.4: Vertical velocity (ω) perturbation in IG modes associated with EIS (filled contours) and LCC (contour lines) on synoptic timescales. Maps show ω at 500 hPa. The blue contour marks the Sc area. Each row represents one region. 'lag-4' denotes circulation leads EIS/LCC by 4 days. The right column shows the cross-section along the latitude marked by the red tick on the map. The thick blue and brown lines at the bottom of cross-sections represent Sc areas and continents, respectively. (Winter and summer versions in Figures S9–10.)

B.4.2 *Subseasonal and interseasonal timescales*

Figure B.5 shows circulation controlling subseasonal variability in EIS and LCC (NP as the example). We see a combined pattern of a planetary-scale Rossby wave (around 60°N) and a localized synoptic-scale Rossby wave (around 20°–40°N). The localized synoptic-scale Rossby wave shows similar pattern to that of Figure B.3, and the planetary-scale Rossby wave indicates the stationary wave in mean flow induced by Rocky Mountains (Charney and Eliassen, 1949). This orography-induced planetary-scale wave does not exhibit an obvious oscillation signal (compare lag-30 with lag0).

In contrast, the subseasonal variability of EIS/LCC over the open ocean is associated with an oscillation of the planetary-scale wave on a monthly timescale. This difference further supports the influence of near-field orographic forcing over the Sc area, which allows synoptic-scale Rossby waves to continue controlling Sc variability on subseasonal timescales. Other Sc areas with smaller orography, such as SI, show a similar dependence on the planetary-scale wave as the open ocean does. (Details in Figures S4 and S11.)

The interseasonal results show circumglobal waves extending into the subtropics (with NA as an exception). These waves are not coupled with SST anomalies. It is worth noting that, because we removed the annual cycle, the circumglobal waves represent interseasonal oscillations apart from seasonality. Still, no signal of monsoon-induced perturbations is observed. In comparison,

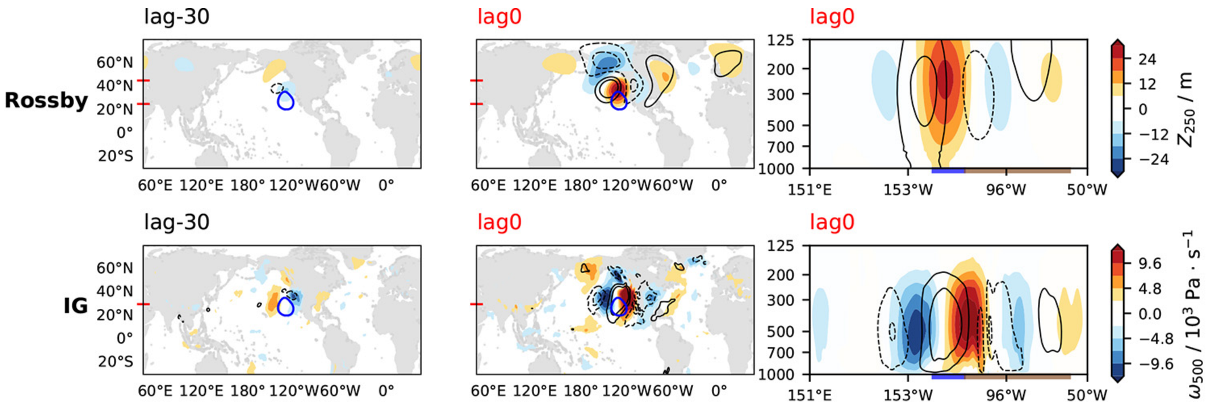

Figure B.5: Geopotential height perturbation in Rossby modes (upper row) and vertical velocity perturbation in IG modes (lower row) associated with NP EIS (filled contours) and LCC (contour lines), respectively, on subseasonal timescales. The other visualization settings are similar to Figures B.3 and B.4. 'lag-30' indicates that the circulation leads EIS/LCC by 30 days. (Rossby modes for all regions are in Figure S10.)

the interseasonal pattern over the open ocean exhibits a monsoon teleconnection when EIS there requires additional subsidence to increase. (Details in Figures S5 and S12.)

B.4.3 *Interannual timescales*

Figure B.6 demonstrates coupling between EIS/LCC variability in NP and global circulation on interannual timescales. The IG-mode tropical pattern is similar to the perturbation in La Niña–like events with ascending (blues in the lower row) around the Maritime Continent and a descending (reds in the lower row) over the central–eastern equatorial Pacific, indicating an enhanced Walker circulation. The compensating upper-level convergence associated with descending branch of this perturbation redistributes absolute vorticity and induces a Rossby wave source in the subtropics (Sardeshmukh and Hoskins, 1988). The induced Rossby-mode circulation in the subtropics is $n = 1$ mode (blues in the upper row) with higher n associated with extratropical signals (patterns at higher latitudes in the upper row). This is a typical pattern associated with stationary response to large-scale tropical heating perturbations.

Apart from tropical heating perturbations, a similar Rossby-mode pattern with a low–high–low meridional structure can also be associated with EIS/LCC variability when its subtropical signal is weak. These results suggest that the upstream high (reds in the black box) has a more robust association with Sc, regardless of whether this structure is induced by extratropical or tropical perturbations, or by a combination of both. This upstream high is coupled with a localized SST pattern in the respective ocean basin: an upstream warm tongue with cooler SST in the Sc area. This coupling is indicated by the Rossby-mode cross-section in Figure B.6. We refer to this atmosphere–ocean coupled pattern as the negative phase of a Pacific Decadal Oscillation–like (-PDO-like) pattern hereafter.

Hence, tropical perturbations are not the direct driver controlling the interannual variability of Sc. Instead, their influence is more likely nonlinear: they can induce a poleward Rossby wave train (first paragraph of §B.4.3) and influence the location of jets (Liu et al., 2021), thereby affecting the propagation of synoptic-scale Rossby waves (discussed in §B.4.1). In comparison, the -PDO-like pattern exerts a more direct influence on Sc (see further discussion in §B.5.3).

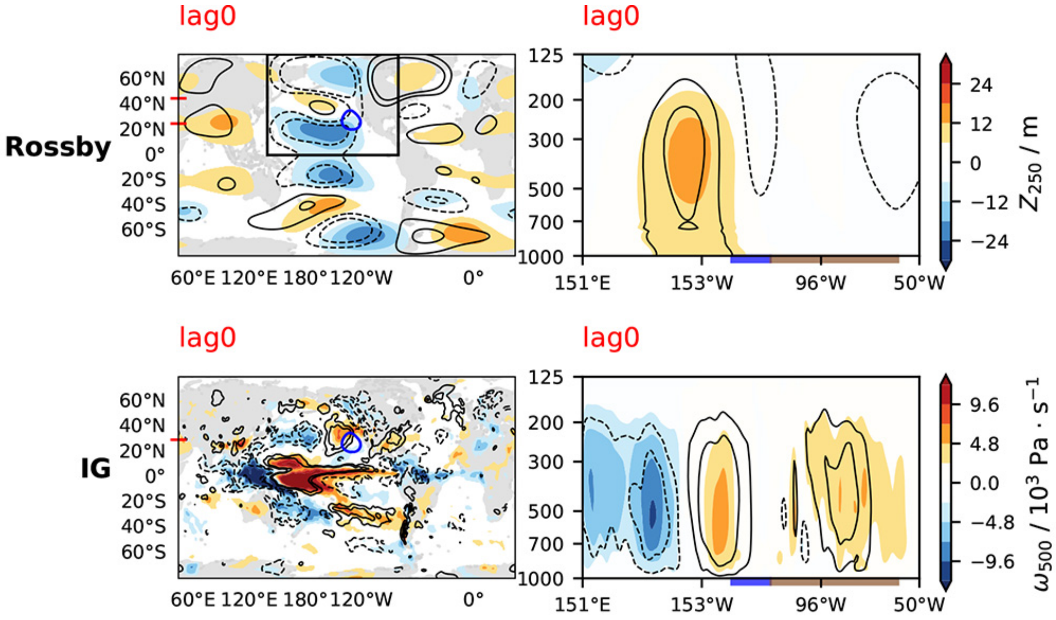

Figure B.6: Geopotential height perturbation in Rossby modes (upper row) and vertical velocity perturbation in IG modes (lower row) associated with NP EIS (filled contours) and LCC (contour lines), respectively, on interannual timescales. The other visualization settings are similar to Figures B.3 and B.4. (Maps for all regions in Figure S14.)

B.5 Composite results for high-EIS and high-LCC cases

In this section, we compare the common and distinct conditions for cases when EIS/LCC exceeds the 90th percentile. We call them the high-EIS and high-LCC cases, respectively.

B.5.1 *Synoptic evolution*

Figure B.7 shows the evolution for high-EIS cases from six days prior (lag-6) to the reference day (lag0). When a Rossby ridge approaching Sc, the geopotential height anomaly keeps increasing there, and so does the θ_{700} (panels a and b). SST doesn't change much, supporting that Ekman pumping in the ocean has little influence on EIS. Meanwhile, θ_{1000} cools more than SST, indicating that the cooling is mainly due to the boundary-layer processes in the atmosphere.

Cross-sections in Figure B.7 show geopotential height anomalies (Z', filled counters) under the synoptic-scale Rossby wave perturbation. The blue underline indicates the Sc area and the brown underlines indicate lands. The right brown underline in panels c–f represents North America. Arrows denote wave activity fluxes, which indicate the direction of energy propagation independent of wave phase (Takaya and Nakamura, 2001). We observe that wave energy mainly propagates from west to east. The propagation is stronger upstream of the Rocky Mountains. We observe wave activity convergence around the Sc area, as the eastward wave activity fluxes upstream meet the westward ones above the Rocky Mountains (arrows in panels c–f). This convergence is associated with an amplified high-pressure anomaly in the Sc area, which is similar to the orographic phase-locked amplification effect observed in Jiménez-Esteve, Kornhuber, and Domeisen (2022). Jiménez-Esteve, Kornhuber, and Domeisen (2022) show this amplification effect preferentially acts on k =5–6 waves, which are the dominant waves for Sc on the synoptic timescales (panels a–c of Figure B.2).

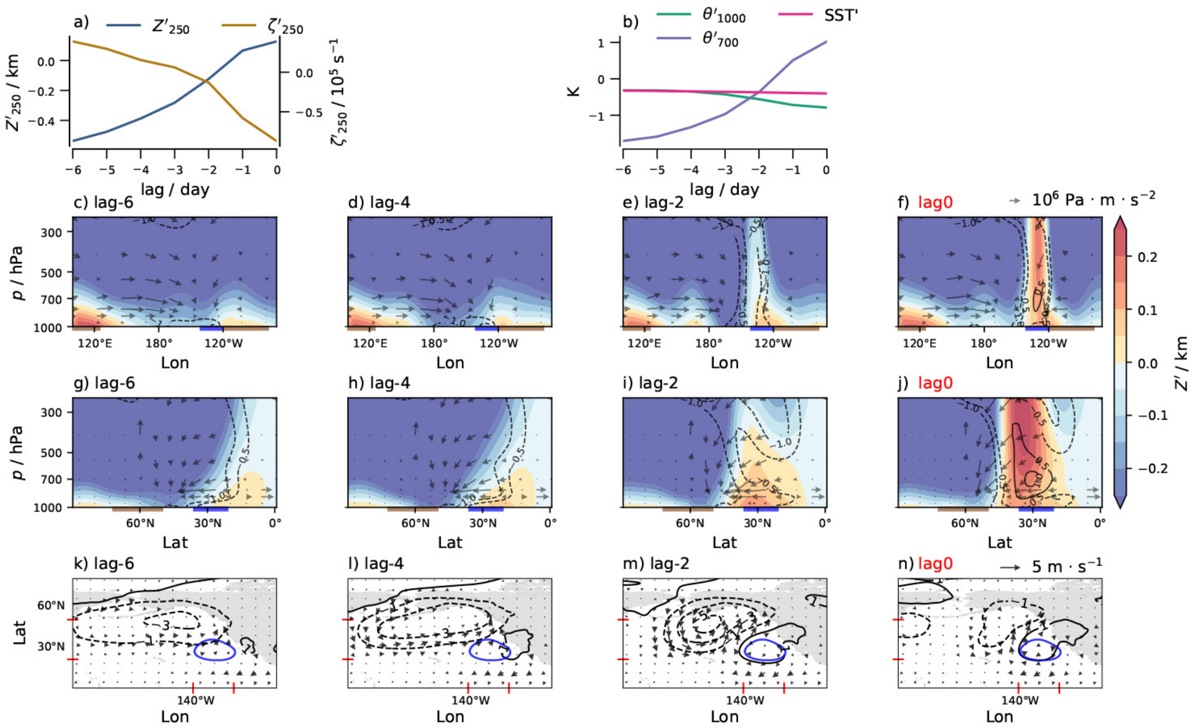

Figure B.7: Synoptic evolution from lag-6 to lag0 days for composite high-EIS cases in NP. a) 250 hPa geopotential height (Z) and relative vorticity (ζ) anomaly. b) potential temperature (θ) and SST anomaly. Prime denotes anomaly. a–b) show values averaged over the Sc area (blue contour in k–n). c–f) zonal and g–j) meridional cross-sections of Z' (filled contours), θ' (contour lines, only visualize -1, -0.5, 0.5, and 1), and wave activity flux (arrows, the vertical direction is multiplied by 10^6 for visualization). The averaged latitude/longitude range used for the zonal/meridional cross-sections are marked by the red ticks in k–n. k–n) sea level pressure anomaly (unit:hPa, contour lines) and 1000 hPa winds anomaly (wind vectors).

On day 0, Z' shows a two-maxima structure: one near the surface and the other in the upper troposphere. Performing a similar analysis away from orography shows that the maximum in the upper troposphere vanishes, and thus the amplified high anomalies is speculated to due to the near-field orographic effects. The amplified high anomalies continuously warm θ_{700} for several days as a synoptic-scale Rossby ridge passes by (see panel b).

The two-maxima structure of Z' is associated with a positive θ' between 500 hPa and 850 hPa, as well as a negative θ' within the boundary-layer (panel f and j). This distribution of Z' and θ' fits the hypsometric equation. θ' centered at the level of the largest gradient of Z'. However, the mechanism for the boundary-layer cooling is not that clear. We speculate this is due to the near-surface cold advection under the anticyclonic perturbation. The near-surface cold advection can create a cold-high anomaly in the boundary-layer, while the upper-level anticyclone warms the free troposphere. We don't know how much contribution of the surface latent heat flux and radiative cooling of clouds. Hotz, Papritz, and Röthlisberger (2024) studies the 3D Lagrangian trajectory of the anticyclone over land, and they found the boundary-layer has a different thermal response to anticyclone compared to the free troposphere. Thus, we refer to the low-level baroclinic change of θ as the column response under synoptic-scale Rossby ridge perturbation. EIS is increased by this column response.

Panels k–n in Figure B.7 show the evolution of SLP and 1000 hPa winds. A positive SLP anomaly locates over the Sc area on day 0, with winds circulating around it. This localized SLP anomaly is located downstream of subtropical highs, indicating that a localized increase in pressure is not necessarily caused by a strengthening of the subtropical highs, but instead results from the enhancement associated with a passing synoptic-scale Rossby ridge. This explains why EIS decorrelates from the strength of the subtropical highs (Ding, Stevens, and Schmidt, 2025).

B.5.2 *Different responses of LCC and EIS to large-scale circulation*

Here we discuss why LCC prefers a Rossby ridge that shifts about 10° upstream.

Figure B.8 shows a similar mechanism to the high-EIS cases in Figure B.7. However, LCC prefers a SLP anomaly that is centered upstream (panel f). This upstream SLP anomaly is aligned with the position of subtropical highs, explaining why studies observed the association between enhanced subtropical highs and larger LCC (George and Wood, 2010; Klein, 1997; Toniazzo et al., 2011). Averaging factors over a 10° upstream area (the blue box in Figure B.8), the geopotential anomaly peaks about one day prior, consistent with Klein, Hartmann, and Norris (1995). This upstream high enhances the pressure gradient between upstream and the Sc area. The enhanced pressure gradient strengthens the near-surface winds along the Lagrangian trajectory of Sc.

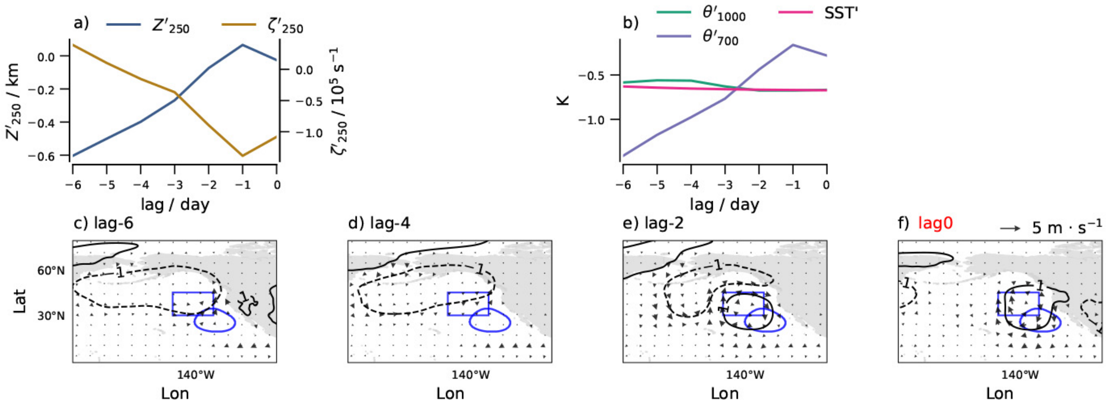

Figure B.8: Similar to the 1st and 4th rows of Figure B.7 but for composite high-LCC cases. a–b) show values averaged over the blue box in c–f) which is 10° west and poleward of the Sc area (blue contour).

Stronger near-surface winds can increase both near-surface cold advection ($-T_{\mathrm{adv}}$) and evaporation (represented by negative latent heat flux, -LHF). Figure B.9 compares them between high-EIS and high-LCC cases. It shows that during the evolution of high-LCC cases (solid lines), cold advection is stronger (with approximately 40% larger range) and negative latent heat flux is larger (by approximately 80%) compared to high-EIS cases (dash lines). Cold advection can enhance mixing in the marine boundary-layer and increase Sc (Klein, Hartmann, and Norris, 1995; Scott et al., 2020; Wood and Bretherton, 2004). Negative latent heat flux (i.e., evaporation) can serve more moisture. In the 3rd panel, we see how this moisture supply cancels the drying effect of the Rossby ridge coming from the west poleward. This canceling effect is more significant in the middle of the boundary-layer (e.g., 950 hPa). We don't observe a significant canceling effect at the 1000 hPa or 700 hPa level. Thus, taking into account moisture would be helpful to predict LCC, but which level to select may also influence how much it improves compared to solely considering EIS.

To notify, Bretherton and Wyant (1997) suggest that LHF change can lead to a boundary-layer decoupling, which points to less well-mixing. This effect may be in competition with the enhanced mixing from cold advection in some circumstances.

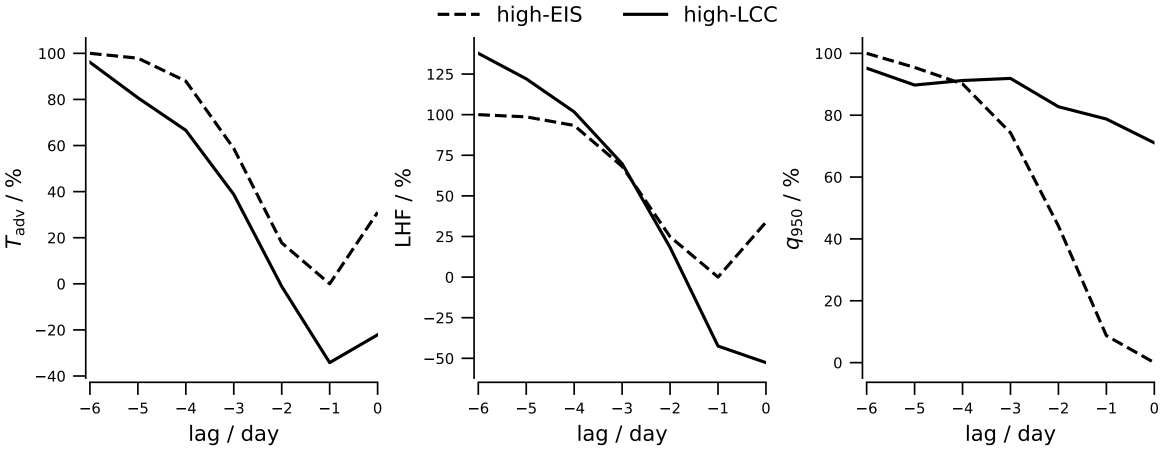

Figure B.9: Synoptic evolution of surface temperature advection (T_{adv}, left), surface latent heat flux (LHF, middle), 950 hPa specific humidity (q_{950}, right) in NP composite high-EIS and high-LCC cases. Values are averaged over the Sc area and are normalized by the range of high-EIS cases. Negative values of T_{adv} indicate cold advection, while negative values of LHF indicate an upward surface flux (i.e., evaporation), and vice versa.

Therefore, apart from the increased local stability, LCC can also directly respond to the upstream Rossby ridge through boundary-layer processes. As deseasonalization has been applied before conducting the composite analyses, the results reflect synoptic perturbations that can occur throughout the year. Table B.2 shows that LCC increasing does not rely on EIS increasing. EIS prefers winter circulation, when jets are stronger and synoptic-scale Rossby waves are more active. Meanwhile, LCC shows less seasonal preference, as both the dynamical processes in winter and the larger evaporation in summer (due to warmer SST) favor more LCC.

Table B.2: Seasonal occurrence (in %) of high-EIS and high-LCC cases on synoptic timescales. Values show the fraction of cases occurring in DJF and JJA relative to the total number of cases.

	high-EIS		high-LCC	
	DJF	JJA	DJF	JJA
NP	34	11	32	12
NA	28	17	25	20
SI	13	33	18	28
SP	17	36	24	26
SA	9	40	20	27

B.5.3 *The role of SST on interseasonal and interannual timescales*

Unlike the short timescales, when EIS increases due to the column response of the synoptic-scale atmospheric Rossby ridge, the long-term variability of EIS is also influenced by SST.

Although EIS and LCC correlate strongly on long timescales, Figure B.10 suggests that it might be due to some shared influence by low-frequency circulations. Comparing the interseasonal patterns (panels b and d), LCC prefers upstream SST warming, while EIS prefers local SST cooling, once the annual cycle is removed. The upstream warming associated with LCC is consistent with **Szoeke_et_al2016**. In addition, the discrepancy between LCC and EIS identified on synoptic timescales (i.e., stronger pressure gradients for LCC versus more localized high-pressure anomalies for EIS) remains on interseasonal timescales.

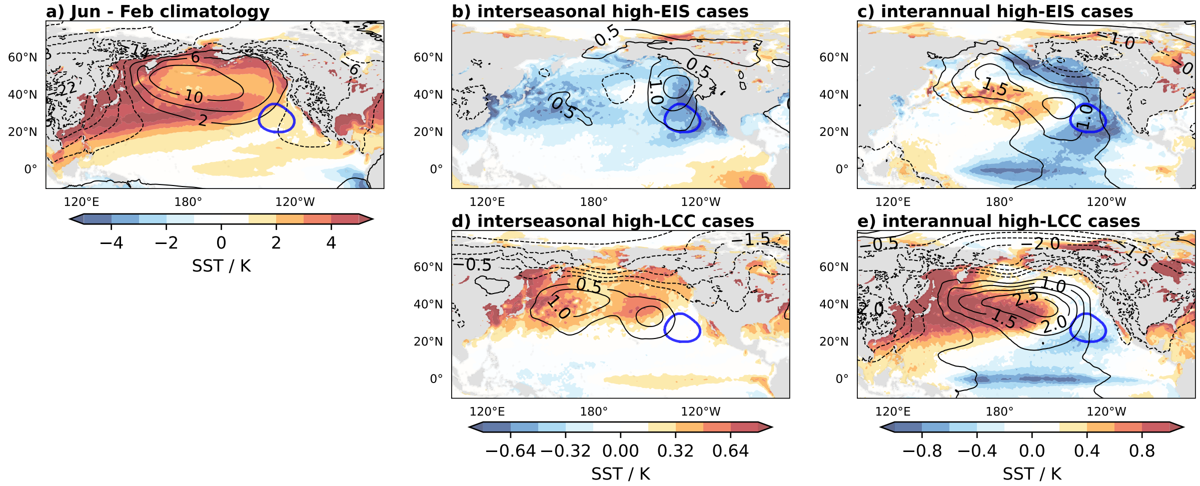

Figure B.10: Maps of SST (filled contours) and SLP (contour lines): a) difference between June and February in the climatology; b) anomalies from the climatological mean in the interseasonal high-EIS cases; c) anomalies from the climatological mean in the interannual high-EIS cases; d–e) are similar as b–c) but for the high-LCC cases. (Panels b and d for all regions in Figure S13; panels c and e in Figure S14.)

That discrepancy can be hidden well if including the annual cycle. Figure B.10a shows the circulation change from winter to summer. We see that SST shows a -PDO-like pattern, which has a warm tongue upstream with relative cool in the Sc area. This relative cool, together with higher atmospheric pressure in summer, increases EIS. Meanwhile, the upstream warm tongue, coupled with higher pressure upstream, favor more LCC. Therefore, EIS and LCC can both increase through different reasons. The strong correlation (usually >0.8) between EIS and LCC on the annual cycle may be confounded by this set of circulation change.

Similar reason leading to high correlation between EIS and LCC on interannual timescales (panels c and e). On interannual timescales, atmospheric circulation coupled with SST pattern. Negative phase of PDO-like structures co-control EIS and LCC, while the preference of regions still shows. The coupling between this -PDO-like pattern and LCC is also observed in model simulations (Bellomo et al., 2014).

B.6 Conclusions and discussion

This study establishes the relationships between large-scale circulation and stratocumulus (Sc), and finds that low-cloud cover (LCC) and estimated inversion strength (EIS) respond differently to circulation perturbations.

Instead of the tropical thermodynamic framework, we find an extratropical dynamics control EIS variability. On synoptic and subseasonal timescales, local synoptic-scale Rossby ridges enhance EIS by increasing the stability of the tropospheric column. Due to near-field orography (e.g., the Rocky Mountains, the Andes, and the South African Plateau), these synoptic-scale Rossby ridges can be amplified around Sc areas. This amplification makes synoptic-scale Rossby ridges pronounce on longer timescales, especially in NP, SP, and SA with significant orography. On interseasonal timescales, both atmospheric Rossby ridges and local SSTs influence EIS variability. On interannual timescales, EIS variability is associated with the negative phase of a PDO-like (−PDO-like) pattern, in which the atmosphere and ocean circulation are coupled. The −PDO-like pattern features extratropical planetary-scale Rossby ridges in the atmosphere and cooler SSTs in the Sc area, both of which can increase EIS. About 76% of EIS variability is explained by the above circulation perturbations, quantified using local 250,hPa geopotential height, 250,hPa vorticity, and SST from 33-year daily series (details of the quantification method are provided in the Supplement, last page).

EIS and LCC exhibit different dependence on similar circulation patterns. Compared with EIS, LCC shows larger dependence on upstream perturbations. Specifically, LCC is associated with upstream Rossby ridges (about a 10° shifted pattern) and upstream SST warming. The reason for this upstream preference is that LCC prefers stronger near-surface winds, which can result from larger pressure gradients. Stronger near-surface winds in the Sc area enhance cold advection and destabilize the marine boundary-layer, thereby enhancing turbulent mixing and favoring more Sc (Klein, Hartmann, and Norris, 1995). Meanwhile, stronger near-surface winds also lead to larger evaporation, which can offset a major part of the drying effect associated with Rossby ridges. Upstream SST warming also supports the enhancement of these boundary-layer processes. Therefore, although EIS tends to prefer winter conditions after deseasonalization, as synoptic-scale Rossby waves are more active in winter, LCC show little seasonal dependence as summer conditions supply more moisture. Solely using EIS explains about 34% of LCC variability, while solely using upstream circulation (quantified using the same method as for EIS variability, but with the averaging region shifted 10° upstream) explains about 36% of LCC variability. Using EIS and upstream circulation together increases the explained variance to 45%, indicating that upstream circulation can direct influence LCC apart from varying EIS. This finding is consistent with Lewis, Bellon, and Dinh (2023) and Lewis and Bellon (2025), although they interpret the upstream preference as a lagged response to upstream EIS.

The different circulation dependence of EIS and LCC suggests that their strong correlation on long timescales is confounded by the −PDO-like circulation structure, which has cooler local SSTs and warmer upstream SSTs that favor both EIS and LCC. We suggest that future studies consider the influence of this pattern when investigating long-term changes in Sc.

The 10° upstream-shifted pattern associated with LCC variability explains why Sc responds to conditions from one day earlier (Klein, Hartmann, and Norris, 1995), as this distance corresponds to about one day of advection at a typical near-surface wind speed in these regions. Therefore, the "one-day-lagged covariance" likely reflects the influence of enhanced near-surface winds on LCC, which are more strongly perturbed by synoptic-scale Rossby waves than by long-term variability in the zonal-mean flow.

Supplements

See next page.

Data availability

Both ERA5 (Hersbach et al., 2017b) and CLARA-A3 dataset (Karlsson et al., 2022) are available at Climate Data Store (`https://cds.climate.copernicus.eu/datasets`). MODES (Žagar et al., 2015) is available at `https://modes.cen.uni-hamburg.de/software`.

Author contributions

HD designed and conducted the analyses and wrote the manuscript. BS initiated the research objects and reviewed the manuscript. FL provided systematic input on the analyses and reviewed the manuscript. NŽ initiated and provided support on methodology and reviewed the manuscript. NŽ, BS, and FL contributed suggestions for interpretation.

Competing interests

The authors declare that no competing interests are present.

Acknowledgments

We thank Hauke Schmidt for testing ideas and interpretations. We thank Bernat Jiménez-Esteve for sharing thoughts on the orographic effects. We thank Volkmar Wirth and Tim Woollings for sharing thoughts on the influence of jets. We thank Katharina Holube, Sergiy Vasylkevych, Franziska Glassmeier, Helene Marie Glöckner for their inputs, and Peishan Chen for sharing her experience with the wave decomposition. We thank Divya Sri Praturi for doing internal review. We thank the dataset and supercomputer resources provided by DKRZ (Deutsches Klimarechenzentrum), as well as the Marin cluster supported by CEN-IT (IT services of the Center for Earth System Research and Sustainability) at Universität Hamburg.

Supplement for paper Large-scale circulation and stratocumulus variability

1 Coherence for each stratocumulus (Sc) region

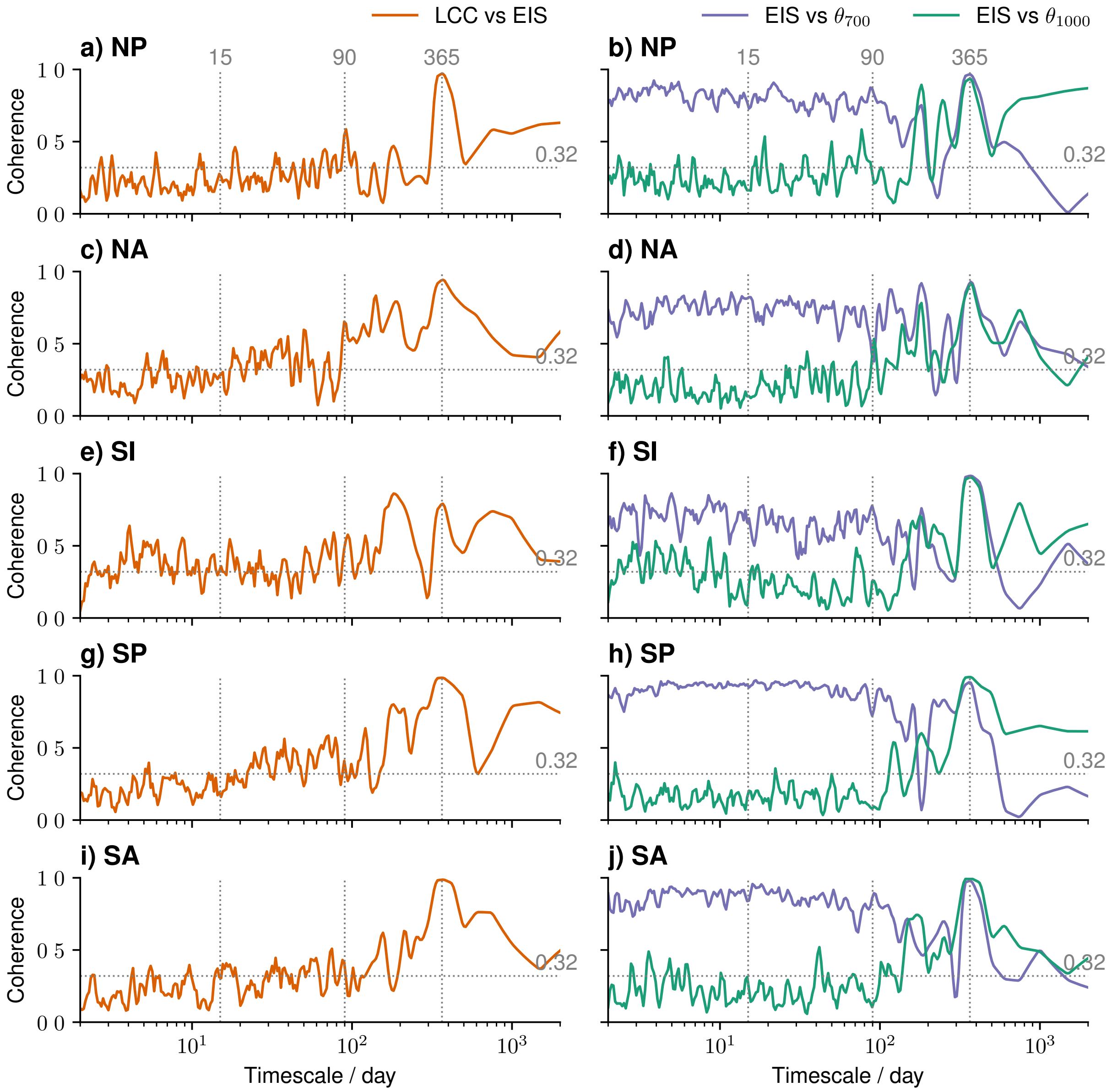

Figure S1: Left: coherence of LCC versus EIS across timescales. Right: coherence of EIS versus $\theta_{700}/\theta_{1000}$ across timescales. NP: North Pacific Sc area. NA: North Atlantic Sc area. SI: South Indian Ocean Sc area. NP: South Pacific Sc area. SA: South Atlantic Sc area.

2 Deseasonalized LCC variance across Timescales from fast Fourier transform

Table S1: Variance of LCC on each timescales after deseasonalization (derived from the fast Fourier transform).

	$\sigma^2_{\text{synoptic}}$	$\sigma^2_{\text{subseasonal}}$	$\sigma^2_{\text{interseasonal}}$	$\sigma^2_{\text{interannual}}$
North Pacific (NP)	136	137	34	24
North Atlantic (NA)	204	187	51	19
South Indian Ocean (SI)	130	86	21	16
South Pacific (SP)	46	48	14	12
South Atlantic (SA)	65	60	13	13

3 Dominant wavenumbers for EIS variability

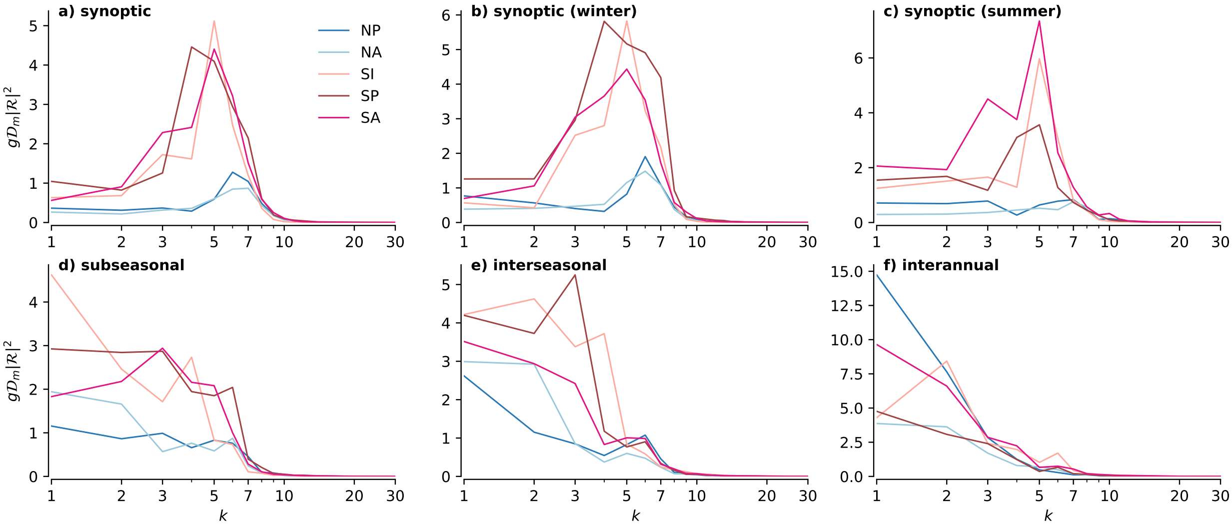

Figure S2: Variance ($g\mathcal{D}_m|\mathcal{R}|^2$) of Rossby modes coupled with EIS as a function of zonal wavenumber (k). Each color represents a region, g denotes gravity, and $\mathcal{D}_m$ denotes equivalent depth on the vertical dimension.

4 Regression results for an open-ocean area in North Pacific

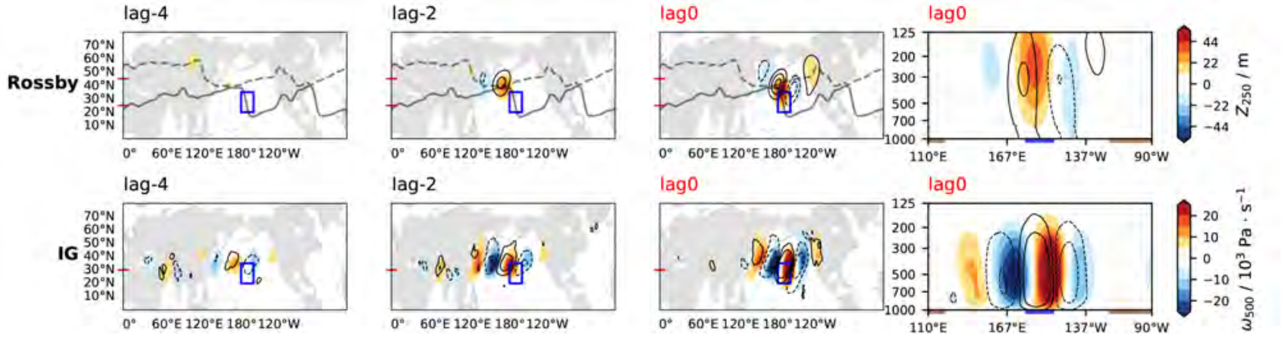

Figure S3: Synoptic timescales plots. Visualization settings are similar to Figures 3 and 4 in the paper but for regressions in an open-ocean area marked by the blue box.

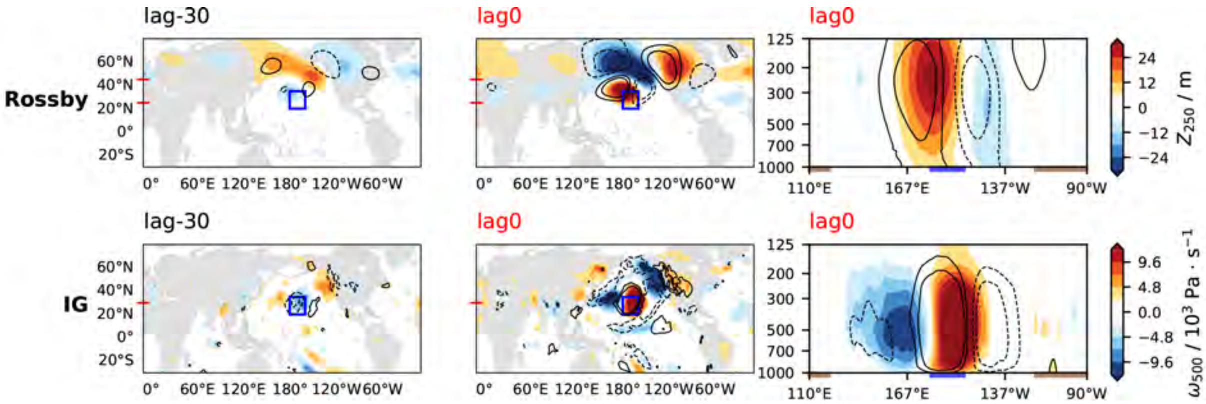

Figure S4: Subseasonal timescales plots for the open-ocean area (blue box).

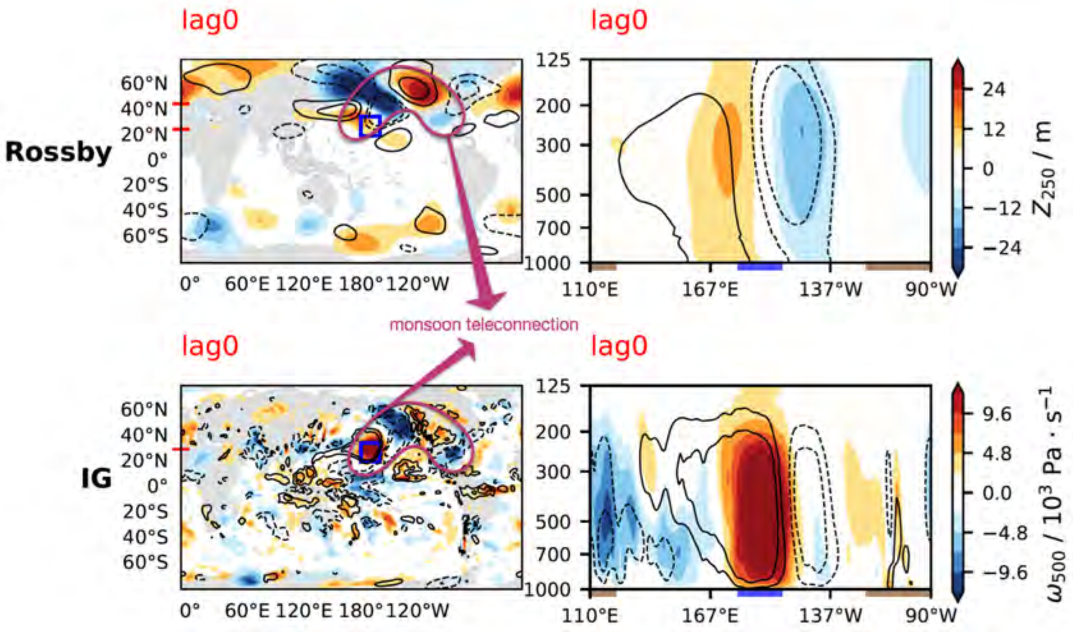

Figure S5: Interseasonal timescales plots for the open-ocean area (blue box).

5 Composite results for an open-ocean area in North Pacific

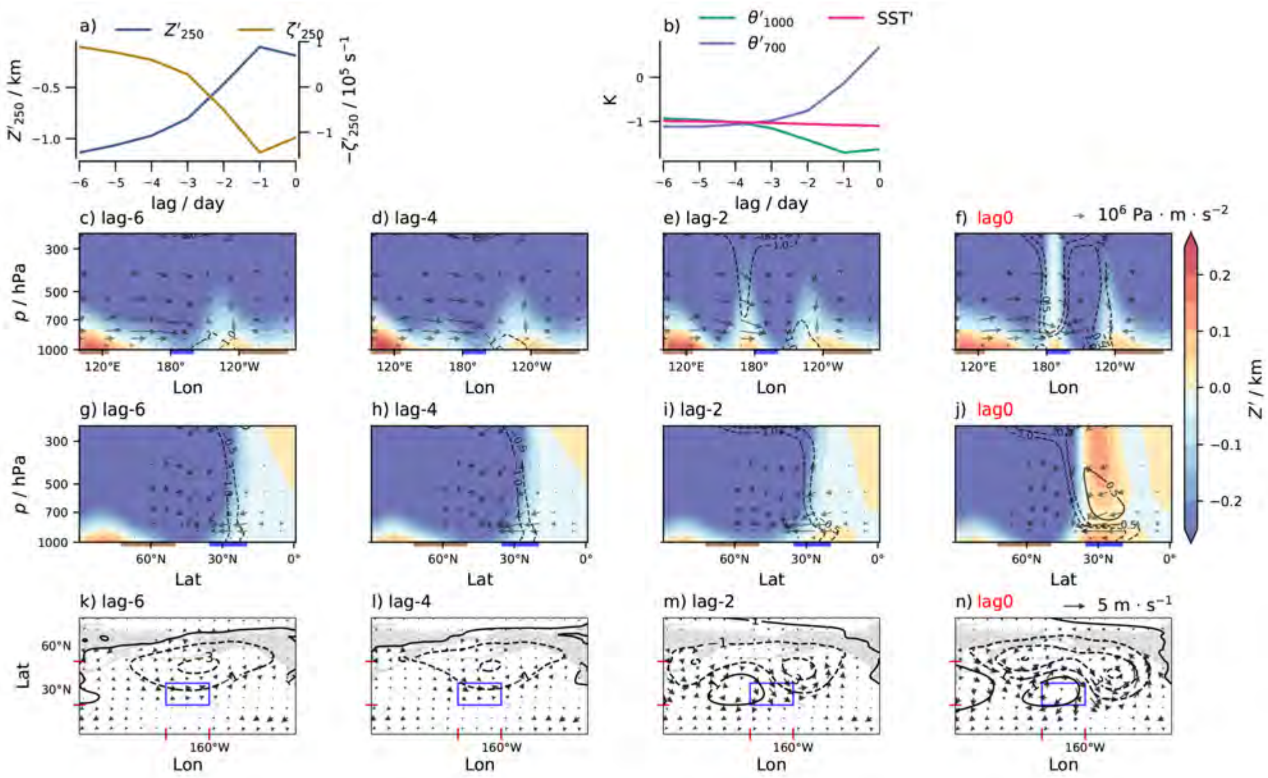

Figure S6: Similar to Figure 8 in the paper but for the open-ocean area.

6 Winter and summer patterns on synoptic timescales

Rossby modes:

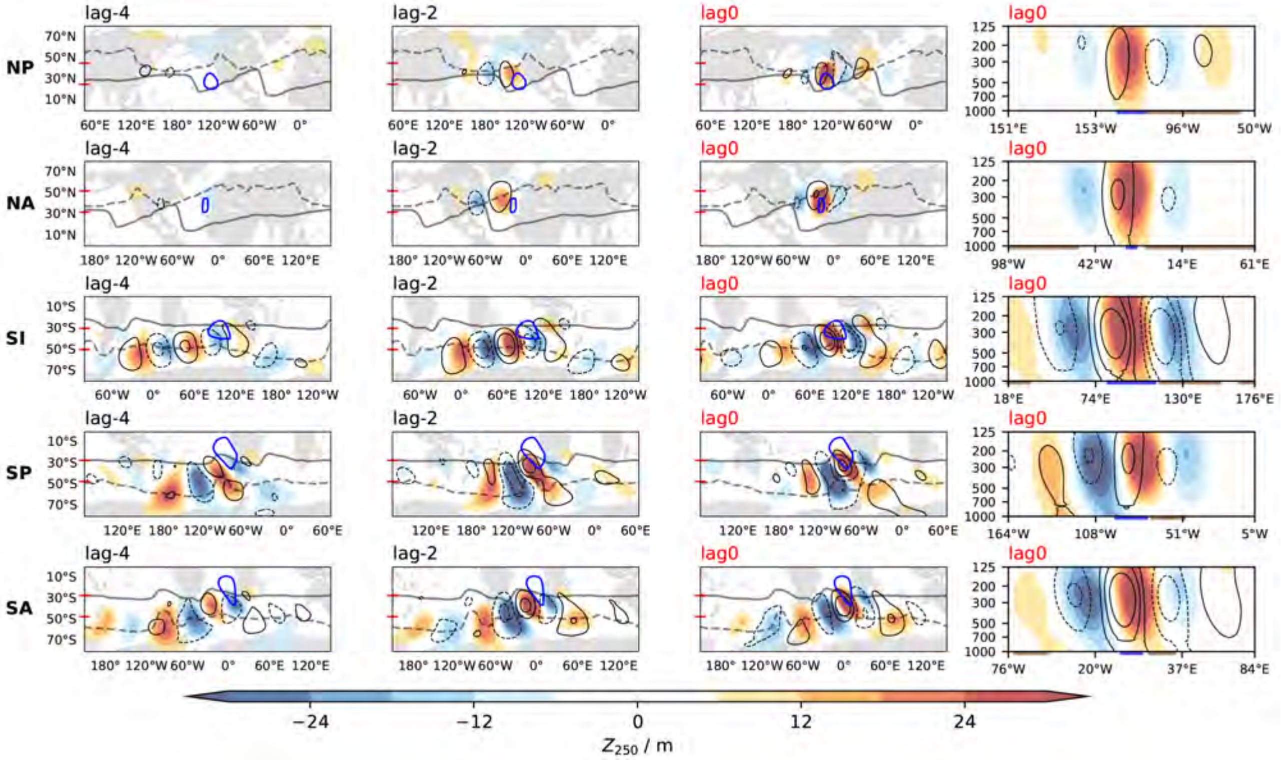

Figure S7: Winter (DJF for the Northern hemisphere and JJA for the Southern hemisphere) version of Figure 3 in the paper.

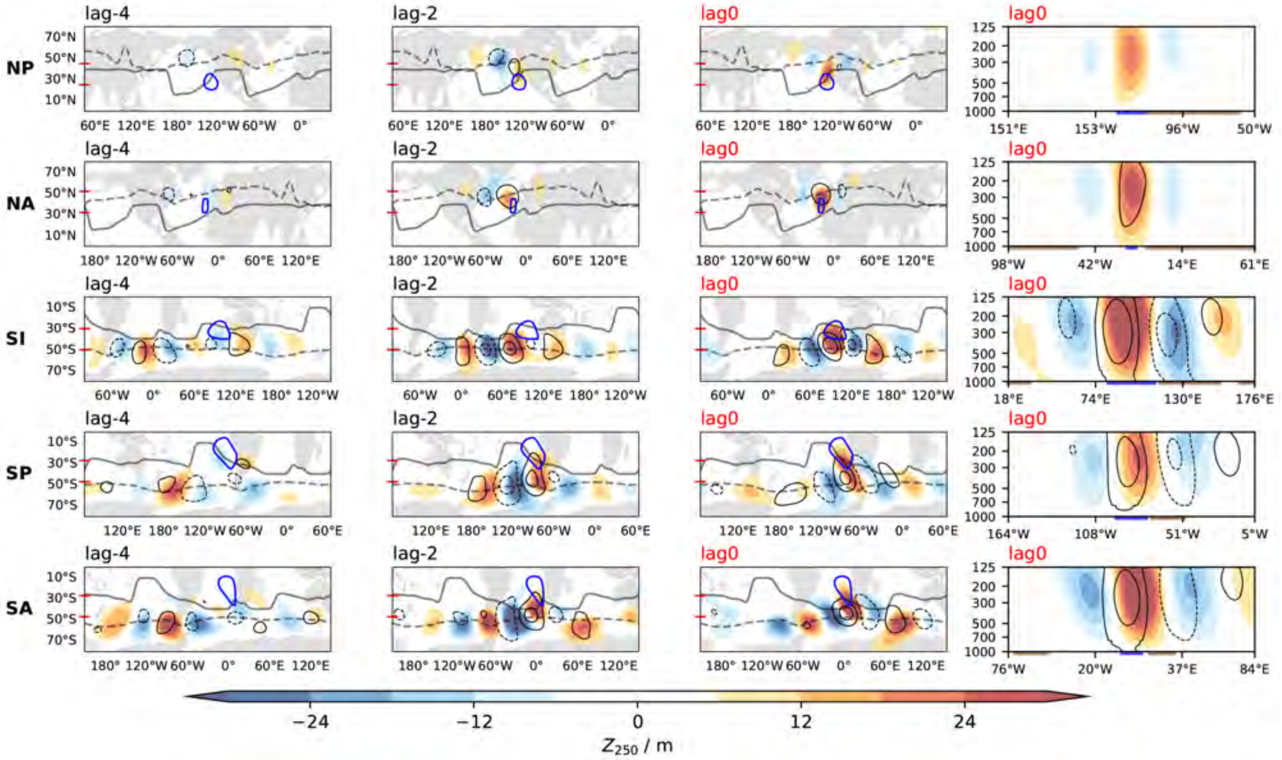

Figure S8: Summer (JJA for the Northern hemisphere and DJF for the Southern hemisphere) version of Figure 3 in the paper.

IG modes:

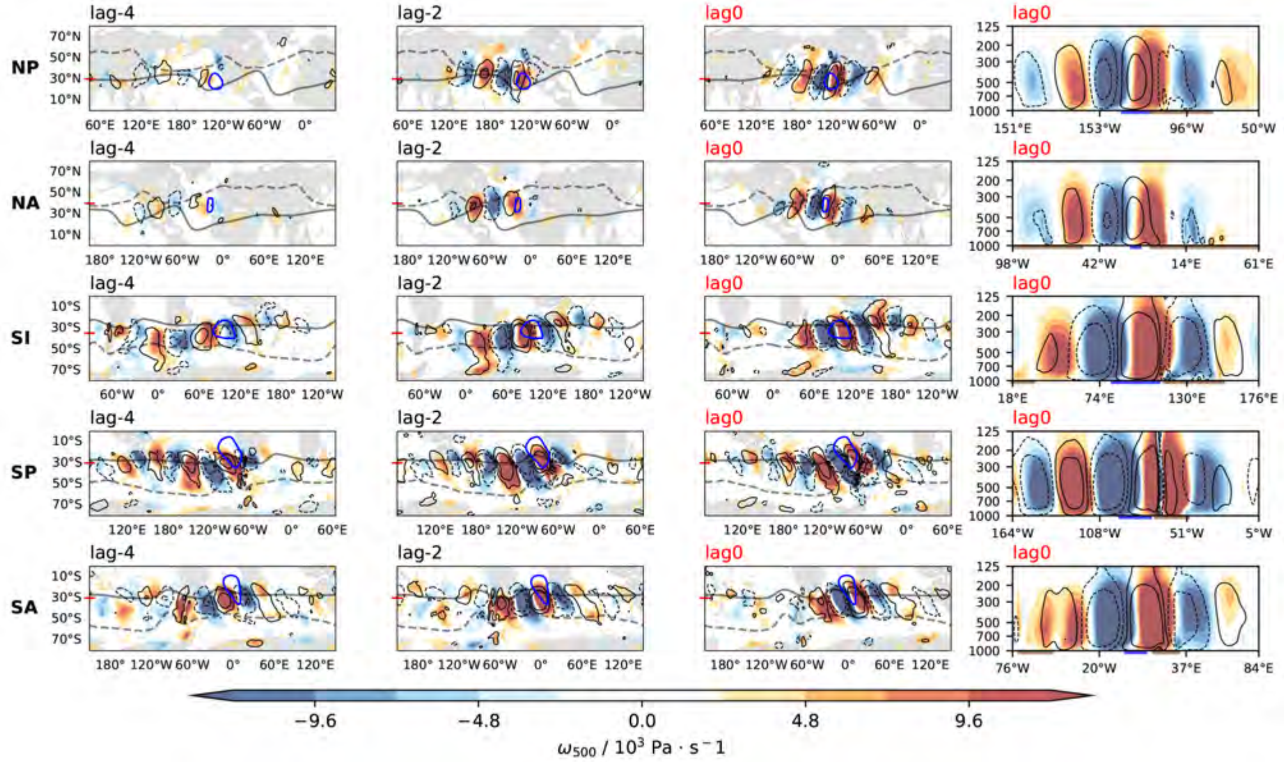

Figure S9: Winter version (DJF for the Northern hemisphere and JJA for the Southern hemisphere) of Figure 4 in the paper.

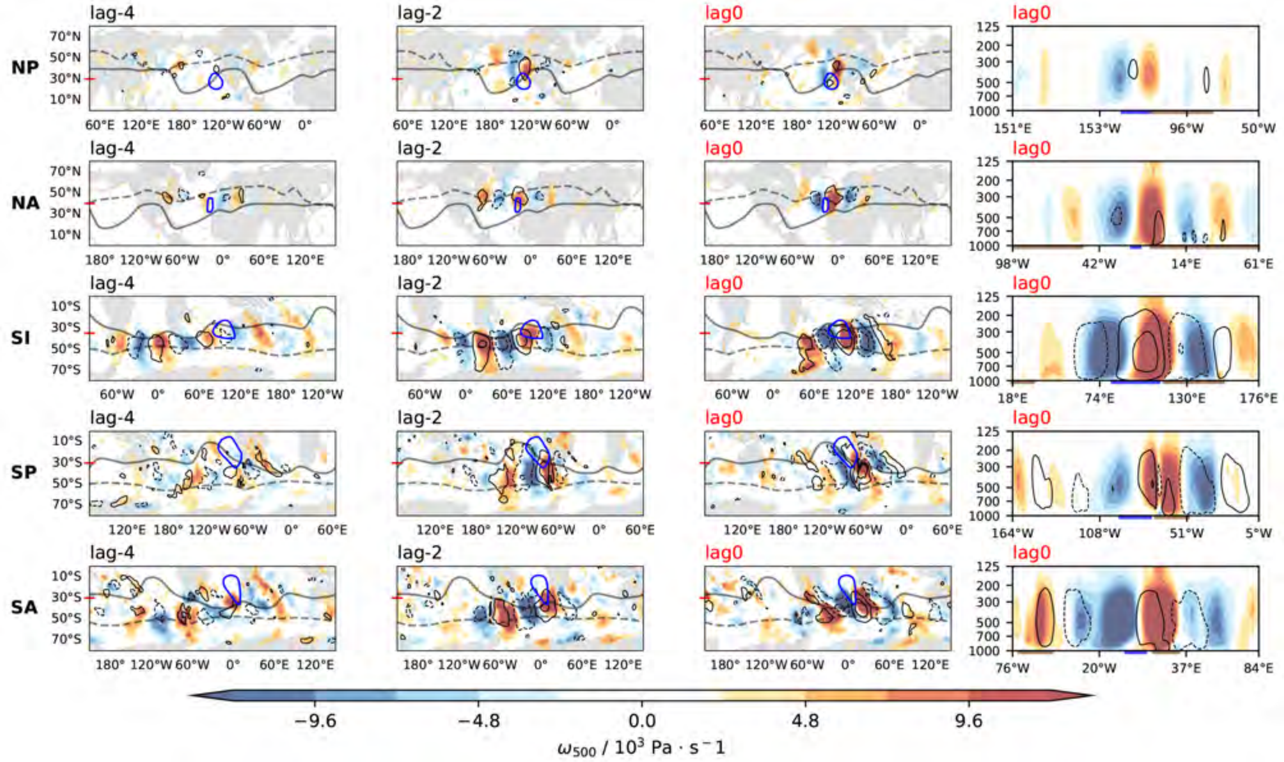

Figure S10: Summer (JJA for the Northern hemisphere and DJF for the Southern hemisphere) version of Figure 4 in the paper.

7 Subseasonal Rossby modes for all regions

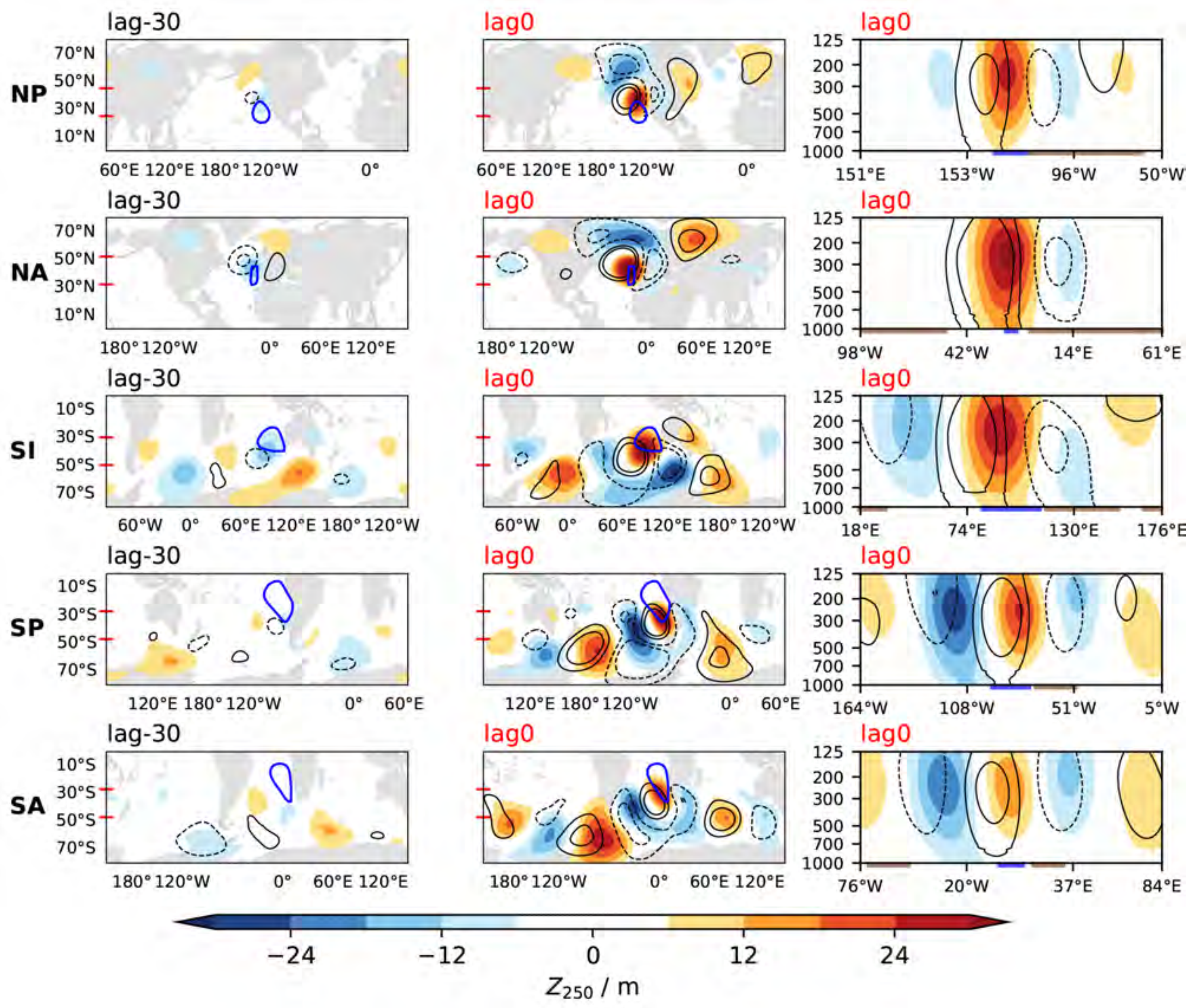

Figure S11: Similar to Figure 5 in the paper but only show Rossby modes for all regions.

8 Interseasonal patterns for all regions

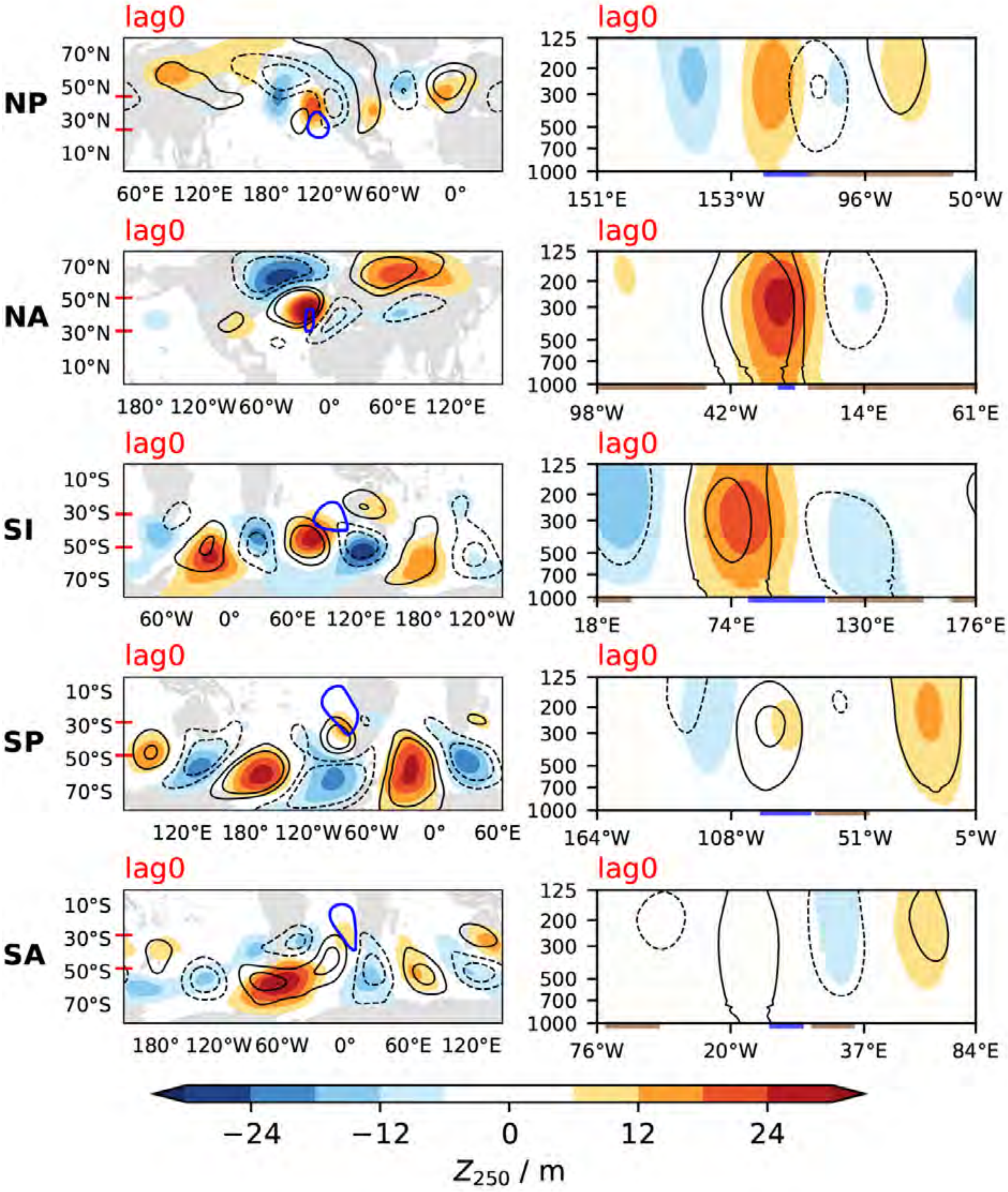

Figure S12: Similar to Figure 5 in the paper but on interseasonal timescales, and only show Rossby modes for all regions.

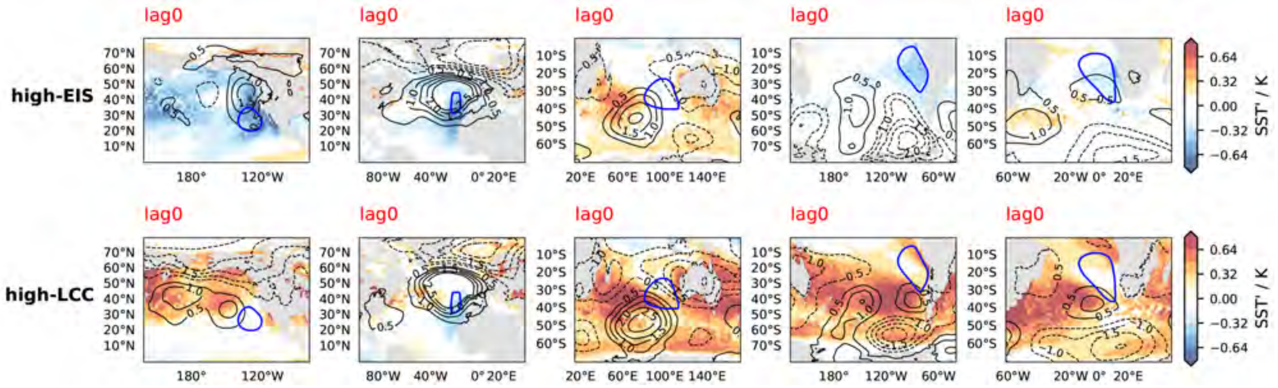

Figure S13: Interseasonal plots for composite high-EIS cases SST and SLP (1st row), and composite high-LCC cases SST and SLP (2nd row). Each column represents one region. The blue thick contour represents Sc areas.

9 Interannual patterns for all regions

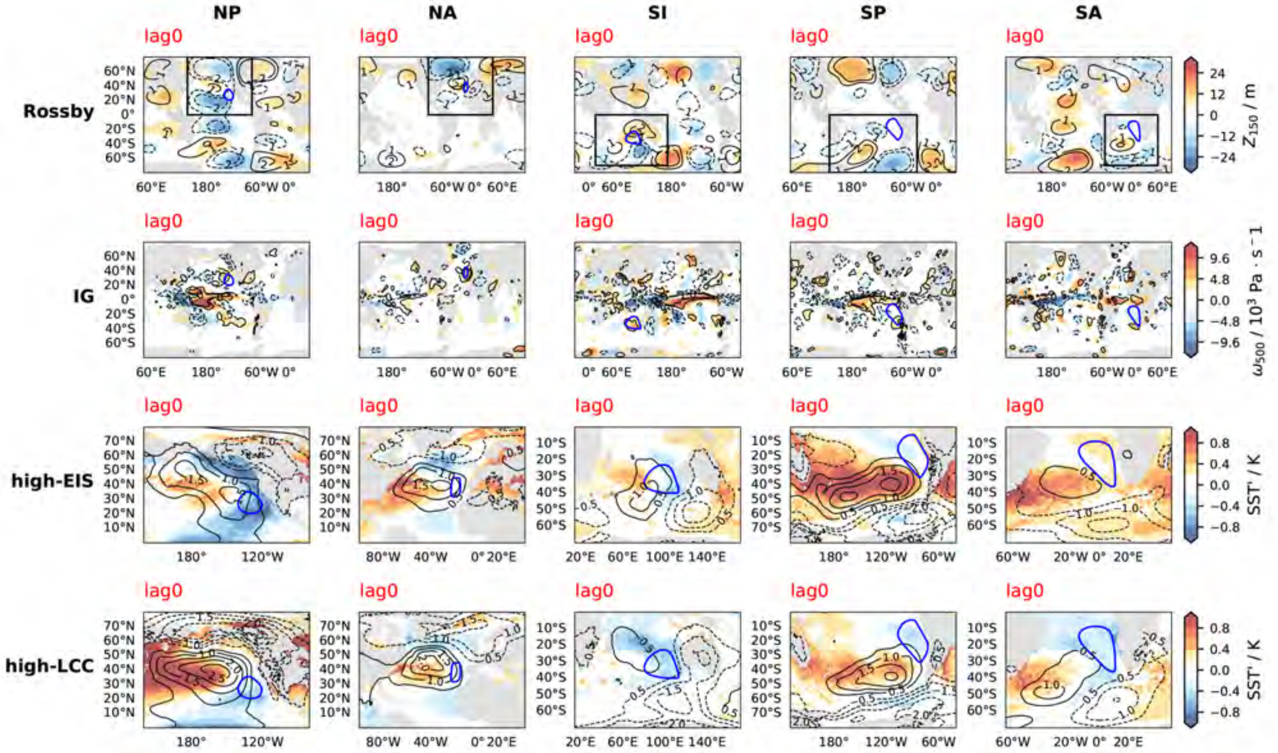

Figure S14: Interannual plots for Rossby modes (1st row), IG modes (2nd row), composite high-EIS cases SST and T_{700} (3rd row), and composite high-LCC cases SST and T_{700} (4th row). Each column represents one region. The black box in the 1st row highlights the plotting domain of the 3rd and 4th rows. The blue thick contour represents Sc areas.

10 The explained variability by extratropical Rossby waves and SST

We quantify the explained variance by the factor of determination R^2 using multi-linear regressions.

- $R^2_{\mathrm{LCC,ucir}}$ (LCC explained by upstream circulation): $\mathrm{LCC} = \alpha + \beta_1 \zeta_{250u} + \beta_2 Z_{250u} + \beta_3 \mathrm{SST_u} + \varepsilon$;
- $R^2_{\mathrm{EIS,cir}}$ (EIS explained by local circulation): $\mathrm{EIS} = \alpha + \beta_1 \zeta_{250} + \beta_2 Z_{250} + \beta_3 \mathrm{SST} + \varepsilon$;
- $R^2_{\mathrm{LCC,EIS}}$ (LCC explained by local EIS): $\mathrm{LCC} = \alpha + \beta_1 \mathrm{EIS} + \varepsilon$;
- $R^2_{\mathrm{LCC,EIS+ucir}}$ (LCC explained by local EIS and upstream circulation): $\mathrm{LCC} = \alpha + \beta_1 \zeta_{250u} + \beta_2 Z_{250u} + \beta_3 \mathrm{SST_u} + \beta_4 \mathrm{EIS} + \varepsilon$.

where 'u' represents for upstream (box that 10° west and poleward of the respective Sc area), α is the intercept, β_i is the slope coefficient, ζ_{250} is 250 hPa relative vorticity, Z_{250} is 250 hPa geopotential height, and ε is the residual. All factors were standardized by their means and standard deviations before doing regressions.

$$R^2 = 1 - \frac{\mathrm{var}(\varepsilon)}{\mathrm{var}(\mathcal{I})}, \tag{1}$$

where var denotes temporal variance and $\mathcal{I}$ represents the index like LCC or EIS.

Then we adjust R^2 to ensure the comparability among different sets by

$$R^2 = 1 - (1 - R^2)\frac{N-1}{N-p-1}, \tag{2}$$

where N is the length of time series and p is the number of predictors in the multi-linear regression equation.

Results:

Table S2: Coefficients of determination (R^2 / %) from multi-linear regressions. 'orig' denotes the original daily series; 'deseas' denotes the daily series removing the annual cycle.

	orig				deseas			
	$R^2_{\mathrm{LCC,ucir}}$	$R^2_{\mathrm{EIS,cir}}$	$R^2_{\mathrm{LCC,EIS}}$	$R^2_{\mathrm{LCC,EIS+ucir}}$	$R^2_{\mathrm{LCC,ucir}}$	$R^2_{\mathrm{EIS,cir}}$	$R^2_{\mathrm{LCC,EIS}}$	$R^2_{\mathrm{LCC,EIS+ucir}}$
NP	36	70	30	43	17	60	16	24
NA	30	79	26	39	27	76	23	36
SI	20	71	18	28	18	60	27	28
SP	50	79	50	60	11	58	23	29
SA	46	79	44	53	15	49	19	28
Mean	36	76	34	45	18	61	22	29

C

SUPPLEMENTAL INFORMATION FOR TOPOGRAPHIC EFFECTS

Figure C.1 shows that for the three-year simulation, removing the 15-day running mean is sufficient for decomposing the synoptic signal. No further deseasonalization is needed.

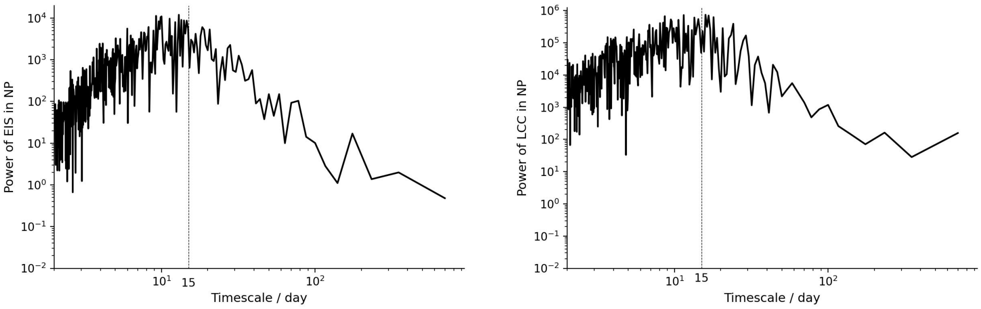

(a) EIS series

(b) LCC series

Figure C.1: Fast Fourier transformed timeseries after removing 15-day running mean. This series is used in the composite analysis for ICON simulations.

Figure C.2 shows that the mean state reflects the imprint of phase-locked amplification of synoptic-scale Rossby ridges.

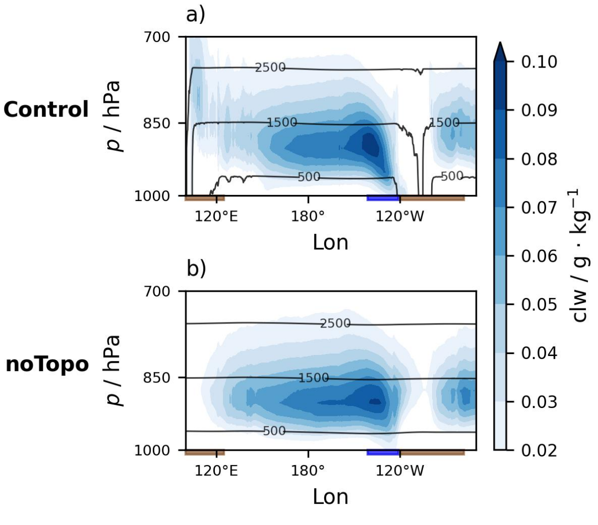

Figure C.2: Zonal cross sections (21°–50°N) of the three-year mean cloud liquid water (clw) in NP. Contours lines denote the three-year mean geopotential height in meters. The thick blue and brown underlines of the cross-sections represent Sc areas and continents, respectively.

Anderson, D.L. and A.E. Gill (1975). "Spin-up of a stratified ocean, with applications to upwelling." In: *Deep Sea Research and Oceanographic Abstracts* 22(9), pp. 583–596. doi: 10.1016/0011-7471(75)90046-7.

Bao, J. and B. Stevens (2021). "The elements of the thermodynamic structure of the tropical atmosphere." In: *Journal of the Meteorological Society of Japan* Ser. II, 99(6), pp. 1483–1499. doi: 10.2151/jmsj.2021-072.

Bellomo, K., A. Clement, T. Mauritsen, G. Rädel, and B. Stevens (2014). "Simulating the role of subtropical stratocumulus clouds in driving Pacific climate variability." In: *Journal of Climate* 27(13), pp. 5119–5131. doi: 10.1175/JCLI-D-13-00548.1.

Betts, A.K. (1986). "A new convective adjustment scheme. Part I: Observational and theoretical basis." In: *Quarterly Journal of the Royal Meteorological Society* 112(473), pp. 677–691. doi: 10.1002/qj.49711247307.

Blake, D. (1928). "Temperature inversions at San Diego, as deduced from aerographical observations by airplane." In: *Monthly Weather Review* 56(6), pp. 221–224. doi: 10.1175/1520-0493(1928)56<221:TIASDA>2.0.CO;2.

Blossey, P.N., C.S. Bretherton, M. Zhang, A. Cheng, S. Endo, T. Heus, Y. Liu, A.P. Lock, S.R. de Roode, and K.M. Xu (2013). "Marine low cloud sensitivity to an idealized climate change: The CGILS LES intercomparison." In: *Journal of Advances in Modeling Earth Systems* 5(2), pp. 234–258. doi: 10.1002/jame.20025.

Bony, S. and J.L. Dufresne (2005). "Marine boundary layer clouds at the heart of tropical cloud feedback uncertainties in climate models." In: *Geophysical Research Letters* 32(20), p. L20806. doi: 10.1029/2005GL023851.

Brayshaw, D.J., B. Hoskins, and M. Blackburn (2009). "The basic ingredients of the North Atlantic storm track. Part I: Land–sea contrast and orography." In: *Journal of the Atmospheric Sciences* 66(9), pp. 2539–2558. doi: 10.1175/2009JAS3078.1.

Bretherton, C.S. and P.N. Blossey (2014). "Low cloud reduction in a greenhouse-warmed climate: Results from Lagrangian LES of a subtropical marine cloudiness transition." In: *Journal of Advances in Modeling Earth Systems* 6(1), pp. 91–114. doi: 10.1002/2013MS000250.

Bretherton, C.S., P.N. Blossey, and C.R. Jones (2013). "Mechanisms of marine low cloud sensitivity to idealized climate perturbations: A single-LES exploration extending the CGILS cases." In: *Journal of Advances in Modeling Earth Systems* 5(2), pp. 316–337. doi: 10.1002/jame.20019.

Bretherton, C.S. and D.L. Hartmann (2009). "Large-scale controls on cloudiness." In: *Clouds in the Perturbed Climate System: Their Relationship to Energy Balance, Atmospheric Dynamics, and Precipitation*. Ed. by J. Heintzenberg and R. J. Charlson. MIT Press. doi: 10.7551/mitpress/8300.003.0012.

Bretherton, C.S. and M.C. Wyant (1997). "Moisture transport, lower-tropospheric stability, and decoupling of cloud-topped boundary layers." In: *Journal of the atmospheric sciences* 54(1), pp. 148–167. doi: 10.1175/1520-0469(1997)054<0148:MTLTSA>2.0.CO;2.

Caldwell, P. and C.S. Bretherton (2009). "Response of a subtropical stratocumulus-capped mixed layer to climate and aerosol changes." In: *Journal of climate* 22(1), pp. 20–38. doi: 10.1175/2008JCLI1967.1.

Charney, J. G. and A. Eliassen (1949). "A numerical method for predicting the perturbations of the middle latitude westerlies." In: *Tellus* 1(2), pp. 38–54. DOI: `10.3402/tellusa.v1i2.8500`.

Chen, H., H. Xu, J. Ma, and J. Deng (2022). "Why is the mid-tropospheric North Atlantic subtropical high much stronger than the North Pacific subtropical high in boreal summer?" In: *Climate Dynamics* 59(5), pp. 1883–1895. DOI: `10.1007/s00382-021-06074-3`.

Chen, P., M.P. Hoerling, and R.M. Dole (2001). "The origin of the subtropical anticyclones." In: *Journal of Atmospheric Sciences* 58(13), pp. 1827–1835. DOI: `10.1175/1520-0469(2001)058<1827:TOOTSA>2.0.CO;2`.

Chen, P., K.M. Holube, F. Lunkeit, N. Žagar, Y. B. Zhao, and R. Lu (2025). "Equatorial wave circulation associated with subseasonal convective variability over the subtropical western North Pacific in boreal summer." In: *Weather and Climate Dynamics* 6(4), pp. 1629–1642. DOI: `10.5194/wcd-6-1629-2025`.

Chen, T., W.B. Rossow, and Y. Zhang (2000). "Radiative effects of cloud-type variations." In: *Journal of climate* 13(1), pp. 264–286. DOI: `10.1175/1520-0442(2000)013<0264:REOCTV>2.0.CO;2`.

Cherchi, A., H. Annamalai, S. Masina, and A. Navarra (2014). "South Asian summer monsoon and the eastern Mediterranean climate: The monsoon–desert mechanism in CMIP5 simulations." In: *Journal of Climate* 27(18), pp. 6877–6903. DOI: `10.1175/JCLI-D-13-00530.1`.

Ciesielski, P.E., W.H. Schubert, and R.H. Johnson (2001). "Diurnal variability of the marine boundary layer during ASTEX." In: *Journal of the Atmospheric Sciences* 58(16), pp. 2355–2376. DOI: `10.1175/1520-0469(2001)058<2355:DVOTMB>2.0.CO;2`.

Clemesha, R.E., A. Gershunov, S.F. Iacobellis, and D.R. Cayan (2017). "Daily variability of California coastal low cloudiness: A balancing act between stability and subsidence." In: *Geophysical Research Letters* 44(7), pp. 3330–3338. DOI: `10.1002/2017GL073075`.

Cutler, L., M.A. Brunke, and X. Zeng (2022). "Re-evaluation of low cloud amount relationships with lower-tropospheric stability and estimated inversion strength." In: *Geophysical Research Letters* 136(11), e2022GL098137. DOI: `10.1029/2022GL098137`.

Ding, H., B. Stevens, and H Schmidt (2025). "Factors causing stratocumulus to deviate from subtropical high variability on seasonal to interannual timescales." In: *Atmospheric Chemistry and Physics* 25(18), pp. 10511–10521. DOI: `10.5194/acp-25-10511-2025`.

Dong, B., J.M. Gregory, and R.T. Sutton (2001). "Understanding land–sea warming contrast in response to increasing greenhouse gases. Part I: Transient adjustment." In: *Journal of Climate* 22(11), pp. 3079–3097. DOI: `10.1175/2009JCLI2652.1`.

Dussen, J.J. van der, S.R. de Roode, and A.P. Siebesma (2016). "How large-scale subsidence affects stratocumulus transitions." In: *Atmospheric Chemistry and Physics* 16, pp. 691–701. DOI: `10.5194/acp-16-691-2016`.

Duynkerke, P.G. and J. Teixeira (2001). "Comparison of the ECMWF reanalysis with FIRE I observations: Diurnal variation of marine stratocumulus." In: *Journal of climate* 14(7), pp. 1466–1478. DOI: `10.1175/1520-0442(2001)014<1466:COTERW>2.0.CO;2`.

Fons, E., A.K. Naumann, D. Neubauer, T. Lang, and U. Lohmann (2024). "Investigating the sign of stratocumulus adjustments to aerosols in the ICON global storm-resolving model." In: *Atmospheric Chemistry and Physics* 24(15), pp. 8653–8675. DOI: `10.5194/acp-24-8653-2024`.

Gaetani, M., B. Pohl, H. Douville, and B. Fontaine (2011). "West African Monsoon influence on the summer Euro-Atlantic circulation." In: *Geophysical Research Letters* 38(9), p. L09705. DOI: `10.1029/2011GL047150`.

Garfinkel, C.I., I.P. White, E.P. Gerber, O. Adam, and M. Jucker (2021). "Nonlinear interaction between the drivers of the monsoon and summertime stationary waves." In: *Geophysical Research Letters* 48(14), e2020GL092321. DOI: `10.1029/2020GL092321`.

Garreaud, R. and R. Muñoz (2004). "The diurnal cycle in circulation and cloudiness over the subtropical southeast Pacific: A modeling study." In: *Journal of climate* 17(8), pp. 1699–1710. DOI: `10.1175/1520-0442(2004)017<1699:TDCICA>2.0.CO;2`.

Garreaud, R.D., J. Rutllant, J. Quintana, J. Carrasco, and P. Minnis (2001). "CIMAR-5: A snapshot of the lower troposphere over the subtropical southeast Pacific." In: *Bulletin of the American Meteorological Society* 82(10), pp. 2193–2208. DOI: `10.1175/1520-0477-82.10.2193`.

Gates, W.L. (1992). "AN AMS continuing series: Global CHANGE–AMIP: The atmospheric model intercomparison project." In: *Bulletin of the American Meteorological Society* 73(12), pp. 1962–1970. DOI: `10.1175/1520-0477(1992)073<1962:ATAMIP>2.0.CO;2`.

Gates, W.L. et al. (1999). "An overview of the results of the Atmospheric Model Intercomparison Project (AMIP I)." In: *Bulletin of the American Meteorological Society* 80(1), pp. 29–56. DOI: `10.1175/1520-0477(1999)080<0029:AOOTRO>2.0.CO;2`.

George, R.C. and R. Wood (2010). "Subseasonal variability of low cloud radiative properties over the southeast Pacific Ocean." In: *Atmospheric Chemistry and Physics* 10(8), pp. 4047–4063. DOI: `10.5194/acp-10-4047-2010`.

Hadley, G. (1735). "VI. Concerning the cause of the general trade-winds." In: *Philosophical Transactions of the Royal Society of London* 39(437), pp. 58–62.

Hahn, C.J. and S.G. Warren (2007). *A gridded climatology of clouds over land (1971–1996) and ocean (1954–1997) from surface observations worldwide*. accessed on 2022-09-01. URL: `https://data.ess-dive.lbl.gov/datasets/doi:10.3334/CDIAC/CLI.NDP026E`.

Hartmann, D.L., Ockert-Bell, M.E., and M.L. Michelsen (1992). "The effect of cloud type on Earth's energy balance: Global analysis." In: *Journal of Climate* 5, pp. 1281–1304. DOI: `10.1175/1520-0442(1992)005<1281:TEOCTO>2.0.CO;2`.

Hartmann, D.L. and D.A. Short (1980). "On the use of earth radiation budget statistics for studies of clouds and climate." In: *Journal of Atmospheric Sciences* 37(6), pp. 1233–1250. DOI: `10.1175/1520-0469(1980)037<1233:OTUOER>2.0.CO;2`.

Held, I.M. and A.Y. Hou (1980). "Nonlinear axially symmetric circulations in a nearly inviscid atmosphere." In: *Journal of the Atmospheric Sciences* 37(3), pp. 515–533. DOI: `10.1175/1520-0469(1980)037<0515:NASCIA>2.0.CO;2`.

Hersbach, H. et al. (2017b). *Complete ERA5 from 1940: Fifth generation of ECMWF atmospheric reanalyses of the global climate [dataset]*. Copernicus Climate Change Service (C3S) Data Store (CDS), Data distribution by the German Climate Computing Center (DKRZ). `10.24381/cds.143582cf` (accessed on 2023-06-15).

– (2017a). *Complete ERA5 from 1940: Fifth generation of ECMWF atmospheric reanalyses of the global climate*. accessed on 2023-06-15. DOI: `10.24381/cds.143582cf`.

Hohenegger, C. et al. (2023). "ICON-Sapphire: simulating the components of the Earth system and their interactions at kilometer and subkilometer scales." In: *Geoscientific Model Development* 16(2), pp. 779–811. DOI: `10.5194/gmd-16-779-2023`.

Hoskins, B.J. and T. Ambrizzi (1993). "Rossby wave propagation on a realistic longitudinally varying flow." In: *Journal of Atmospheric Sciences* 50(12), pp. 1661–1671. DOI: `10.1175/1520-0469(1993)050<1661:RWPOAR>2.0.CO;2`.

Hoskins, B.J. and D.J. Karoly (1981). "The steady linear response of a spherical atmosphere to thermal and orographic forcing." In: *Journal of Atmospheric Sciences* 38(6), pp. 1179–1196. DOI: `10.1175/1520-0469(1981)038<1179:TSLROA>2.0.CO;2`.

Hotz, B., L. Papritz, and M. Röthlisberger (2024). "Understanding the vertical temperature structure of recent record-shattering heatwaves." In: *Weather and Climate Dynamics* 5(1), pp. 323–343. DOI: `10.5194/wcd-5-323-2024`.

Jiménez-Esteve, B., K. Kornhuber, and D. I. V. Domeisen (2022). "Heat extremes driven by amplification of phase-locked circumglobal waves forced by topography in an idealized atmospheric model." In: *Geophysical Research Letters* 49(21), e2021GL096337. DOI: `10.1029/2021GL096337`.

Karlsson, K.-G. et al. (2022). *CLARA-A3: The third edition of the AVHRR-based CM SAF climate data record on clouds, radiation and surface albedo covering the period 1979 to 2023 [dataset]*. Copernicus Climate Change Service (C3S) Climate Data Store (CDS). `10.24381/cds.68653055` (accessed on 2025-07-01).

Kasahara, A. (1976). "Normal modes of ultralong waves in the atmosphere." In: *Mon. Wea. Rev.* 104, pp. 669–690.

Kawai, H., T. Koshiro, and M. Webb (2017). "Interpretation of Factors Controlling Low Cloud Cover and Low Cloud Feedback Using a Unified Predictive Index." In: *Journal of Climate* 30, pp. 9119–9131. DOI: `10.1175/JCLI-D-16-0825.1`.

Klein, S. A. (1997). "Synoptic variability of low-cloud properties and meteorological parameters in the subtropical trade wind boundary layer." In: *Journal of Climate* 10(8), pp. 2018–2039. DOI: `10.1175/1520-0442(1997)010<2018:SVOLCP>2.0.CO;2`.

Klein, S. A. and D. L. Hartmann (1993). "The Seasonal Cycle of Low Stratiform Clouds." In: *Journal of Climate* 6(8), pp. 1587–1606. DOI: `10.1175/1520-0442(1993)006<1587:TSCOLS>2.0.CO;2`.

Klein, S. A., D. L. Hartmann, and J. R. Norris (1995). "On the relationships among low-cloud structure, sea surface temperature, and atmospheric circulation in the summertime northeast Pacific." In: *Journal of Climate* 8(5), pp. 1140–1155. DOI: `10.1175/1520-0442(1995)008<1140:OTRALC>2.0.CO;2`.

Koshiro, T. and M. Shiotani (2014). "Relationship between low stratiform cloud amount and estimated inversion strength in the lower troposphere over the global ocean in terms of cloud types." In: *Journal of the Meteorological Society of Japan* Ser. II 92(1), pp. 107–120. DOI: `10.2151/jmsj.2014-107`.

Large, W. G. and S. Pond (1981). "Open ocean momentum flux measurements in moderate to strong winds." In: *Journal of physical oceanography* 11(3), pp. 324–336. DOI: `10.1175/1520-0485(1981)011<0324:OOMFMI>2.0.CO;2`.

Lawrence, Mark G. (2005). "The relationship between relative humidity and the dewpoint temperature in moist air: A simple conversion and applications." In: *Bulletin of the American Meteorological Society* 86(2), pp. 225–234. DOI: `10.1175/BAMS-86-2-225`.

Lee, S. and H.K. Kim (2003). "The dynamical relationship between subtropical and eddy-driven jets." In: *Journal of the atmospheric sciences* 60(12), pp. 1490–1503. DOI: `10.1175/1520-0469(2003)060<1490:TDRBSA>2.0.CO;2`.

Lewis, H. and G. Bellon (2025). "Systematic upstream large-scale control of subtropical low-cloud properties." In: *Journal of Climate* 38(1), pp. 327–346. DOI: `10.1175/JCLI-D-24-0181.1`.

Lewis, H., G. Bellon, and T. Dinh (2023). "Upstream large-scale control of subtropical low-cloud climatology." In: *Journal of Climate* 36(10), pp. 3289–3303. DOI: `10.1175/JCLI-D-22-0676.1`.

Lilly, D.K. (1968). "Models of cloud-topped mixed layers under a strong inversion." In: *Quarterly Journal of the Royal Meteorological Society* 94(401), pp. 292–309. DOI: `10.1002/qj.49709440106`.

Lindzen, R.S. and A.Y. Hou (1988). "Hadley circulations for zonally averaged heating centered off the equator." In: *Journal of atmospheric science* 45(17), 2416–2427. DOI: `10.1175/1520-0469(1988)045<2416:HCFZAH>2.0.CO;2`.

Liu, X., K.M. Grise, D.F. Schmidt, and R.E. Davis (2021). "Regional characteristics of variability in the Northern Hemisphere wintertime polar front jet and subtropical jet in observations and CMIP6 models." In: *Journal of Geophysical Research: Atmospheres* 126(22), e2021JD034876. DOI: `10.1029/2021JD034876`.

Manabe, S., J. Smagorinsky, and R.F. Strickler (1965). "Simulated climatology of a general circulation model with a hydrologic cycle." In: *Monthly Weather Review* 93(12), pp. 769–798. DOI: `10.1175/1520-0493(1965)093<0769:SCOAGC>2.3.CO;2`.

McCoy, D.T., R. Eastman, D.L. Hartmann, and R. Wood (2017). "The change in low cloud cover in a warmed climate inferred from AIRS, MODIS, and ERA-Interim." In: *Journal of climate* 30(10), pp. 3609–3620. DOI: `10.1175/JCLI-D-15-0734.1`.

Myers, T.A. and J.R. Norris (2013). "Observational evidence that enhanced subsidence reduces subtropical marine boundary layer cloudiness." In: *Journal of climate* 26(19), pp. 7507–7524. DOI: `10.1175/JCLI-D-12-00736.1`.

Neduhal, V., N. Žagar, F. Lunkeit, I. Polichtchouk, and Ž. Zaplotnik (2024). "Decomposition of the horizontal wind divergence associated with the Rossby, mixed Rossby-gravity, inertia-gravity, and kelvin waves on the sphere." In: *Journal of Geophysical Research: Atmospheres* 129(9), e2023JD040427. DOI: `10.1029/2023JD040427`.

Nigam, S. and S.C. Chan (2009). "On the summertime strengthening of the Northern Hemisphere Pacific sea level pressure anticyclone." In: *Journal of climate* 22(5), pp. 1174–1192. DOI: `10.1175/2008JCLI2322.1`.

Norris, J.R. and S.A. Klein (2000). "Low cloud type over the ocean from surface observations. Part III: Relationship to vertical motion and the regional surface synoptic environment." In: *Journal of climate* 13(1), pp. 245–256. DOI: `10.1175/1520-0442(2000)013<0245:LCTOTO>2.0.CO;2`.

Park, S. and J. Shin (2019). "Heuristic estimation of low-level cloud fraction over the globe based on a decoupling parameterization." In: *Atmospheric Chemistry and Physics* 19(8), pp. 5635–5660. DOI: `10.5194/acp-19-5635-2019`.

Polster, C. and V. Wirth (2023). "A new atmospheric background state to diagnose local waveguidability." In: *Geophysical Research Letters* 50(24), e2023GL106166. DOI: `10.1029/2023GL106166`.

Poulsen, C.A., G. McGarragh, G. Thomas, M. Christensen, A. Povey, D. Grainger, S. Proud, and R. Hollmann (2017). *ESA Cloud Climate Change Initiative (Cloud_cci): ATSR2-AASTR monthly gridded cloud properties, version 2.0*. accessed on 2023-02-16. URL: `https://catalogue.ceda.ac.uk/uuid/1ea3b2e391e4441daa57100a02b98691`.

Qu, X., A. Hall, S.A. Klein, and P.M. Caldwell (2014). "On the spread of changes in marine low cloud cover in climate model simulations of the 21st century." In: *Climate dynamics* 42(9), pp. 2603–2626. DOI: `10.1007/s00382-013-1945-z`.

Qu, X., A. Hall, S.A. Klein, and A.M. DeAngelis (2015). "Positive tropical marine low-cloud cover feedback inferred from cloud-controlling factors." In: *Geophysical Research Letters* 42(18), pp. 7767–7775. DOI: `10.1002/2015GL065627`.

Randall, D.A. (1980). "Conditional instability of the first kind upside-down." In: *Journal of Atmospheric Sciences* 37(1), pp. 125–130. DOI: `10.1175/1520-0469(1980)037<0125:CIOTFK>2.0.CO;2`.

Randall, D.A., J.A. Coakley, C.W. Fairall, R.A. Kropfli, and D.H. Lenschow (1984). "Outlook for research on subtropical marine stratiform clouds." In: *Bulletin of the American Meteorological Society* 65(12), pp. 1290–1301. DOI: `10.1175/1520-0477(1984)065<1290:OFROSM>2.0.CO;2`.

Randall, D.A. and M.J. Suarez (1984). "On the dynamics of stratocumulus formation and dissipation." In: *Journal of Atmospheric Sciences* 41(20), pp. 3052–3057. DOI: `10.1175/1520-0469(1984)041<3052:OTDOSF>2.0.CO;2`.

Richter, I. and C.R. Mechoso (2004). “Orographic influences on the annual cycle of Namibian stratocumulus clouds.” In: *Geophysical Research Letters* 31(24), p. L24108. DOI: `10.1029/2004GL020814`.

– (2006). “Orographic influences on subtropical stratocumulus.” In: *Journal of the Atmospheric Sciences* 63(10), pp. 2585–2601. DOI: `10.1175/JAS3756.1`.

Riehl, H. (1961). *Jet streams of the atmosphere*. US Government Printing Office.

Ringler, T.D. and K.H. Cook (1997). “Factors controlling nonlinearity in mechanically forced stationary waves over orography.” In: *Journal of the Atmospheric Sciences* 54(22), pp. 2612–2629. DOI: `10.1175/1520-0469(1997)054<2612:FCNIMF>2.0.CO;2`.

Rodwell, M. J. and B. J. Hoskins (1996). “Monsoons and the dynamics of deserts.” In: *Quarterly Journal of the Royal Meteorological Society* 122(534), pp. 1385–1404. DOI: `10.1002/qj.49712253408`.

Rodwell, M.J. and B.J. Hoskins (2001). “Subtropical anticyclones and summer monsoons.” In: *Journal of Climate* 14(15), pp. 3192–3211. DOI: `10.1175/1520-0442(2001)014<3192:SAASM>2.0.CO;2`.

Sardeshmukh, P.D. and B.J. Hoskins (1988). “The generation of global rotational flow by steady idealized tropical divergence.” In: *Journal of Atmospheric Sciences* 45(7), pp. 1228–1251. DOI: `10.1175/1520-0469(1988)045<1228:TGOGRF>2.0.CO;2`.

Schubert, W.H. (1976). “Experiments with Lilly’s cloud-topped mixed layer model.” In: *Journal of the Atmospheric Sciences* 33(3), pp. 436–446. DOI: `10.1175/1520-0469(1976)033<0436:EWLCTM>2.0.CO;2`.

Schubert, W.H., P.E. Ciesielski, C. Lu, and R.H. Johnson (1995). “Dynamical adjustment of the trade wind inversion layer.” In: *Journal of Atmospheric Sciences* 52(16), pp. 2941–2952. DOI: `10.1175/1520-0469(1995)052<2941:DAOTTW>2.0.CO;2`.

Scott, R.C., T.A. Myers, J.R. Norris, M.D. Zelinka, S.A. Klein, M. Sun, and D.R. Doelling (2020). “Observed sensitivity of low-cloud radiative effects to meteorological perturbations over the global oceans.” In: *Journal of Climate* 33(18), pp. 7717–7734. DOI: `10.1175/JCLI-D-19-1028.1`.

Segura, H. et al. (2025). “nextGEMS: entering the era of kilometer-scale Earth system modeling.” In: *Geoscientific Model Development* 18(20), pp. 7735–7761. DOI: `10.5194/gmd-18-7735-2025`.

Siebesma, A.P. et al. (2004). “Cloud representation in general-circulation models over the northern Pacific Ocean: A EUROCS intercomparison study.” In: *Quarterly Journal of the Royal Meteorological Society* 130(604), pp. 3245–3267. DOI: `10.1256/qj.03.146`.

Singh, M.S. and P.A. O’Gorman (2013). “Influence of entrainment on the thermal stratification in simulations of radiative-convective equilibrium.” In: *Geophysical Research Letters* 40(16)), pp. 4398–4403. DOI: `10.1002/grl.50796`.

Slingo, A. (1990). “Sensitivity of the Earth’s radiation budget to changes in low clouds.” In: *Nature* 343(6253), pp. 49–51. DOI: `10.1038/343049a0`.

Sobel, A.H. and C.S. Bretherton (2000). “Modeling tropical precipitation in a single column.” In: *Journal of climate* 13(24), pp. 4378–4392. DOI: `10.1175/1520-0442(2000)013<4378:MTPIAS>2.0.CO;2`.

Sobel, A.H., J. Nilsson, and L.M. Polvani (2001). “The weak temperature gradient approximation and balanced tropical moisture waves.” In: *Journal of the Atmospheric Sciences* 58(23), pp. 3650–3665. DOI: `10.1175/1520-0469(2001)058<3650:TWTGAA>2.0.CO;2`.

Soden, B.J. and G.A. Vecchi (2011). “The vertical distribution of cloud feedback in coupled ocean-atmosphere models.” In: *Geophysical Research Letters* 38(12), p. L12704. DOI: `10.1029/2011GL047632`.

Stephens, G.L. (2005). “Cloud feedbacks in the climate system: A critical review.” In: *Journal of Climate* 18(2), pp. 237–273. DOI: `10.1175/JCLI-3243.1`.

Stevens, B. (2005). "Atmospheric moist convection." In: *Annu. Rev. Earth Planet. Sci.* 33(1), pp. 605–643. DOI: `10.1146/annurev.earth.33.092203.122658`.

Stevens, B., A.S. Ackerman, B.A. Albrecht, A.R. Brown, A. Chlond, J. ... Cuxart, and D.E. Stevens (2001). "Simulations of trade wind cumuli under a strong inversion." In: *Journal of the Atmospheric Sciences* 58(14), pp. 1870–1891. DOI: `10.1175/1520-0469(2001)058<1870:SOTWCU>2.0.CO;2`.

Stevens, B. and J. Brenguier (2009). "Cloud controlling factors: Low clouds." In: *Clouds in the Perturbed Climate System: Their Relationship to Energy Balance, Atmospheric Dynamics, and Precipitation*. Ed. by J. Heintzenberg and R. J. Charlson. MIT Press, pp. 173–196. DOI: `10.7551/mitpress/8300.003.0010`. URL: `10.7551/mitpress/8300.003.0010`.

Stone, P.H. and J.H. Carlson (1979). "Atmospheric lapse rate regimes and their parameterization." In: *Journal of the Atmospheric Sciences* 36(3), pp. 415–423. DOI: `10.1175/1520-0469(1979)036<0415:ALRRAT>2.0.CO;2`.

Takaya, K. and H. Nakamura (2001). "A Formulation of a Phase-Independent Wave-Activity Flux for Stationary and Migratory Quasigeostrophic Eddies on a Zonally Varying Basic Flow." In: *Journal of the Atmospheric Sciences* 58, pp. 608–627. DOI: `10.1175/1520-0469(2001)058<0608:AFOAPI>2.0.CO;2`.

Toniazzo, T., S.J. Abel, R. Wood, C.R. Mechoso, G. Allen, and L.C. Shaffrey (2011). "Large-scale and synoptic meteorology in the south-east Pacific during the observations campaign VOCALS-REx in austral Spring 2008." In: *Atmospheric Chemistry and Physics* 11, pp. 4977–5009. DOI: `10.5194/acp-11-4977-2011`.

Wang, Z., J. Yuan, R. Wood, Y. Chen, and T. Tong (2023). "Profile-based estimated inversion strength." In: *Atmospheric Chemistry and Physics* 23(5), pp. 3247–3266. DOI: `10.5194/acp-23-3247-2023`.

Warren, S.G., C.J. Hahn, J. London, R.M. Chervin, and R.L. Jenne (1986). "Global Distribution of Total Cloud Cover and Cloud Type Amounts Over Land (No. NCAR/TN-273+STR)." In: *University Corporation for Atmospheric Research* 29, + 200 maps. DOI: `10.5065/D6GH9FXB`.

– (1988). "Global Distribution of Total Cloud Cover and Cloud Type Amounts Over the Ocean (No. NCAR/TN-317+STR)." In: *University Corporation for Atmospheric Research* 42, + 170 maps. DOI: `10.5065/D6QC01D1`.

Weaver, C.J. and R. Pearson Jr (1990). "Entrainment instability and vertical motion as causes of stratocumulus breakup." In: *Quarterly Journal of the Royal Meteorological Society* 116(496), pp. 1359–1388. DOI: `10.1002/qj.49711649606`.

Webb, M.J. and A.P. Lock (2013). "Coupling between subtropical cloud feedback and the local hydrological cycle in a climate model." In: *Climate dynamics* 41(7), pp. 1923–1939. DOI: `10.1007/s00382-012-1608-5`.

Wirth, V. (2020). "Waveguidability of idealized midlatitude jets and the limitations of ray tracing theory." In: *Weather and Climate Dynamics* 1(1), pp. 111–125. DOI: `10.5194/wcd-1-111-2020`.

Wood, R. (2012). "Stratocumulus clouds." In: *Monthly weather review* 140(8), pp. 2373–2423. DOI: `10.1175/MWR-D-11-00121.1`.

Wood, R. and C.S. Bretherton (2004). "Boundary layer depth, entrainment, and decoupling in the cloud-capped subtropical and tropical marine boundary layer." In: *Journal of Climate* 17(18), pp. 3576–3588. DOI: `10.1175/1520-0442(2004)017<3576:BLDEAD>2.0.CO;2`.

– (2006). "On the relationship between stratiform low cloud cover and lower-tropospheric stability." In: *Journal of Climate* 19(24), pp. 6425–6432. DOI: `10.1175/JCLI3988.1`.

Žagar, N., V. Neduhal, S. Vasylkevych, Ž. Zaplotnik, and H.L. Tanaka (2023). "Decomposition of vertical velocity and its zonal wavenumber kinetic energy spectra in the hydrostatic atmosphere." In: *J. Atmos. Sci.* 80, pp. 2747–2767. DOI: `10.1175/JAS-D-23-0090.1`.

Zhang, Y., J. Li, Z. Hou, B. Zuo, Y. Xu, X. Tang, and H. Wang (2022). "Climatic effects of the Indian Ocean tripole on the Western United States in boreal summer." In: *Journal of Climate* 35(8), pp. 2503–2523. DOI: `10.1175/JCLI-D-21-0490.1`.

Zhou, C., M.D. Zelinka, A.E. Dessler, and S.A. Klein (2015). "The relationship between interannual and long-term cloud feedbacks." In: *Geophysical Research Letters* 42(23), pp. 10463–10469. DOI: `10.1002/2015GL066698`.

Zilli, M.T. and N.C. Hart (2021). "Rossby wave dynamics over South America explored with automatic tropical–extratropical cloud band identification framework." In: *Journal of Climate* 34(20), pp. 8125–8144. DOI: `10.1175/JCLI-D-21-0020.1`.

Žagar, N. and C. L. Franzke (2015). "Systematic decomposition of the Madden-Julian Oscillation into balanced and inertio-gravity components." In: *Geophysical Research Letters* 42(16), pp. 6829–6835. DOI: `10.1002/2015GL065130`.

Žagar, N., A. Kasahara, K. Terasaki, J. Tribbia, and H. Tanaka (2015). "Normal-mode function representation of global 3-D data sets: Open-access software for the atmospheric research community." In: *Geoscientific Model Development* 8(4), pp. 1169–1195. DOI: `10.5194/gmd-8-1169-2015`.

Eidesstattliche Versicherung

Declaration upon Oath

Hiermit erkläre ich an Eides statt, dass ich die vorliegende Dissertationsschrift selbst verfasst und keine anderen als die angegebenen Quellen und Hilfsmittel benutzt habe.

Sofern im Zuge der Erstellung der vorliegenden Dissertationsschrift generative Künstliche Intelligenz (gKI) basierte elektronische Hilfsmittel verwendet wurden, versichere ich, dass meine eigene Leistung im Vordergrund stand und dass eine vollständige Dokumentation aller verwendeten Hilfsmittel gemäß der Guten wissenschaftlichen Praxis vorliegt. Ich trage die Verantwortung für eventuell durch die gKI generierte fehlerhafte oder verzerrte Inhalte, fehlerhafte Referenzen, Verstöße gegen das Datenschutz- und Urheberrecht oder Plagiate.

I hereby declare and affirm that this doctoral dissertation is my own work and that I have not used any aids and sources other than those indicated.

If electronic resources based on generative artificial intelligence (gAI) were used in the course of writing this dissertation, I confirm that my own work was the main and value-adding contribution and that complete documentation of all resources used is available in accordance with good scientific practice. I am responsible for any erroneous or distorted content, incorrect references, violations of data protection and copyright law or plagiarism that may have been generated by the gAI.

Hamburg, 13.03.2026

Hairu Ding

Ich versichere, dass dieses gebundene Exemplar der Dissertation und das in elektronischer Form eingereichte Dissertationsexemplar (über den Docata-Upload) und das bei der Fakultät (zuständiges Studienbüro bzw. Promotionsbüro Physik) zur Archivierung eingereichte gedruckte gebundene Exemplar der Dissertationsschrift identisch sind.

I, the undersigned, declare that this bound copy of the dissertation and the dissertation submitted in electronic form (via the Docata upload) and the printed bound copy of the dissertation submitted to the faculty (responsible Academic Office or the Doctoral Office Physics) for archiving are identical.

Hamburg, 13.03.2026

Hairu Ding